An Algorithm for Automatic Crystal Identification in Pixelated Scintillation Detectors Using Thin Plate Splines and Gaussian Mixture Models

By

Graham Schellenberg

A Thesis Submitted to the Faculty of Graduate Studies of
The University of Manitoba

In partial fulfillment of the requirements of the degree of

MASTER OF SCIENCE

Department of Physics and Astronomy
University of Manitoba
Winnipeg, Manitoba, Canada

Abstract

Positron emission tomography (PET) is a non-invasive imaging technique which utilizes positron-emitting radiopharmaceuticals (PERs) to characterize biological processes in tissues of interest. A PET scanner is usually composed of multiple scintillation crystal detectors placed in a ring so as to capture coincident photons from a position annihilation. These detectors require a crystal lookup table (CLUT) to map the detector response to the crystal of interaction. These CLUTs must be accurate, lest events get mapped to the wrong crystal of interaction degrading the final image quality. This work describes an automated algorithm, for CLUT generation, focused around Gaussian Mixture Models (GMM) with Thin Plate Splines (TPS). The algorithm was tested with flood image data collected from 16 detectors. The method maintained at least 99.8% accuracy across all tests. This method is considerably faster than manual techniques and can be adapted to different detector configurations.

Acknowledgements

The work in this thesis would not have been possible without the support and guidance of the following individuals:

- Dr. Andrew L. Goertzen, my academic advisor, who provided invaluable insight and experience while also tolerating my many questions.
- Dr. Jonathan D. Thiessen, who helped me start out in the lab and provided me with the Inveon data.
- Greg Stortz, for his help with the paper and allowing me to spitball ideas off him (resulting in THIS thesis).
- Ehsan Shams, Bryan McIntosh, and all of my other colleagues and coworkers in the lab, I wish you all the best.
- My friends and family, who support me in ways they will never know.

Table of Contents

List of Figures

List of Equations

Equation

1. Introduction

1.1 Positron Emission Tomography

Positron Emission Tomography (PET) is a nuclear medicine imaging modality based on positioning the annihilation event of positrons within a patient or phantom. When a positron comes into contact with an electron they undergo an annihilation event resulting in two 511 keV gamma rays emitted at approximately 180^{o} to one another. Positrons are not naturally abundant within a patient or imaging subject, so they must be injected with a positron emitting radio-pharmaceutical (also called a tracer) prior to the scan. The tracer is a metabolically relevant molecule labelled so as to decay by positron emission. A common tracer in PET is ^{18}F-fluorodeoxyglucose (Schlyer, 2004), which is used to view glucose metabolism in mammalian cells, useful for locating tumors, neurological disorders, and certain myocardial diseases. With the appropriate choice of tracer, PET can be used to study a variety of *in vivo* biological processes.

For accurate images, PET systems rely on the detection of the two 511 keV annihilation photons within some coincidence window. Since the two photons are emitted approximately 180^{o} apart, the most common scanner design is a ring. This ring is subdivided into modules of individual detectors capable of stopping, and detecting, a significant fraction of the 511 keV photons passing through it. The detectors are almost exclusively scintillation detectors due to their favorable attributes and longstanding history as PET detectors. A typical scintillation detector is composed of a scintillation crystal coupled to a photodetector. The scintillation crystal varies from one monolithic block to a lattice of individual crystals depending on the design being implemented. The scintillation crystal, on a successful absorption of a 511 keV photon, will emit an isotropic pulse containing thousands of optical photons. These optical photons will travel through the crystal and some will be absorbed/detected by

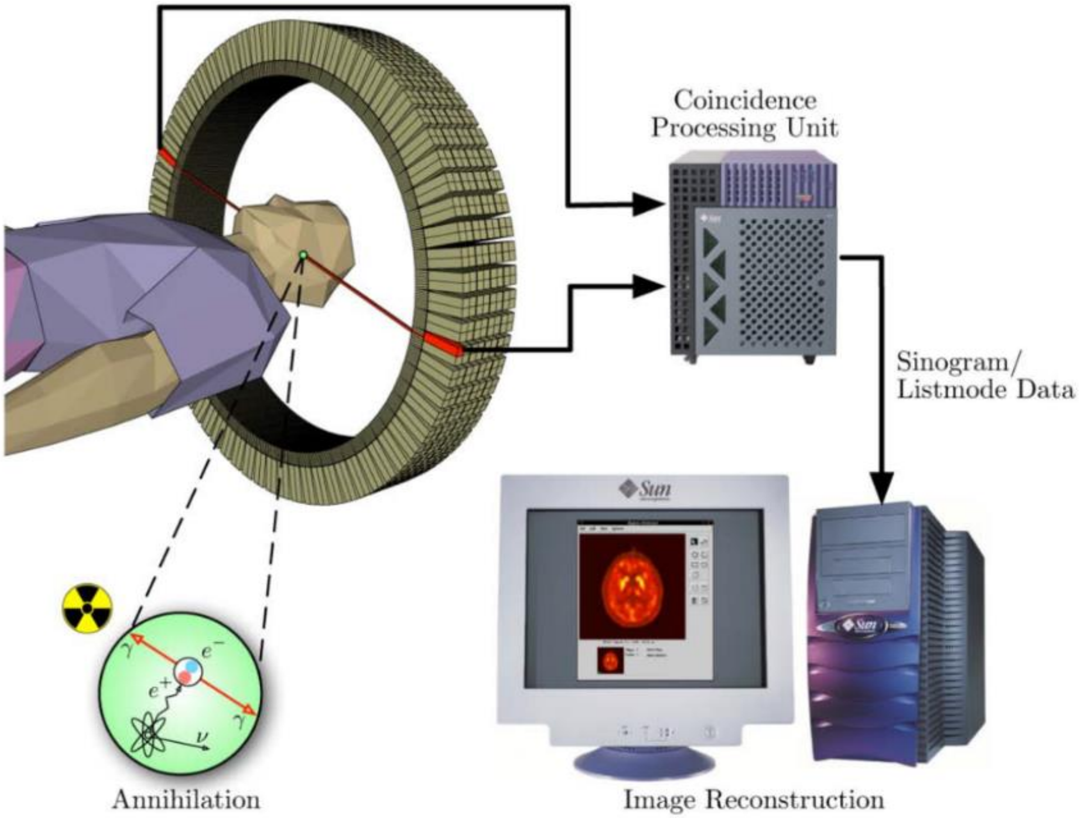

Figure 1-1. Overview of PET systems (Langner, 2003)

the photodetector which converts the optical photon pulse into an electric pulse signal. Conventionally, Photomultiplier Tubes (PMT) have been used as the photodetector for PET scanners, however in the past decade semiconductor based photodetectors have become an important and favorable choice for certain PET systems, specifically including hybrid PET/MRI systems, due, in part, to their smaller form factors and magnetic field insensitivity.

After the optical photon pulse is converted into an electrical signal, it is sent to a coincidence processing system that attempts to pair it with the electric pulse from another detector within a certain coincidence timing window. The width of the timing window can vary between 3ns to 20ns depending on the size of the scanner and scintillation crystal used. Also of importance is the measured energy of the detected photon. To ensure that the detected photon is within an acceptable percentage of 511 keV, an energy window is set (usually 6% to 25% of 511 keV) and any event outside of this window is discarded. This coincidence data is typically stored as list mode data (or sinograms) and sent to the image reconstruction system. Typical images will be reconstructed using upwards of millions of these coincidence pairs. A high level overview of a typical PET system is depicted in Figure 1-1. The bottom line of PET system performance is the ability to stop the 511 keV photon, and the accuracy to which it is able to locate the position of the 511 keV gamma within the detector block, these are the most important factors, affecting the quality of the system as a whole.

1.2 Multimodality PET

Over the past 15 years, clinical standalone PET systems have become rare, more common is a joint system that pairs PET and Computed Tomography (CT). CT involves acquiring multiple planar x-ray images at different angles to create an anatomical image of the subject. PET alone only provides information on the location of radio-pharmaceutical within the subject. To improve the significance of the PET data, it is helpful to combine it with the excellent anatomical information provided by CT. However, the two modalities are not without compatibility issues. PET-CT systems must acquire their images sequentially. Simultaneous acquisition by both modalities is not possible due to the large amount of x-rays emitted by the CT. The number of x-rays dwarfs the average radio-pharmaceutical activity to such a degree that it would saturate the PET detectors making detection of the 511 keV photons impossible even with the imposed energy window.

More recent is the development of PET combined with Magnetic Resonance Imaging (MRI). PET-MR has not been pursued to the same degree as PET-CT due to severe incompatibilities between the PMT based photodetectors and high magnetic fields used in MR. However, in the past decade advances in semiconductor based photodetectors have made PET-MR a successful and viable hybrid imaging technique.

1.3 PET-MR

MR provides several benefits over CT such as improved soft tissue contrast and higher spatial resolution in general. On top of this, MR does not use ionizing radiation to construct anatomical images meaning that unlike CT, MR delivers no radiation dose to the patient/subject. While MR holds advantages over CT, the hybrid modality PET-MR has multiple benefits over PET-CT. PET and MR couple together with synergistic advantages, where PET falls short MR excels, and vice versa. PET is unparalleled in quantitative detection of radiotracers, which target specific metabolic processes or molecules. The ability of MR to quantify certain molecules within a subject is orders of magnitude less accurate than PET. However, as stated before, PET gives little anatomical information and cannot distinguish the molecular species that the injected tracer is interacting with. MR can provide anatomical information and tissue contrast to supplement the PET information. In addition, using Magnetic Resonance Spectroscopy (MRS), it is possible to identify the molecular species the tracer is interacting with in specific regions of the subject. PET-MR systems are also capable of operating in conjunction with one another. Simultaneous acquisition of images is a major benefit as it gives perfect co-registration between the biological process and anatomy being observed. This advantage can be taken further using the MR to correct for subject motion (such as breathing) increasing the accuracy of the PET image and information (Tsoumpas, Agarwal, Marsden, & King, 2012). Lastly, PET systems suffer from a small loss in spatial resolution due to positron range. When the positron is released from the tracer it travels a short distance (up to several mm (Levin & Hoffman, 1999)) before annihilating with an electron. This walk leads to a reduction in system accuracy and spatial resolution, however since the positron carries a charge equal and opposite to an electron they are influenced by the strong magnetic field of the MR. This magnetic field causes a significant reduction in positron range, improving the overall PET system resolution (Wirrwar, Vosberg, Herzog, Hailing, & Weber, 1997).

Early PET systems exclusively utilized PMTs coupled directly to a single scintillation crystal (Hoffman, Phelps, Mullani, Higgins, & Ter-pogossian, 1976; Phelps, Hoffman, Huang, & Kuhl, 1978). PMTs operate by cascading electrons from anode to anode through a vacuum tube. When the PMT is exposed to a magnetic field, the electrons, having a charge and velocity, are deflected, changing their trajectory. This results in severe distortions in the PMT output signal, rendering them unsuitable for use in a magnetic field and subsequently MR incompatible. It was this incompatibility that hindered early work on a hybrid PET-MR system. Despite this complication, PET-MR systems were still constructed using PMTs. Early PET-MRs were constructed with the PMTs residing outside of the magnetic field of the MR. One design has the PET and MR systems completely separate but operating on the same patient/subject bed so as to acquire sequential images. The Ingenuity TF PET/MR from Philips Medical Systems is based on this design (Zaidi et al., 2011). The Ingenuity has the PET and MR 4.2m apart on the same bed with extra shielding around the PET system to protect the PMTs from the fringe fields still present at that distance from the MR. While this system requires little to no modifications of the PET and MR it does require sequential imaging which has the disadvantages explained previously as well as significantly longer scan times in a clinical setting.

Other systems were constructed using a light guide to funnel the optical light from the scintillation crystals to PMTs located outside the magnetic field. In this design the scintillation crystal array is positioned within the MR Field of View (FOV) in a typical PET detector ring. This design, while allowing simultaneous PET and MR acquisitions, suffered from significant light loss through the light guides which were initially constructed with bent glass rectangles. Development of fiber optic cables, to replace the glass light guides, helped reduce light loss but still suffered from space limitations. A modified MicroPET® from the University of Cambridge utilizes this design (Hawkes et al., 2008; Lucas et al., 2006)

Possibly the most successful PET-MRs utilize designs that rely on the use of solid state photodetectors, also known as Avalanche Photodiodes (APD). This class of photodetector remains stable under the influence of strong magnetic fields and usually has a small form factor making them very attractive for use within the bore of an MR.

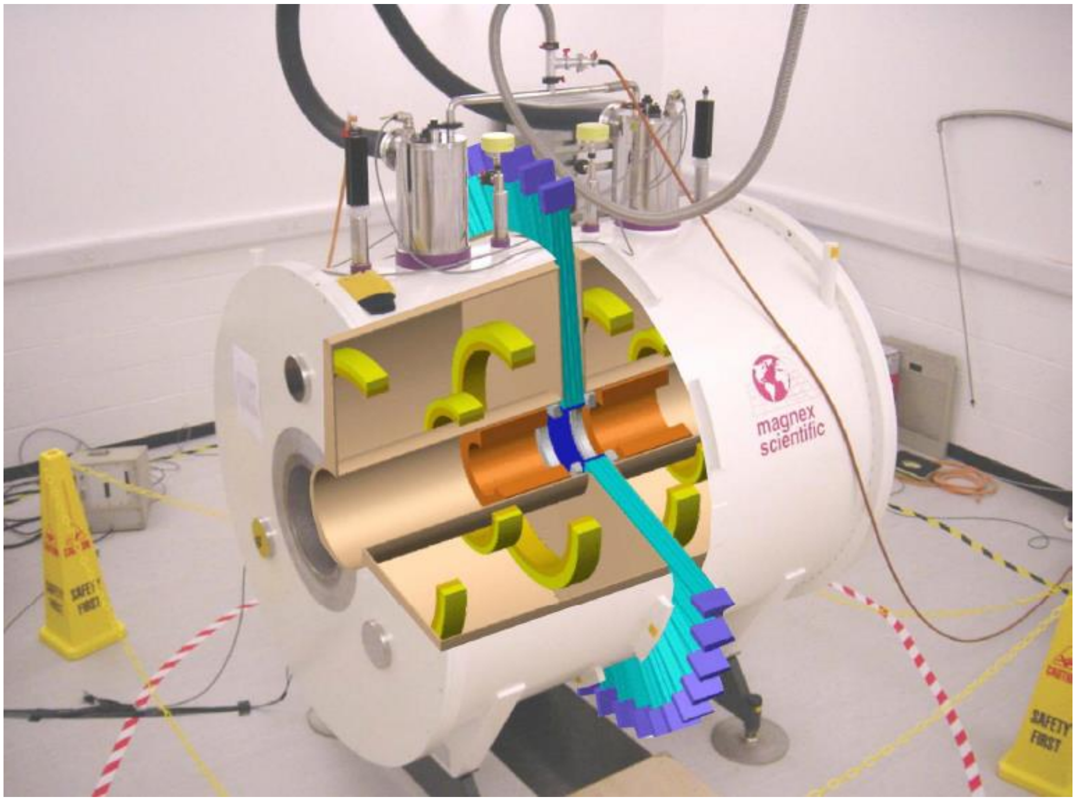

Figure 1-2. Partial transparent overview of the MicroPET®. System utilizes fiber optic cables, depicted in light blue, to funnel light from the scintillation crystals out to the PMTs, depicted in dark blue, located outside the system (Lucas et al., 2006).

1.4 Solid State Photodetectors

1.4.1 Avalanche Photodiodes

Major drawbacks of the PMT, such as large form factor and magnetic field sensitivity, have been overcome with the continued development of semiconductor electronics, specifically, the APD. The working structure of an APD is a negatively biased p-n junction. When an optical photon strikes the surface of the APD there is a probability that an electron-hole pair will be created. This electron, propelled by the negative bias, can create multiple electron-hole pairs through impact ionization, which, if continued, will create an avalanching cascade of electrons eventually reaching the anode and being read out as a detectable signal pulse. Aside from being insensitive to magnetic fields, APDs hold a number of benefits over conventional PMTs such as smaller form factors, less bias voltage, and a higher quantum efficiency in the blue range. Although it ranges between specific device, APDs are thought in general to have good energy resolution and average timing resolution. While the technology is still growing, current APDs have some drawbacks. A single avalanche event requires relatively little work to set off and as such APDs suffer from high noise from dark current. While requiring less bias voltage the gain of APD devices is quite low compared to PMTs. The gain of an APD is mainly determined by bias voltage it is also affected by temperature, thus if APDs are used within a system it is important to monitor the system temperature since the position of the photopeak, and energy window around it, depend on the gain.

One of the first scintillation detectors utilizing APDs was constructed at the University of Sherbrooke in 1984. It used a 9x9x38 mm^3 block of Thallium doped Sodium Iodide, NaI(Tl), for a scintillation crystal and using Cs-137, emitting a gamma ray of energy 662 keV, it obtained an energy resolution of 10.4% FWHM (Petrillo et al., 1984). This same group built the first APD-based PET system for small animals. The Sherbrooke Avalanche Photodiode Positron Tomograph consisted of 256 modules, each consisting of a Bismuth Germinate, BGO, crystal coupled to an APD (Lecomte et al., 1996).

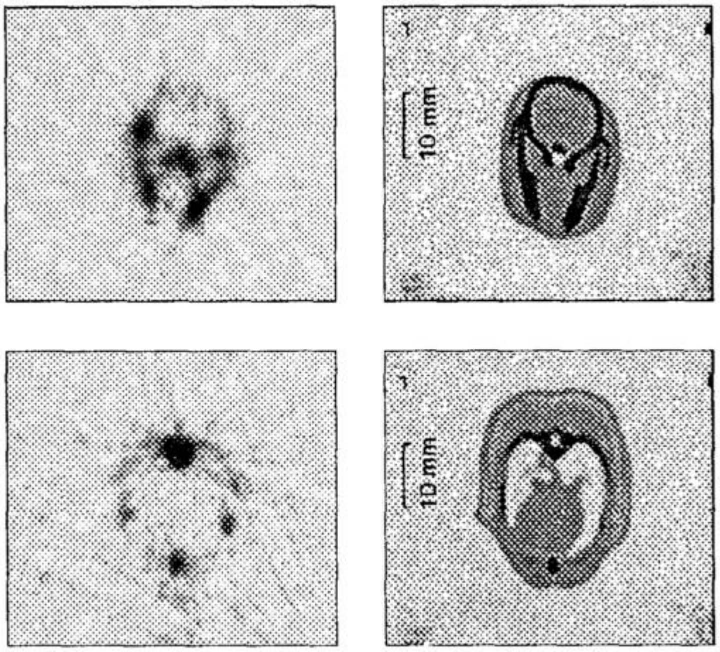

Figure 1-3. Uptake of ^{18}F-flouride within the skull of a 160g Rat obtained with the Sherbrooke Avalanche Photodiode Positron Tomograph (Lecomte et al., 1996)

The introduction of Cerium doped Lutetium Oxyorthosilicate (LSO) created new possibilities for scintillator APD detectors. LSO has light output similar to NaI(Tl) and stopping power similar to BGO but much faster decay time than both, 30-40ns vs 230-300ns (Melcher, 2000), making it a ‘best of both worlds’ scintillation material. This faster decay time allowed for better timing resolution eventually leading to Time of Flight (TOF) capable PET detectors. LSO APD detectors were operated within a magnetic field in 1997 at the University of Munchen, Germany. Placing the detector in a 9.4T magnetic field the group found that the APD output was stable, with no change in gain, energy or spatial resolution (Pichler et al., 1997).

There are several current systems that utilize LSO APD detectors for dual modality PET-MR. The University of Tubingen Simultaneous PET/MRI Small Animal System uses ten modules of 12x12 LSO arrays coupled to APDs. It is designed to fit inside a Bruker 7T ClinScan MRI or Bruker 7T BioSpec 70/30 Ultra Shielded Refrigerated MRI (Judenhofer et al., 2008).

Another system is the MR compatible RatCAP from Brookhaven National Laboratory. This system is composed of 12 modules of 4x8 LSO arrays coupled to APDs and is designed to fit into a 9.4T microMRI (Maramraju et al., 2008).

1.4.2 Silicon Photomultipliers

A progression in the development of the APD is the Silicon Photomultiplier (SiPM), also called a Geiger Mode APD. A SiPM is composed of hundreds to thousands of microcell APDs fixed to a substrate each acting as an isolated APD in the detection process. APDs have what is known as a breakdown voltage, a bias voltage beyond which the gain stops being proportional to photon energy and becomes a fixed quantity, proportional only to bias voltage. APDs operating just above this breakdown voltage are said to be operating in Geiger mode (Saveliev & Golovin, 2000). The microcells comprising the surface of the SiPM are all operated in Geiger mode meaning that the firing of one individual cell does not contain any information on the energy of the photon that triggered it. Scintillation detectors using SIPMs rely on the sum of all microcells fired for one scintillation event to determine the energy of the gamma. In this way the energy resolution of the detector depend on the intrinsic properties of the scintillator and how much optical light was emitted from the absorbed gamma ray. Each microcell has a quenching time, the amount of time required, after a successful avalanche breakdown, before another avalanche can occur. These quenching times are typically tens of nanoseconds (Knoll, 2010). Since each cell has a dead time (quenching time) there must be a sufficient number of microcells to collect a reasonable fraction of the scintillation light leading to decent energy resolution. However, each microcell has a fraction of its surface occupied by a transistor which is effective dead space. Increasing the number of microcells increased the overall dead space on the surface of the SiPM decreasing the detection efficiency of the detector, thus the appropriate number of microcells for a particular SiPM depends on the scintillator it will be paired with.

SiPMs share many of the advantages of typical APDs over the PMT, including small form factor and magnetic field insensitivity, but also show lower gain temperature dependence than APDs as well as lower noise in general. On top of this, SiPMs have a gain comparable with PMTs ($\sim 10^6$), a major advantage over APDs ($\sim 10^4$). A group from Seoul, South Korea, built an MR compatible PET insert based around SiPMs, specifically Hamamatsu Multi Pixel Photon Counters (MPPC). In their design the scintillator arrays are coupled to fiber optic cables bridging a gap between them and the SiPMs. This is intended to reduce interference with the RF needed by the MR (Hong et al., 2012).

1.5 Spatial Resolution of a PET Scanner

The goal of a PET scanner is to obtain a high quality image of a patient/subject. Any image created by a PET scanner has several parameters attributed to it, these include contrast, noise, and spatial resolution. The values of these parameters determines the quality of any particular image. These factors are the complicated result of many details within the scanner hardware and reconstruction software, they are interdependent and often increasing one will negatively affect another. Spatial resolution is a metric measured and assigned to the scanner itself and depends almost entirely on the scanner hardware. The factors that affect the system spatial resolution are; detector width, positron walk, multiplexing, acollinearity, sampling rate, and parallax error (William W Moses, 2011).

Detector width refers to the physical width of a single detector element. This is the dominant factor that determines spatial resolution. An accurate image requires accurate lines of response (LOR) which are created based upon the scintillation crystal of interaction. However once a 511 keV photon has been absorbed by one particular crystal the location is known only to the crystal location and no further information can be gleaned. Thus PET LORs are not exact but rather a probability density of some width. In this way the detector width negatively affects spatial resolution.

As discussed briefly before, the positron annihilation does not exactly represent the location of the radiotracer source of emission. Rather, after emission from the radiotracer, the positron experiences a small walk before capturing an electron, creating an annihilation event resulting in the two 511 keV photons. The magnitude of this factor depends on the radioisotope used (higher average positron energy results in larger ranges), it is unavoidable and results in image blurring ranging from 0.54 mm fwhm to 6.14 mm fwhm for ^{18}F and ^{82}Rb respectively (Cho et al., 1975; Levin & Hoffman, 1999).

In order to combat the error introduced by the detector width (discussed above), crystals can be made thinner. However this comes at a cost of not only system sensitivity but a consideration that it is not practical, both financially and physically (many readout cables), to have one to one readout of scintillation element to photodetector. Since the number of scintillation crystals is usually higher than the number of photodetector elements, especially in small ring diameter systems, there must be some degree of multiplexing. This usually manifests itself in the form of light sharing between crystal elements, where even if the entire face of the crystal is contained within one photodetector element, optical photons will be shared across other crystals and the absorbed gamma can still be positioned into the proper crystal. This multiplexing is always, to an extent, imperfect and results in information loss or the possibility of mispositioned scintillation events.

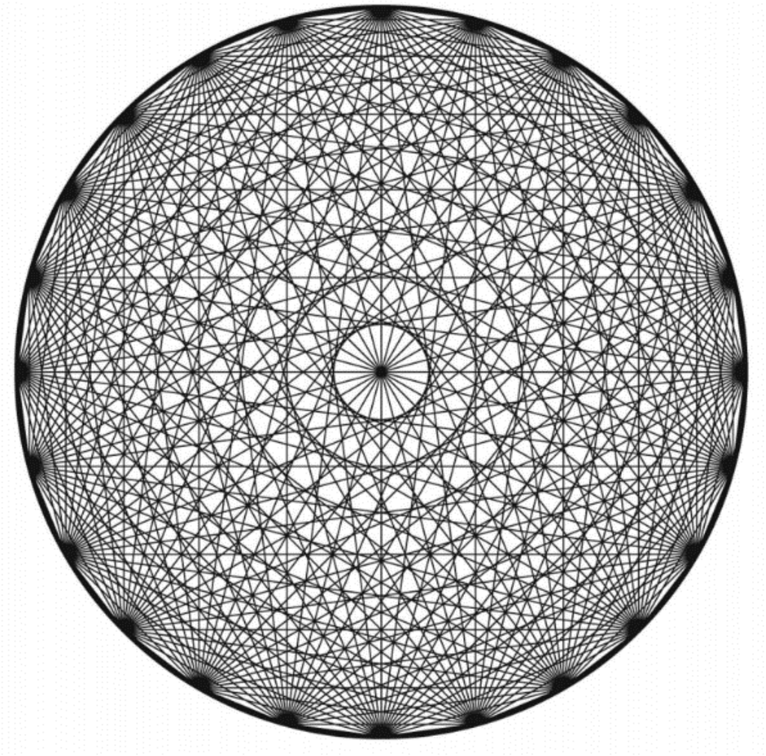

Figure 1-4. Depiction of sampling error showing areas of low and high LOR density (William W Moses, 2011)

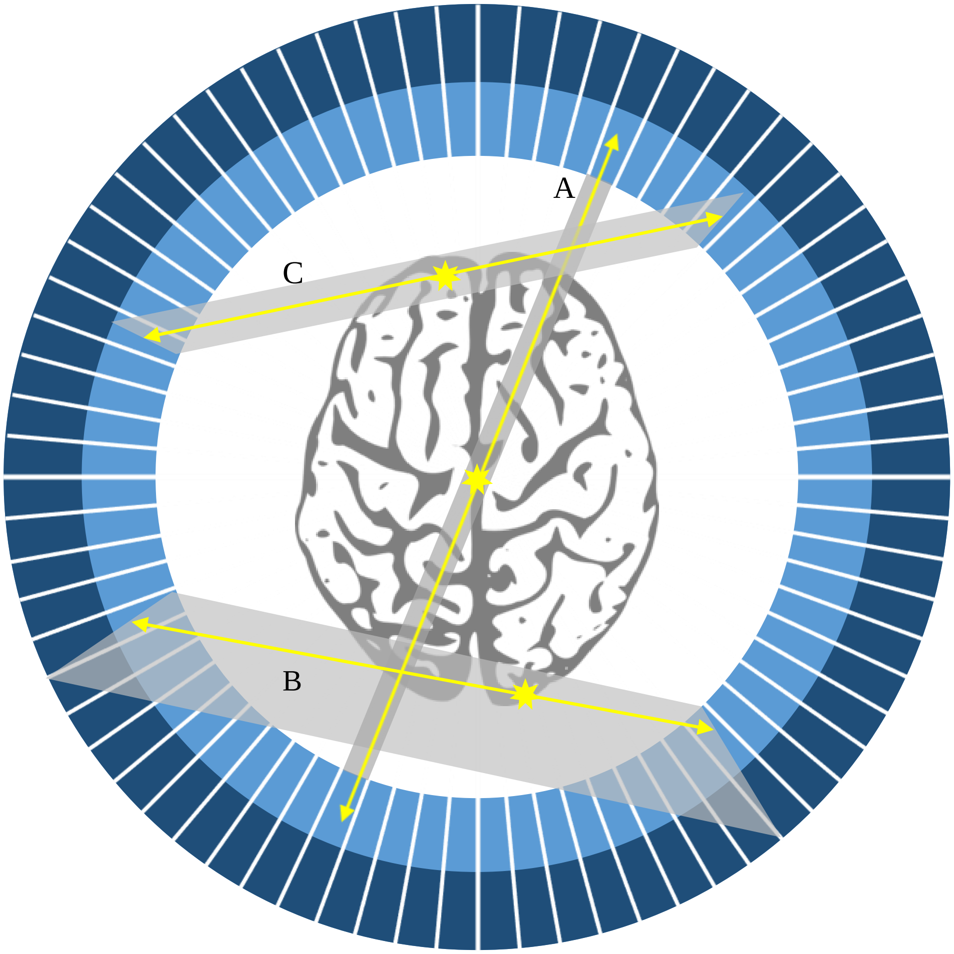

Figure 1-5. A) Center event unaffected by parallax. B) Parallax error shown for off center annihilation event - wide LOR reducing spatial resolution radially. C) Reduced degradation of LOR from DOI information.

Acollinearity refers to the deviation of the photon emission from 180°. When a positron captures an electron it becomes a short lived positronium which decays to become two 511 keV gamma rays 180° back-to-back. However since the positronium has some non-zero kinetic energy when it decays, the angle of emission for the photons is not perfectly 180°. Rather 180° is the mean angle with an acollinearity of 0.2° FWHM (Colombino, Fiscella, & Trossi, 1965; Shibuya et al., 2007). This error, like positron walk, is unavoidable and results in image blurring.

Sampling error refers to the unequal distribution of LORs. Since the LORs are positioned at the center of the crystal elements, there are areas where events cannot be placed, as shown in

Figure *1-4*: the superposition of all possible LORs. This effect has the most impact near the center of the FOV where the LOR density varies the most. This error can be reduced by wobbling the camera around the patient/subject or vice versa so as to move the LORs physically (Suk, Thompson, Labuda, & Goertzen, 2008). Increasing the number of crystal elements adds LORs and also reduces this error.

The last factor that degrades spatial resolution in PET is parallax error. When an annihilation event takes place in the center of the scanner's FOV the scintillation crystal width is the dominant factor that effects the spatial resolution since the incoming gammas will always be perpendicular to the crystal surface. However events that take place radially off center in the FOV are affected proportionally to the degree they are off center. The 511 keV gamma rays will penetrate some degree into the crystals in the detector ring. Since all that is known is the crystal of interaction the LOR that is created for off center events has a width dependent on the projected width of the crystal at that distance off center. Figure 1-5-B depicts this. This wide LOR leads to off center blurring known as parallax error. To reduce parallax error detector designs can supply some degree of depth of interaction (DOI) information to the reconstruction system, shown in Figure 1-5-C. In a DOI detector the absorbed gamma ray can be pin pointed, with varying degrees of accuracy, to a location within the scintillation crystal element instead of defaulting the location to the center of the crystal. This reduces the width of off center LORs and improves the spatial resolution off center in the FOV.

The best achievable spatial resolution for any given PET system is given by:

$$\Gamma = \sqrt{(d/2)^2 + s^2 + (0.0044R)^2} \qquad (mm\ FWHM) \qquad 1.1$$

Where d is the crystal element width, s is the positron walk range, and R is the detector ring radius (William W Moses, 2011).

1.6 DOI Detectors

Clinical whole body PET systems rarely worry about the effects of parallax error since the FOVs are large compared to the scintillation crystal lengths making the degradation in spatial resolution off center low enough not to warrant the extra cost and engineering of a DOI detector. Small ring diameter PET such as pre-clinical, small animal, or dedicated head systems are strongly affected by parallax error and can benefit greatly from DOI information. There are a number of different detector designs that specialize in DOI: Dual ended readout detectors, Individual crystal readout detectors, Monolithic crystal detectors, and Phoswich detectors.

Dual ended readout systems, shown in Figure 1-6-B, utilize photodetectors on both sides of a scintillation element. The depth of interaction is then measured by comparing the proportional signal strength from one scintillation event. Since optical light is spread isotopically, more light, and thus more signal will result from the closer photodetector. Since this design is sharing the light from one event between two detectors it suffers from reduced energy resolution and increased noise. Precise calibration of the photodetector pairs is also required for accurate DOI measurements as the gain directly affects the positioning. Proper construction results in continuous DOI localization, however there is added cost and complexity of adding a second photodetector.

Individual crystal readout detectors, Figure 1-6-C, break traditional scintillation elements into two or more separate elements coupled individually to their own photodetector. Each photodetector/crystal pair acts as a traditional pair would, with reduced sensitivity if the overall crystal length is reduced. Events are localized to crystals through signal readout leading to DOI information. While the dual ended readout supplies continuous DOI, this design is limited to registering events to crystal centers but does not share scintillation light leading to better energy resolution. However, like dual ended readout systems, this design has added complexity and cost.

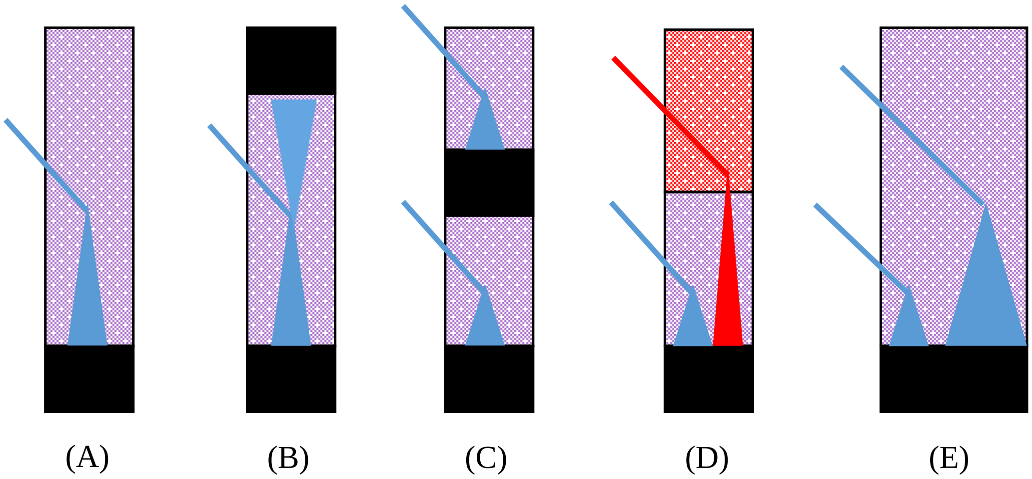

Figure 1-6. Various DOI detectors: A) Standard detector (non-DOI). B) Dual ended readout. C) Individual crystal readout. D) Phoswich detector. E) Monolithic with light spread depicted.

Monolithic crystal designs rely on multiple photodetectors or a position sensitive photodetectors with multiple independent readouts is attached to a single monolithic crystal. The photodetectors being used are then able to measure the extent to which the scintillation light has spread at the detector surface by comparing the values of the independent readouts across the crystal. Events absorbed further from the photodetector will have a larger optical light spread than events closer, shown in Figure 1-6-E, in this way these detectors are able to measure the depth of interaction. While one monolithic block of scintillator is quite simple compared to various other arrays of scintillators, some requiring complex reflector around and in between elements, determining the position of side and corner events can be complicated in this design as the optical light, within the crystal, will dominantly spread inwards (Vinke & Levin, 2014).

Finally, one of the most popular designs is the phoswich, or ‘phosphor sandwich’ (Wilkinson, 1952). In this design the scintillation element is composed of two or more different scintillation materials having measurable differences in their decay times, Figure 1-6-D shows these differences as red and blue with the separate scintillation materials also visible. The emission of optical light from a scintillation crystal has a fast exponential rise followed by a slower exponential decay. The time constants of these two parameters depend on the materials and doping concentrations of activator with the crystal. The layer of interaction is then determined from pulse shape discrimination within the readout electronics determining the decay time of the scintillation light. A major problem with this design is the differences between different scintillation materials. These differences can affect timing and energy resolution if one of the materials has a much slower decay time or light output respectively. However, with new doping techniques it is possible to get two materials that have very similar properties, and fast decay times that vary by only 20-30ns (Spurrier et al., 2008). One of the first commercially available phoswich systems was the Sedecal Argus (GE Vista) hybrid small animal PET/CT scanner. This scanner was composed of a top layer of cerium doped LYSO and bottom of cerium doped GSO having dimensions 1.45 x 1.45 x 7, 8 mm^3 for top, bottom respectively. 13x13 crystal arrays coupled to Hamamatsu R8520-C12 PMTs arranged in 2 rings of 18 modules made up the scanner. This scanner used decay time differences to identify the layer of interaction with the LYSO and GSO having decay times of 40 and 60 ns respectively (Canadas et al., 2010; Wang, Seidel, Tsui, Vaquero, & Pomper, 2006).

1.7 The Flood Histogram

Of critical importance to image reconstruction in PET is the calibration of light spread pattern in the scintillator block to physical crystal location. When a 511 keV gamma ray is absorbed by a scintillator the isotropic emission of light is piped down the particular crystal of interaction but also, to a lesser degree, shared with neighboring crystals leading to a spread of light across multiple photodetector elements. As stated before there is rarely one to one coupling of crystal element to photodetector due to space and complexity limitations, instead detectors rely on optical multiplexing to readout arrays of scintillation crystals with a small number of photodetector elements. One of the first block detector designs was introduced by M. Casey and R. Nutt, in 1986, which was composed of a 4 x 8 BGO array coupled to four PMTs (Casey & Nutt, 1986). Figure 1-7 shows a typical detector element for a PET scanner using common scintillator material and PMTs as photodetectors. In this detector, a scintillation event will result in optical light of varying intensities striking all four of the PMTs. This results in four signals (A, B, C, and D) each having an amplitude proportional to the number of optical photons the respective PMT detected. The gamma ray is then located by using a center of mass approach shown in equation 1.2. This equation is essentially identical to traditional Anger logic used in a Gamma Camera (Anger, 1966) the difference being that there are many PMTs in a Gamma camera which are further multiplexed down using a resistive network into four signals. Detectors using APDs or SiPMs usually work in a similar manner with the APD cells or micro cells being summed into channels.

$$X = \frac{(A+B)-(C+D)}{(A+B+C+D)} \qquad Y = \frac{(A+C)-(B+D)}{(A+B+C+D)} \tag{1.2}$$

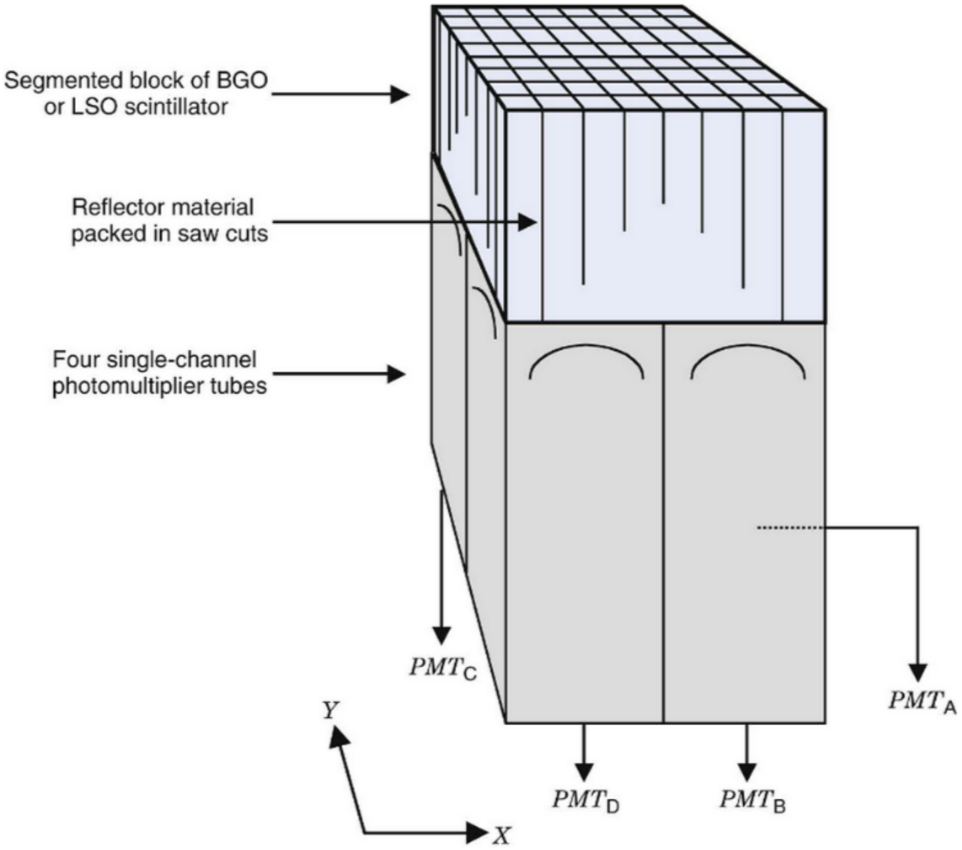

Figure 1-7. Typical detector element showing a scintillator block coupled to four PMTs (Cherry, Sorenson, & Phelps, 2012, p. 324).

When a detector block, such as the one shown in ***Figure 1-7***, is uniformly irradiated each event is given an X and Y position on the detector surface via an equation the same as, or similar, to equation 1.2. These positions can then be binned into a 2D histogram known as a Flood Histogram. Figure 1-8 shows a flood histogram acquired from an 8x8 scintillation crystal array (image courtesy of UC Davis). The individual crystal elements are distinguishable but also immediately apparent is the 'pin cushion' distortions pressing the sides of the histogram inward. The crystal block this flood histogram originated from was a square block of equal dimension scintillator crystals with reflective material between each. The reflective material is a means of preserving the number of optical photons collected by the detector helping to preserve the energy resolution. The distortions in the flood histogram are the result of a complex product of readout electronics, capacitance of the photodetector (APD), how the optical light

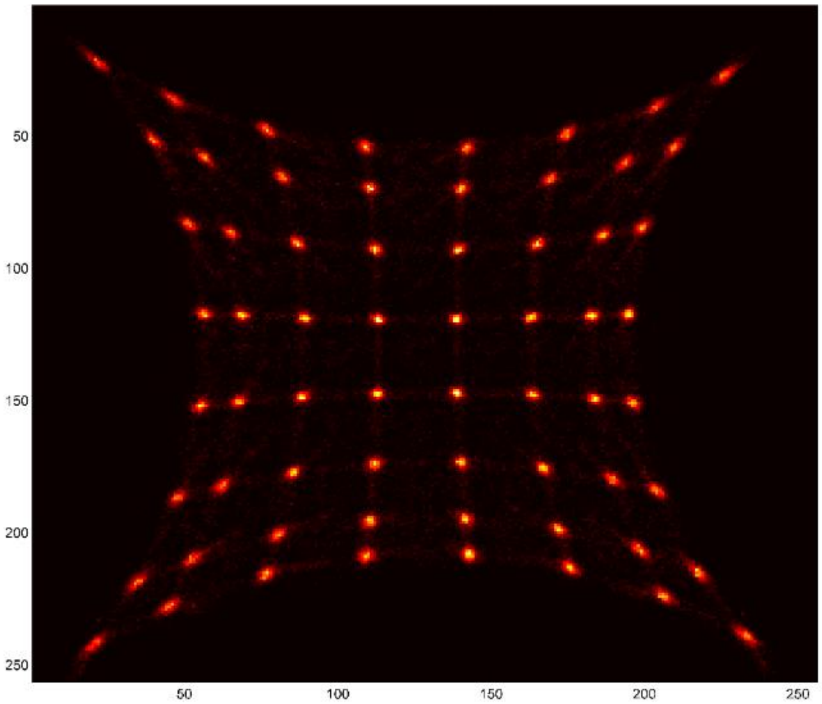

Figure 1-8. Flood histogram from an 8x8 scintillator array. Visible is the pin cushion distortion from uneven light distribution.

is transmitted within the crystal array, and the center of mass positioning equations. When a gamma ray is absorbed by one of the edge crystals the subsequent optical photon emission is shared dominantly inward due to the reflective material coating the outside of the array. This results in a positioning of the event that is closer to the center of the array than truth. The corner crystals do not experience the same degree of distortion since the decrease in nearest neighbors also decreases the light sharing. The side, and especially the corner, crystals also suffer from reduced energy resolution from Compton scattering events resulting in the photon leaving the crystal array and not deposition its full energy. Compton scatter is a source of noise for all crystals in the flood histogram. A scattering event within the center crystals is more likely to still be completely absorbed by the array than a side crystal. This results in the possibility of mispositioned events but preserves energy resolution since most of the energy / optical light is still deposited / detected.

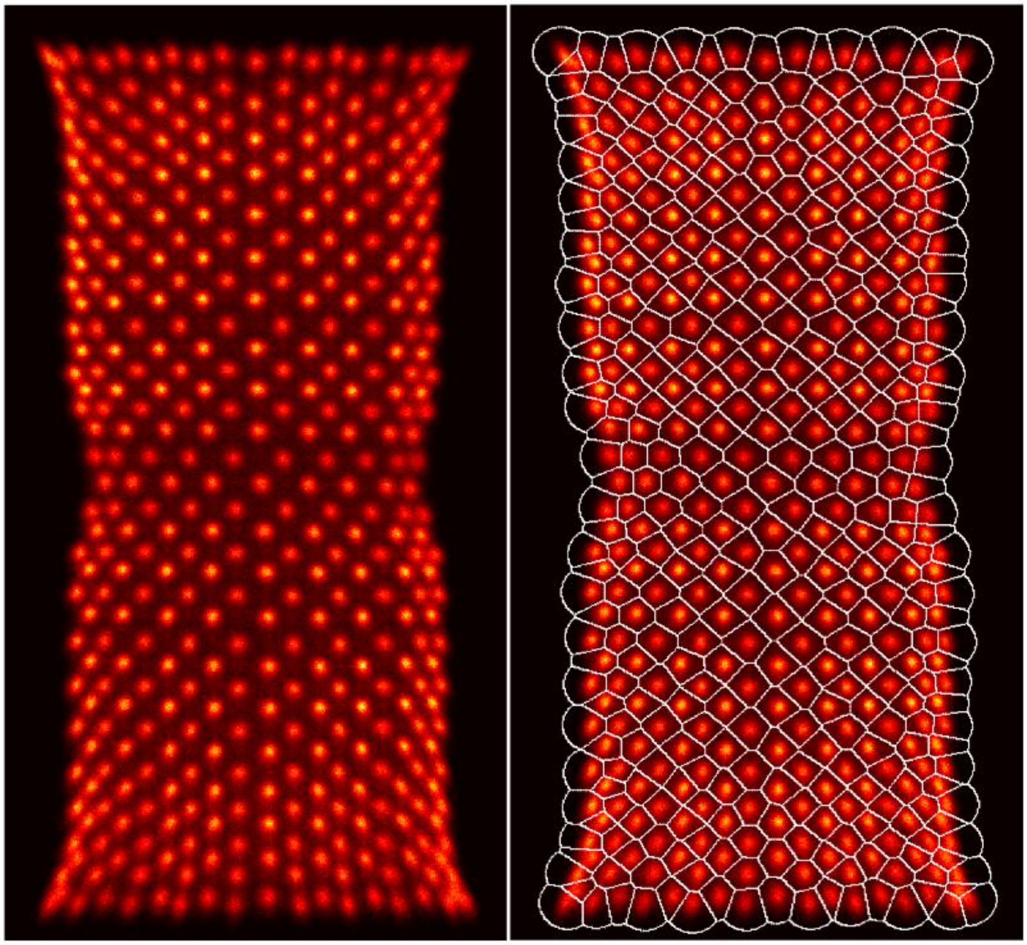

Figure 1-9. *(right)* A 409 crystal flood histogram with *(left)* the borders of its corresponding CLUT visible

For image reconstruction each event must be assigned to its crystal of interaction. This is most commonly accomplished by calibrating each detector's flood histogram with a crystal lookup table (CLUT). The CLUT is a 2D map of crystal zones corresponding to positions on the flood histogram. During an image acquisition, instead of building a flood histogram, the gamma ray (i, j) position is simply mapped with the CLUT immediately assigning it to a crystal. Figure 1-9 shows the flood histogram of a 409 crystal detector module along with the segmented zones of the CLUT on the right. Each of these zones represents a crystal number (in this case from 1 to 409) and any event falling within them is assigned the specific number and its associated (X, Y) location. For quality images, and accurate reconstruction, it is crucial that the CLUT be an accurate map of the crystal responses on the flood histogram to the physical crystals in the scintillator array. This requires segmenting the flood histogram into crystal regions, a standard step of PET detector calibration. This segmentation is usually a manual, time consuming, process as even small ring diameter PET scanners can have thousands of crystal elements.

1.8 Flood Segmentation Algorithms

Manual flood segmentation usually involves the user clicking points on a screen to identify the crystal centers on the flood histogram. This process quickly becomes time consuming and tedious for systems with thousands of crystal elements typical of modern PET systems. On top of this, while the human eye excels at pattern recognition – useful for recognizing deformations in the flood, the crystal center may more accurately be located with a fitted distribution and software. For these reasons several methods/algorithms, summarized in this section, have been explored to segment detector flood images and reduce the burden of creating CLUTs and/or to improve accuracy. Many of these algorithms vary in core principle and range from semi-automatic, requiring substantial manual intervention, to fully automatic, robust but requiring training data. A collection of the most prevalent methods for flood segmentation and crystal identification makeup the following subsections.

1.8.1 Watershed

Methods relying on a watershed algorithm are not concerned with locating the crystal centers but rather segmenting the flood into regions. Based on the geological idea from which it derives its name, a watershed algorithm mimics the water flow relief of a topological area experiencing rainfall (Vincent & Soille, 1991). This algorithm is a staple of standard image segmentation in a variety of fields. Usually the flood is smoothed before applying this algorithm, then the inverse intensities can be thought of as drainage or catchment basins and a watershed line is placed between them, as depicted in Figure 1-10, representing the flow of water into one basin or another. In this way an entire flood histogram can be segmented.

Watershed algorithms are known to be fast but do not guarantee the correct number of regions and rely on significant preprocessing to smooth out anomalies lest an unwanted basin be added to the flood. An example of flood segmentation using a watershed is shown in Figure 1-11 (Xiaowen et al., 2008).

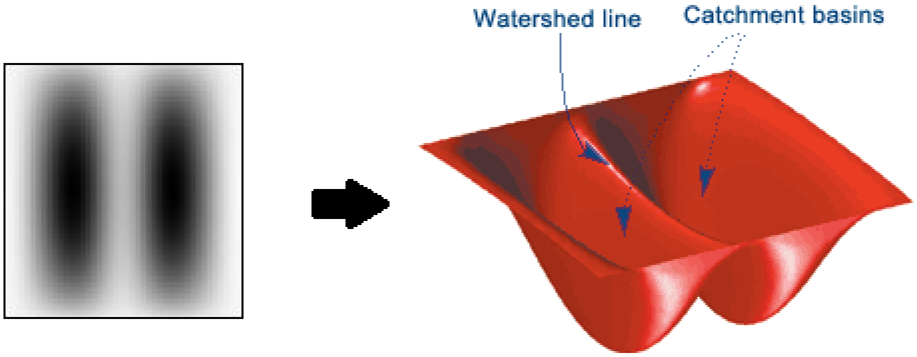

Figure 1-10. Example of a Watershed line divide between two areas of intensity or catchment basins. Reprinted from mathworks.com

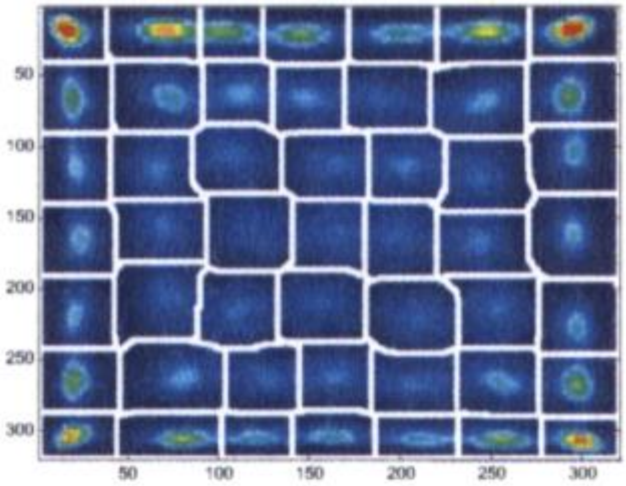

Figure 1-11. Watershed algorithm used to segment a 7x7 crystal flood histogram (Xiaowen et al., 2008).

1.8.2 Fourier Method

Another flood segmentation method developed by (Chaudhari et al., 2008), involves filtering / identification of the crystals in Fourier space. In this method, intensities across the flood are corrected to be uniform, then a discrete Fourier transform is used to filter the flood histogram and create a template which corresponds to the crystal arrangements of the physical array and is also a lower order spatial approximation of the flood histogram. This template is created such that it lends itself easily to proper segmentation / crystal identification. Lastly the template is deformed to match the flood using an intensity based warping scheme with polynomial bases such that an error function is minimized.

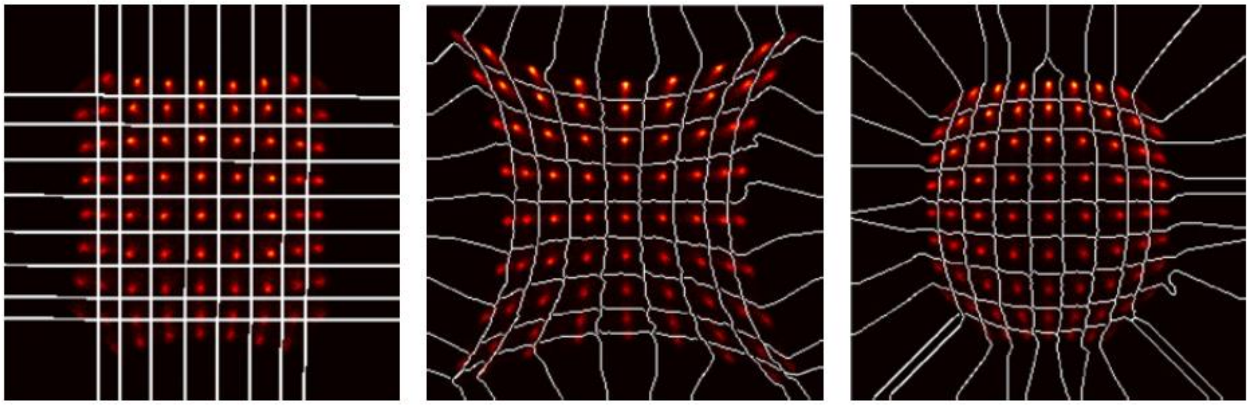

Figure 1-12. Fourier segmentation method applied and warped to different flood deformations

1.8.3 Neural Networks

Neural networks are an aspect of machine learning involving collections of nodes and the corresponding connections between them allowing passage of information from node to node. In this way neural networks mimic a biological brain in that they mathematically resemble a ganglion of neurons. A neural network is capable of learning, in a sense, by applying training data to shift weights corresponding to different nodes preferential to certain outcomes. When applied to flood crystal identification the system is ‘taught’ which events correspond to which nodes (crystals) with training data. This is both a strength and a weakness of this approach in that the system can adapt to various levels of flood deformation, by learning, but also can require extensive amounts of training data, supplied by the user, to be robust. This approach has been used with the Siemens Inveon PET scanner

(Hu, Atkins, Lenox, Castleberry, & Siegel, 2006) and achieved very accurate results for that particular scanner. However this group experienced stability problems in the neuron locations due to the training data used showing the sensitivity of this approach to the quality of training data. The training data also lead to dead neurons, or neurons that are never allocated training data since their initial position is too far removed from any incoming data. Figure 1-13 shows results from the Siemens Inveon neural network, the red dots represent the 400 neurons (20x20 crystal array). The left image shows the initial locations before application of the training data while the right shows the final results. While the right image shows that the majority of neurons seem to be positioned properly there are visible mistakes (top right corner).

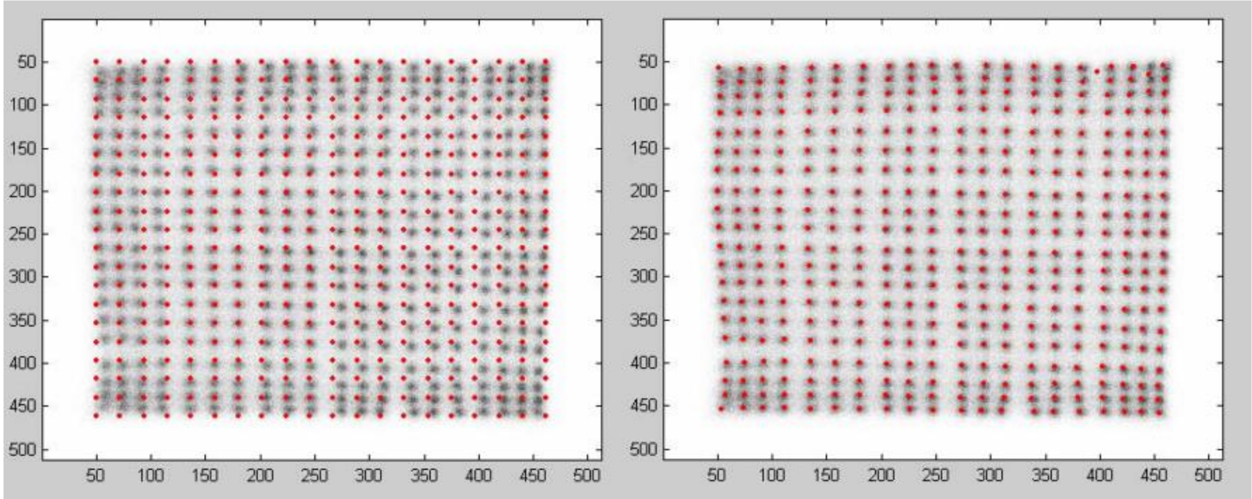

Figure 1-13. Inveon detector block crystal identification. Left: Initial positions of neurons in neural network. Right: Final neuron positions after training (Hu et al., 2006).

1.8.4 Gaussian Mixture Models

As stated before, PET detectors are usually a 2D array of scintillation crystals coupled to a photodetector. This configuration leads to events being positioned on the x-y plane. With enough counts, individual crystal responses are then modelled extremely well with a 2 dimensional Gaussian distribution. A Gaussian Mixture Model (GMM) is, as the name suggests, multiple Gaussian distributions, in the case of flood histograms, used to represent the individual crystal responses. Algorithms based on GMM rely on maximum likelihood (ML) iterations to converge to an optimum fitting of the Gaussians parameters. These parameters are usually the vector means as well as the covariance matrices for each distribution. This approach has several limitations, one being that it can take many iterations to converge, possibly making it time consuming. The number of iterations is directly affected by how close the starting estimates of the Gaussian parameters are to the converged parameters. ML for GMM is usually very sensitive to initial starting parameters. The method is guaranteed to converge to an optimum mixture of components (parameters), but with a poor choice of starting conditions it can converge to a local optimum. This severely limits the robustness of algorithms based on GMMs.

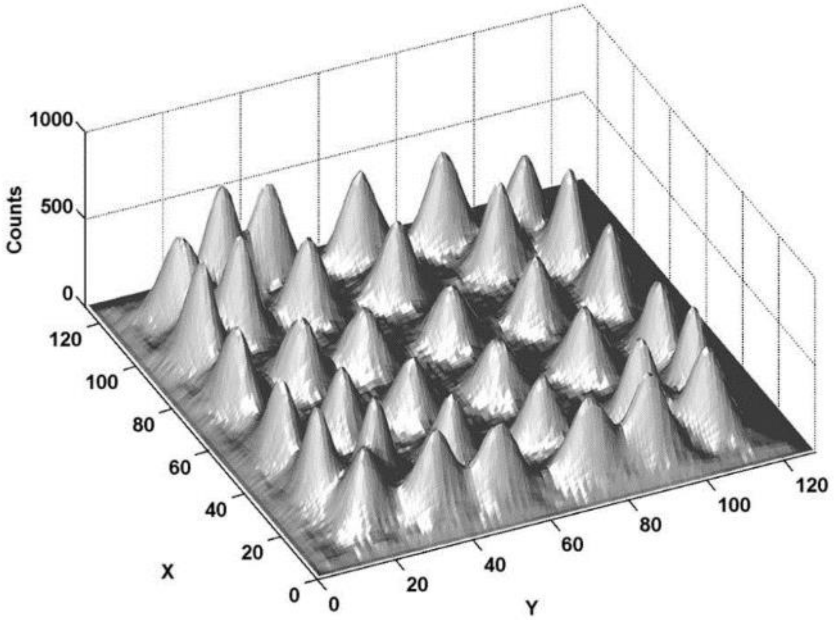

Figure 1-14. Smoothed flood histogram shown in 3D. Crystal responses are to be modelled with a GMM (Stonger & Johnson, 2004).

A GMM approach has been utilized by a few groups. (Stonger & Johnson, 2004) used this method successfully on a GE Discovery PET system which has detector elements composed of a 6x6 array of BGO crystals coupled to 4 PMTs. The flood histograms in this case are relatively simple and subject to significant preprocessing and smoothing (Figure 1-14) before the ML GMM algorithm is applied. On top of this the initial estimates for starting parameters are trained with data to get a more accurate position for each individual detector block.

This approach was also used in a DOI detector by (Yoshida, Kimura, Kitamura, & Murayama, 2004). In this detector the scintillator array is divided into four regions composed of two different scintillator materials. The layer of interaction is identified by both location of event in the flood histogram and decay time characteristics, shown in Figure 1-15.

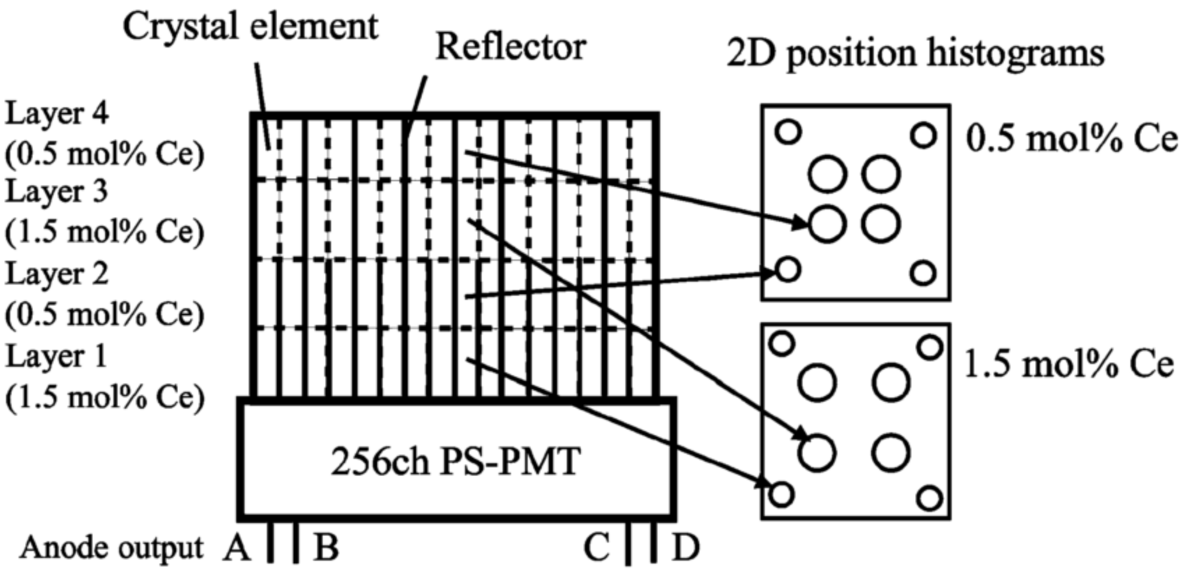

Figure 1-15. Four layer detector design utilizing both phoswich and position for layer identification (Yoshida et al., 2004).

This design leads to a very complex flood histogram, as shown in Figure 1-16. Individual detector elements are processed individually. The broad cluster of eight regions is identified first then further clustered into the eight separate regions. This method obtained good results for individual detector elements but was not practical on the whole detector block due to the varying level of quality the crystal responses show near the edges and the number of parameter that must be estimated for the GMM.

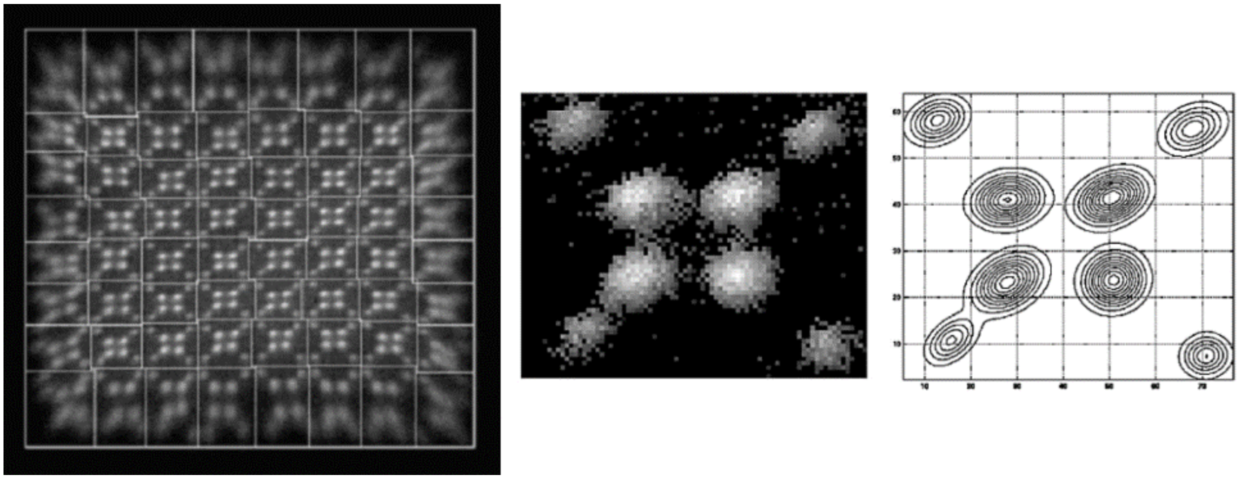

Figure 1-16. Left: Full detector block. Middle: Response from one detector element. Right: GMM fit to Middle (Yoshida et al., 2004).

2 Crystal Identification Algorithm

2.1 Overview

This chapter describes the main components of the flood segmentation algorithm created for calibration of a small animal, MR compatible, PET system developed by our group. The purpose and aims for creating the algorithm are discussed before an in depth explanation of the theory behind the algorithm. Finally in section 2.3, the algorithm is explained in detail along with pseudo code representing the structure of the algorithm found in this groups MATLAB program.

2.2 Theory behind algorithm

The algorithm is mainly based on a Gaussian Mixture Model (GMM) approach however it also utilizes Thin Plate Splines (TPS) as a mapping function. This algorithm aims to overcome the inherent initial condition sensitivity experienced by other GMM algorithms by letting individual Gaussians converge slowly in an expanding region of interest and using these converged Gaussians to create a TPS map function which is applied to points that have yet to be fit. Applying the TPS map to inactive points alters the starting position at which they enter the GMM. Since the TPS map is created from already converged points the starting position of inactive points are more accurate increasing the stability of the GMM.

2.2.1 Purpose / Mission

As stated before, work on this algorithm initially started as part of a calibration package for a small animal MR compatible PET insert (Stortz et al., 2013). This system has 16 detector modules each with 409 crystals. Due to intricate reflector configurations within the crystal lattice the subsequent flood histograms are distorted in unique but similar patterns, Figure 1-9 shows an example of one such flood. Flood histogram segmentation was initially manual, which involved clicking on all 409 crystal locations for all modules, proving to be a tedious and time consuming task leading to work on an automatic algorithm for segmentation / crystal identification.

Basic requirements for the algorithm included:

- **Speed** – Must require significantly less than the time required for manual segmentation.
- **Robustness** – There are a variety of distortions, of varying magnitude, unique to the flood histograms used for testing. The algorithm should successfully identify crystals in these difficult regions.
- **Accuracy** – Should identify the location of crystals to equal or greater accuracy than manual segmentation.
- **Minimal user input** - Should use the minimal amount of initial data and user correction throughout algorithm.
- **Versatility –** The ability to readily apply the algorithm to floods originating from other detectors with different geometries and/or dimensions.

A neural network approach was unattractive due to the need for training data, which can vary in quality, adversely affecting the algorithms accuracy. However, if data is readily available for use, it was decided that it should not be disregarded.

2.2.2 EM for GMM

The Expectation Maximization (EM) algorithm is a technique that can be used in Maximum Likelihood (ML) when analytical solutions are not possible. An explanation of the EM algorithm begins with a general definition of ML:

Given there is a probability density function $p(x|\Theta)$, where x is an independent variable and Θ is a set of parameters that govern the behavior of the function. For example in the case where p is a Gaussian function Θ could represent the means a covariance matrices. We then introduce a data set X of size N, ($X = \{x_1, x_2, \ldots x_N\}$) that we claim is represented by the density function p. The density function across the samples X is then:

$$p(X|\theta) = \prod_{i=1}^{N} p(x_i|\theta) = L(\theta|X) \qquad 2.1$$

Where $L(\Theta|X)$ is known as the likelihood for the set of parameter Θ. As the name suggests, the aim of ML is to maximize this likelihood function. Usually the logarithm ($log(L(\Theta|X))$, also known as the log-likelihood, is used as it lends itself to easier analytic solutions. This is accomplished by finding a particular set of Θ that results in a maximum likelihood of the set X, or in other terms, the set of parameters Θ, that *fit* the data X, the best. In simple cases this maximization can be accomplished with the standard technique of setting the derivative of $log(L(\Theta|X)$, with respect to Θ, to zero and solving for the parameters within Θ. However in more complicated scenarios, where p is not one single function but made up of many (possibly) different functions, an analytical solution is sometimes not possible and other methods, such as the EM algorithm, must be used to find a maximum likelihood.

The EM algorithm is usually used in ML scenarios where not only is an analytic solution not possible but there are also values missing from the data set X. A simple example of missing data is to imagine a one dimensional set of data values (x-axis) which are sampled from a Gaussian distribution. The aim would be to maximize the likelihood of a Gaussian distribution over the point set by finding the optimal mean and variance. However we do not have the probabilities associated with each point (one can think of these as the y-axis values) when they were sampled from the supposed distribution. Each x-value in the data set is missing its respective y-value. Scenarios like this involving missing data, where one must still estimate or fit a function, are quite common since usually the data that is missing would come from the function that you are attempting to fit. The EM algorithm attempts to bypass this problem by filling in the missing data by estimating parameters for the distribution. It is formally broken into two steps, the expectation step or E-step, and the maximization step, or M-step. Initially the unknown parameters, Θ, are guessed or estimated and passed to the E-step, where, using Θ one can calculate the *expected* likelihood of the function which is then passed to the M-step. Now there is an expected likelihood with no missing values in the data one can *maximize* the function to get new estimates of the function parameters Θ. If the initial guess for the parameters Θ was correct the expected likelihood will be the true likelihood, if the initial guess was off, the likelihood serves as a lower bound and the new parameters, calculated in the M-step, can be passed back to the E-step to start the process anew. The EM algorithm is an iterative process continuously looping through E-steps and M-steps until there is convergence of the expected likelihood (Dempster, Laird, & Rubin, 1977).

A Gaussian mixture model (GMM) is a type of probability density function that EM is commonly applied to, and of special interest to this work. As one would expect, a GMM is two or more Gaussian functions summed under the title of one function. GMMs are extremely well suited, and often applied, to clustering problems where the Gaussians fit to points in space dictate the ownership of the respected points. Figure *2-1* depicts a 3 component GMM being applied to a set of 2D points, showcasing the clustering abilities.

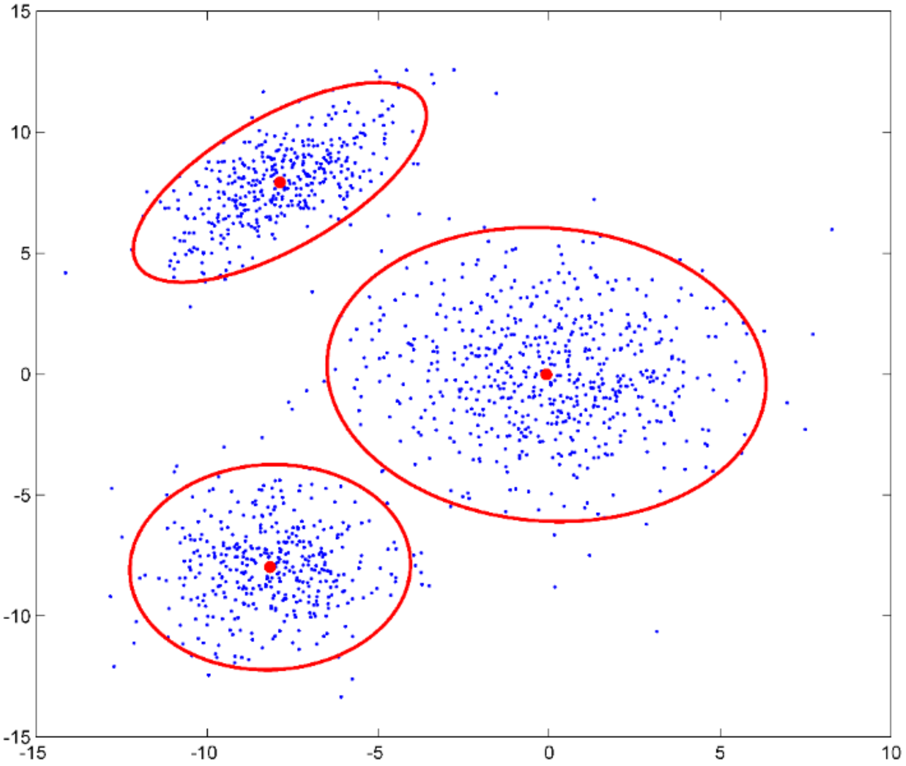

Figure 2-1. Example of a 3-component 2D GMM applied to randomly generated data (with Gaussian PDFs).

As stated before, the EM algorithm is routinely used to estimate the ML parameters for a GMM over data sets such as the one depicted in Figure *2-1*. The EM algorithm applied to GMM is formally defined as follows:

Defining a data set C composed of n points and a GMM with k mixture components and parameters Θ where Θ_j is comprised of w_j, μ_j , Σ_j for $j = 1 \ldots k$, where w_j is the normalized weighting of each Gaussian, μ_j is the mean vector of each Gaussian, and Σ_j is the covariance matrix of each Gaussian. One of the Gaussians in the mixture over the data set C can then be written $N(C| \mu_j , \Sigma_j)$ the multivariate Gaussian function:

$$N(x|\mu,\Sigma) = \frac{1}{\sqrt{(2\pi)^u|\Sigma|}}\exp\left(-\frac{1}{2}(x-\mu)^T\Sigma^{-1}(x-\mu)\right) \qquad 2.2$$

Where u is the dimension of the data (and also the multivariate Gaussian) and |Σ| represents the determinant of the covariance matrix. Before the iteration cycle of the EM algorithm starts the initial parameters in Θ must be set by either estimating or randomly assigning values. The algorithm then follows an E-step, M-step iteration cycle with the m^{th} iteration defined as follows.

E-Step for: $i = 1 \ldots n,\ \ j = 1 \ldots k$

$$\gamma_{ij}^{(m)} = \frac{w_j^{(m)} N\left(C_i | \mu_j^{(m)}, \Sigma_j^{(m)}\right)}{\sum_{l=1}^{k} \left(w_l^{(m)} N\left(C_i | \mu_l^{(m)}, \Sigma_l^{(m)}\right)\right)} \qquad 2.3$$

$$q_j^{(m)} = \sum_{i=1}^{n} \gamma_{ij}^{(m)} \qquad 2.4$$

Here γ is an n x k matrix representing the normalized correspondence (or value) of all points to all Gaussians in the mixture and q, being the sum of the columns of γ, represents the un-normalized weighting of each Gaussian. These two calculations (equations 2.3 and 2.4) make up the estimation step where the EM algorithm estimates the missing variables, in this case the correspondences of each point to each Gaussian. Next, in the maximization step, the algorithm uses these estimations to calculate the new distributions parameters $\Theta^{(m+1)}$.

M-Step for: $j = 1 \ldots k$

$$w_j^{(m+1)} = \frac{q_j^{(m)}}{n} \qquad 2.5$$

$$\mu_j^{(m+1)} = \frac{1}{q_j^{(m)}} \sum_{i=1}^{n} \left(\gamma_{ij}^{(m)} C_i\right) \qquad 2.6$$

$$\Sigma_j^{(m+1)} = \frac{1}{q_j^{(m)}} \sum_{i=1}^{n} \left(\gamma_{ij}^{(m)} \left(C_i - \mu_j^{(m+1)}\right)\left(C_i - \mu_j^{(m+1)}\right)^T\right) \qquad 2.7$$

At the end of each EM loop the overall log-likelihood is calculated as

$$L^{(m+1)} = \frac{1}{n}\sum_{i=1}^{n} log\left(\sum_{j=1}^{k}\left(w_j^{(m+1)} N\left(C_i|\mu_j^{(m+1)}, \Sigma_j^{(m+1)}\right)\right)\right) \qquad 2.8$$

and compared to the previous iteration's log-likelihood ($L^{(m)}$), such that if $|L^{m+1} - L^{m}| < \varepsilon$, where ε is a user defined preset threshold, the algorithm is deemed converged and the cycle is stopped. One of course must calculate $L^{(o)}$ with the initial Θ parameters before the iterations start so the first iteration can be compared (Bilmes, 1997; Gauvain & Lee, 1994).

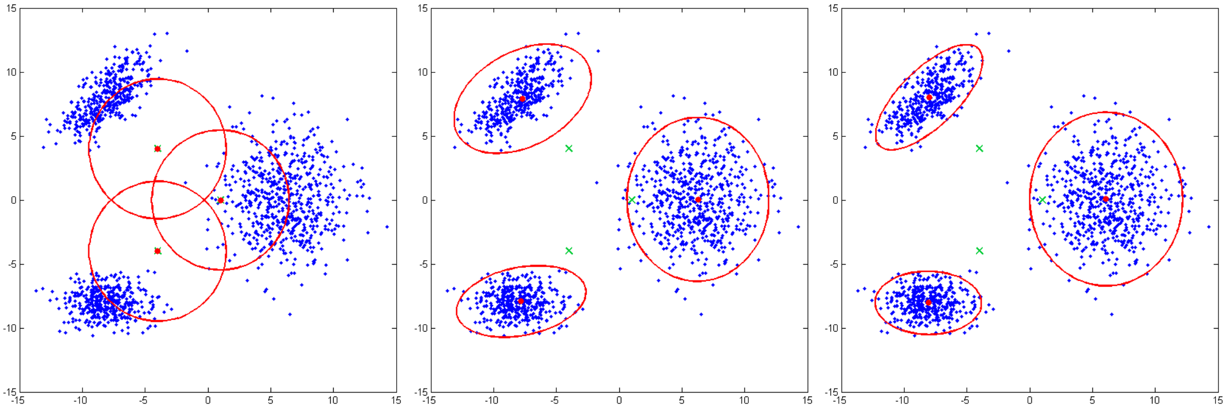

Figure 2-2. Progression of 3 component GMM. Current means shown as red dots, 95% confidence shown as red line, initial means shown as green X's. From left to right are iterations 1, 3, 5 respectively.

Figure *2-2* shows the progression of a 3 component GMM from initialization to convergence. The simplistic data shown in blue has three clearly visible clusters that one can easily predict Gaussian functions to represent. The left most figure shows the initial Gaussians used to start the EM algortithm, all symmetric and located in relative positions similar to the actual clusters in the data. The third and fifth iterations are visible in the middle and right figures respectivly showing the progression of the algorithm. By the fifth iteration the algorithm has converged to below a 10^{-5} log-likelihood difference and further iterations were deemed unnessassary by the user. While Figure *2-2* showcases the strength of the EM algorithm in not only locating the proper positions of the GMM components, but the appropriate covariances as well, it must be stated that the starting parameters in this case were ideal.

In cases where the starting parameters are not ideal, consequences can range from requiring more iterations to incorrect convergence. Sensitivity to starting parameters is a limitation of the EM algorithm, magnified with complex or large GMMs. An example of this sensitivity is shown in **Figure 2-3**.

While the EM algorithm is guaranteed to converge to an optimum likelihood, appropriate initialization is needed lest the algorithm converge to a local optimum resulting in a GMM which poorly represents the data. **Figure 2-3** shows the same distribution initialized with two different sets of starting parameters. The data in this case is noticeably more complicated than the data used in **Figure 2-2** having clusters overlapping. **Figure 2-3** (a) shows adequate starting parameters leading to a convergence in (b) that correctly represents the data. Conversely, (c) shows inadequate starting parameters that lead to (d), a GMM where one of the components is completely neglected in favor of larger component spanning two clusters. The convergence in (d) clearly misrepresents the data and is a product of starting conditions too far-removed from the likelihood maxima best representing the data (b), and closer to a local maxima resulting in (d). This shows a serious limitation of GMMs when used for clustering (or crystal identification in PET): How to prevent, or detect / correct convergence to local optima especially in complex data with hundreds of clusters like many PET detectors would have. Solutions vary from hard coding catches within the algorithm to restarting the entire process with new parameters.

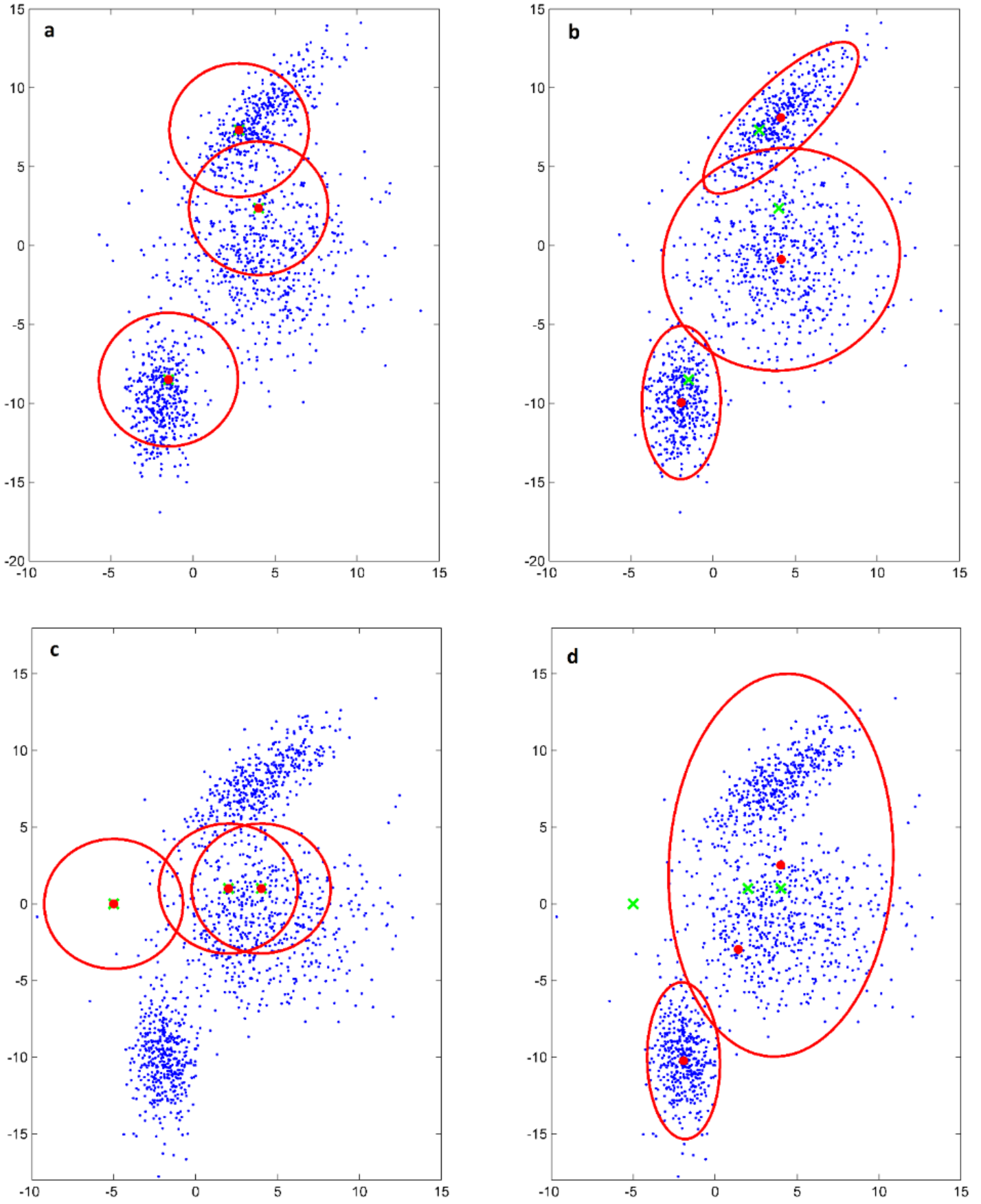

Figure 2-3. Depiction of GMM starting parameter sensitivity. Starting parameters (a) that lead to proper convergence in (b). Poor starting parameters (c) leading to incorrect convergence (d). Current means shown as red dots, 95% confidence shown as red line, initial means shown as green X's.

2.2.3 TPS

Thin plate splines (TPS) are basis functions for representing maps from $\mathbb{R}^2 \rightarrow \mathbb{R}^2$. TPS maps are created with a known correlation between an initial point set, P, and a target point set, V, both being sets of (x,y) points of size n (Bookstein, 1989). The result of the TPS mapping is a function, $f(x,y)$, such that $V = f(P)$. However, the mapping function $f(x,y)$ is not limited to the point set P, and can be applied to any point set in $\mathbb{R}^2$. The name (Thin Plate Spline) comes from the analogy to bending a sheet of metal at certain points resulting in an overall warped sheet. Outlined below is the creation of the TPS map function from the point sets P and V:

As stated before we must start with two point sets, in $\mathbb{R}^2$, of equal size and known correspondence, the initial point set P and the target point set V, such that $P_i = (x_i, y_i)$. We then have the aim of creating a map function $f(x,y)$ such that $V = f(P)$. We define an intermediary function:

$$U(r) = r^2 \log(r^2) \tag{2.9}$$

Where:

$$r_{ij} = \left|P_i - P_j\right| \tag{2.10}$$

Then defining the set of matrices, as well as their respective dimensions (blue text):

$$U(r_{ij}) \xrightarrow{yields} K_{ij} = \begin{bmatrix} 0 & U(r_{12}) & \cdots & U(r_{1n}) \\ U(r_{21}) & 0 & \cdots & U(r_{2n}) \\ \vdots & \vdots & \ddots & \vdots \\ U(r_{n1}) & U(r_{n2}) & \cdots & 0 \end{bmatrix}, n \times n \tag{2.11}$$

$$B_i = [\,1 \mid P_i\,] \xrightarrow{yields} B = \begin{bmatrix} 1 & x_1 & y_1 \\ 1 & x_2 & y_1 \\ \vdots & \vdots & \vdots \\ 1 & x_n & y_n \end{bmatrix}, n \times 3 \tag{2.12}$$

$$L = \begin{bmatrix} K & B \\ B^T & 0 \end{bmatrix}, (n+3) \times (n+3) \tag{2.13}$$

$$Y = [V \mid 0 \quad 0 \quad 0]^T, (n+3) \times 2 \tag{2.14}$$

$$L^{-1}Y = \left[W \mid a_1 \;\; a_x \;\; a_y\right]^T, (n+3) \times 2 \qquad 2.15$$

It should be noted that in equation 2.13 the ‘0’ represents a 3×3 matrix of zeros. Having obtained the matrix from equation 2.15 (of size $(n+3)\times2$ where the last three elements, of each column, are a_1 a_x a_y and represent the affine components of the transformation) we can define the TPS mapping function f as follows:

$$f(x,y) = a_1 + a_x x + a_y y + \sum_{i=1}^{n} w_i U\big(P_i - (x,y)\big) \qquad 2.16$$

Where the vector W is composed of elements w_i *for* $i = 1 \ldots n$. This form may seem confusing, it is important to remember that the output of the function f is a new point (x', y') which has been mapped in the manner according to $P \rightarrow V$. However, equation 2.16 is not the most convenient form of the mapping function f for applications to whole point sets. Given one has already created the mapping function f from point set P to V, and now wishes to apply the map to a new point set M of length m, we define two new intermediary matrices:

$$A_{ij} = U\big(\mid P_j - M_i \mid\big), m \times n \qquad 2.17$$

$$N_i = [\,1 \mid M_i\,], m \times 3 \qquad 2.18$$

Where ‘1’ represents a column vector of length m composed of ones. Using this new matrix we can define a new form for the mapping function f based on full point sets:

$$f(M) = [A \;\; N] \; L^{-1}\, Y \;, m \times 2 \qquad 2.19$$

This form (equation 2.19) is equivalent to equation 2.16 but is far more convenient to apply to code and large point sets. To further aid the TPS theory explanation, an example is laid out below.

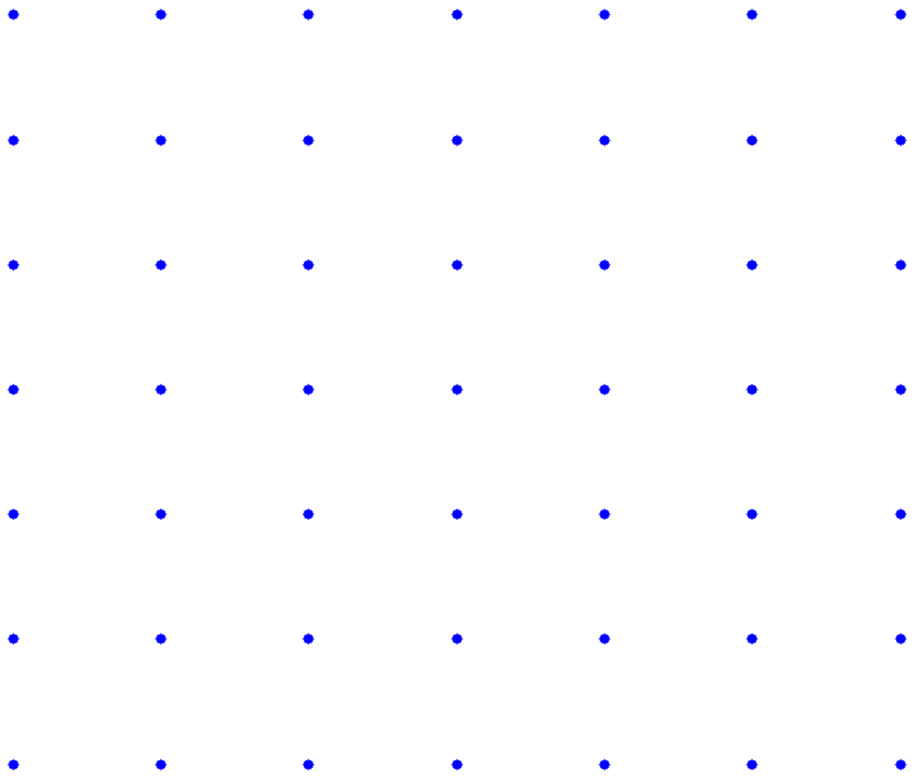

Figure 2-4. An example point set making up a 7x7 grid

The example starts with a point set M composed of 49 points arranged in a 7×7 grid as shown in ***Figure 2-4***. We will subject this point set to a TPS map, but first we must define an initial point set P, and a target point set V, in order to define the mapping function. We will choose P to be a subset of M, however it does not have to be a subset.

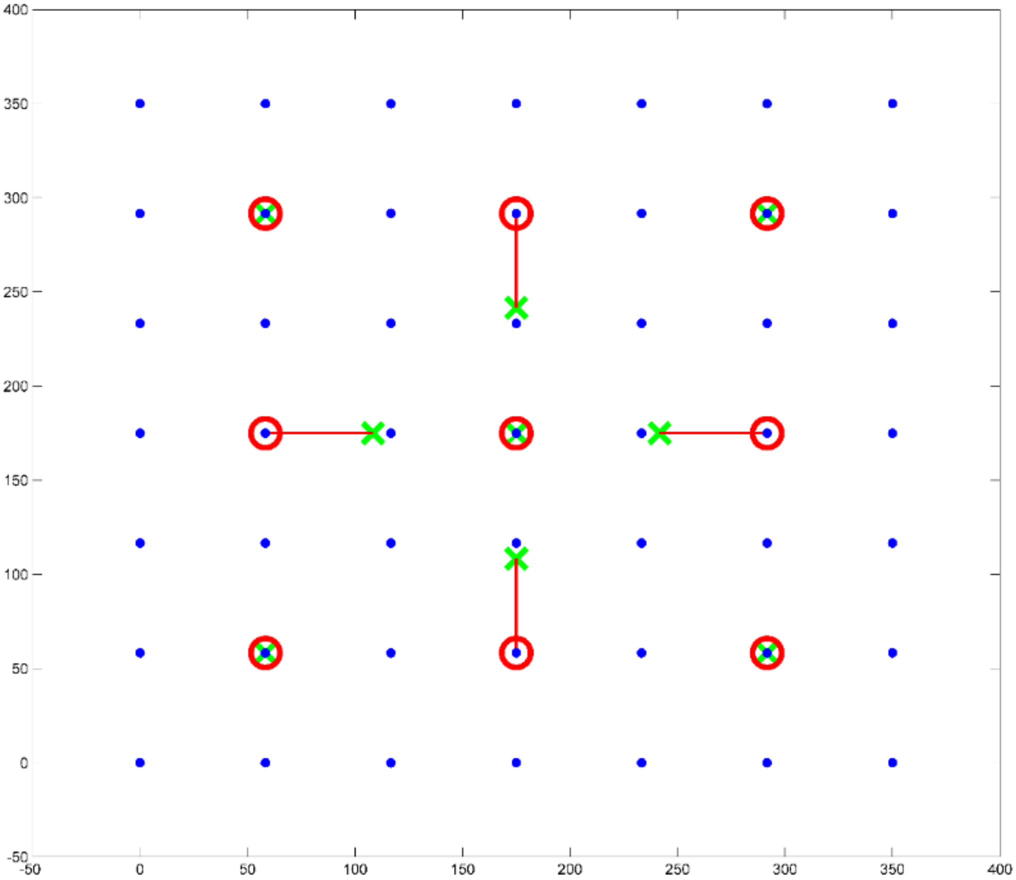

Figure 2-5. Point set *M* shown in blue, initial point set *P* shown as red circles, and target point set *V* shown as green X's with the correspondence shown as red lines.

Figure *2-5* shows the point sets *M, P, and V,* as well as the correspondence between *P* and *V*. Recall that *P* is a subset of *M* and is shown as red circles over the blue dots while *V* is shown as green X's. Note that five of the nine points in *V* are identical to their *P* counterpart. These points map *P* to the same point in space creating an anchor point. These points are not necessary but ensure that the grid *must* deform and not simply change scale to accommodate the map. With P, V and their respective correspondence defined, we can generate the mapping function *f* defined by equations 2.9 to 2.19 and apply it to the entire point set M as depicted in Figure *2-6*.

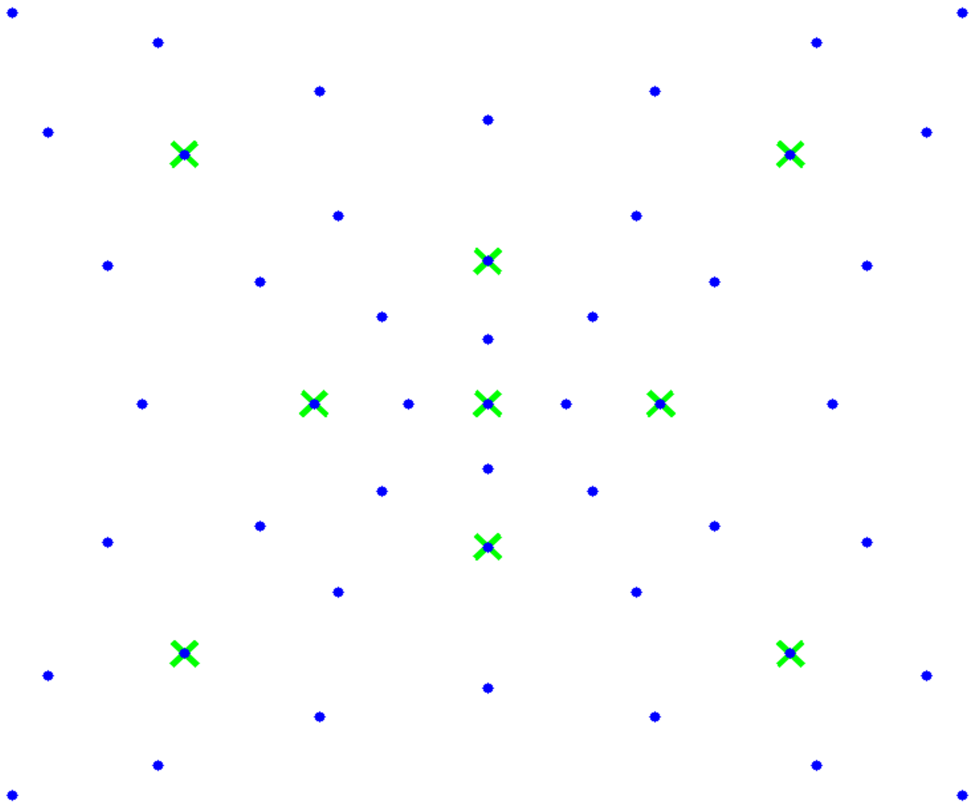

Figure 2-6. Point set *f(M)* shown as blue dots with the target point set *V* shown in green.

However the map function is not limited to the point set M, any set can be used once the function has been created. Figure *2-7* shows a grid being deformed by the mapping function *f*. Initially the grid was uniformly spread across the dimensions of the point set *M* (shown as the green box). Visible are the regions of high density and low density after the deformation.

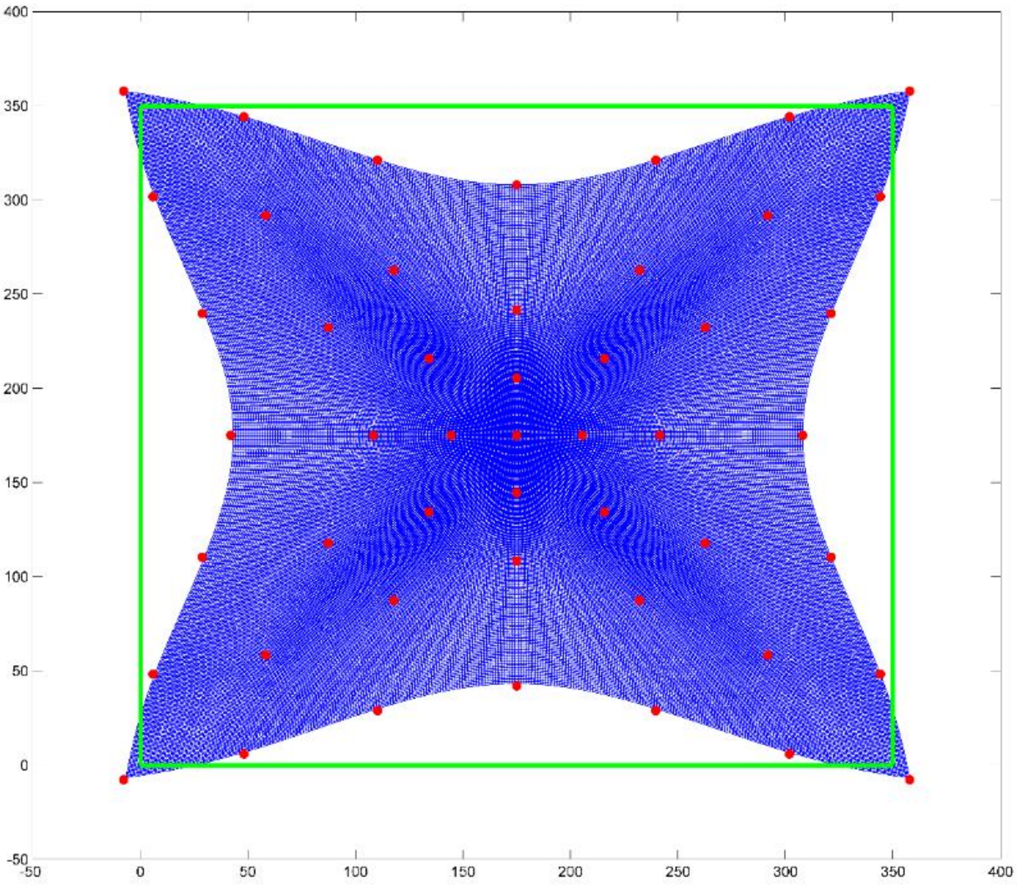

Figure 2-7. TPS warp diagram. Red dots represent target point set *f(M)* with the original grid dimension shown as a green box.

2.3 GMM TPS Algorithm

The main work of this thesis is the creation and testing of an automatic crystal identification algorithm. This section outlines the overall functioning of the algorithm as well as the individual processes and pseudo code needed for application to existing detector flood histograms. As stated before, the algorithm is based on a GMM approach but also utilizes TPS maps. This algorithm was created for, but is not limited to, a new small animal PET insert comprised of 16 detectors having 409 crystals each arranged in a dual layer offset design with the top layer having 21x9 crystals and bottom 22x10 (Stortz et al., 2013). These detector flood images have unique deformations with varying crystal response location densities making a complicated flood histogram to automatically segment. Several methods were initially attempted with varying levels of success before a GMM method was attempted (see section 2.4).

With the first application of a GMM approach it was found that the inherent sensitivity GMM exhibit towards initial starting parameters greatly limited the initial means of the Gaussians. This limitation was so pronounced that the starting means very nearly had to be the actual crystal locations rendering the identification algorithm almost useless. However it was found in the testing of floods there were common regions of stability where the crystal responses were always resolvable and the EM algorithm could easily fit the correct Gaussians. It followed that if the algorithm could utilize the easily obtainable, correct, information in these stable regions of the flood, and use it to influence the initial parameters in the more complicated regions, the algorithm would be much more robust. This was realized through the use of TPS maps, which was not stumbled upon randomly but rather was part of an earlier attempted method. Rather than starting every point at once, the algorithm starts in one location and works outward. Typically this starting point is a known crystal number in a region of stability or little deformation. In practice, the starting point is usually the center crystal of the flood or corner points, as they are the easiest to locate. The TPS map is then used to translate the movement /

convergence of stable points into small deformations that affect and shift the initial parameters of points yet to be fit. In this way the sensitivity of the GMM to starting parameters can be circumvented with the addition of small TPS maps to the algorithm.

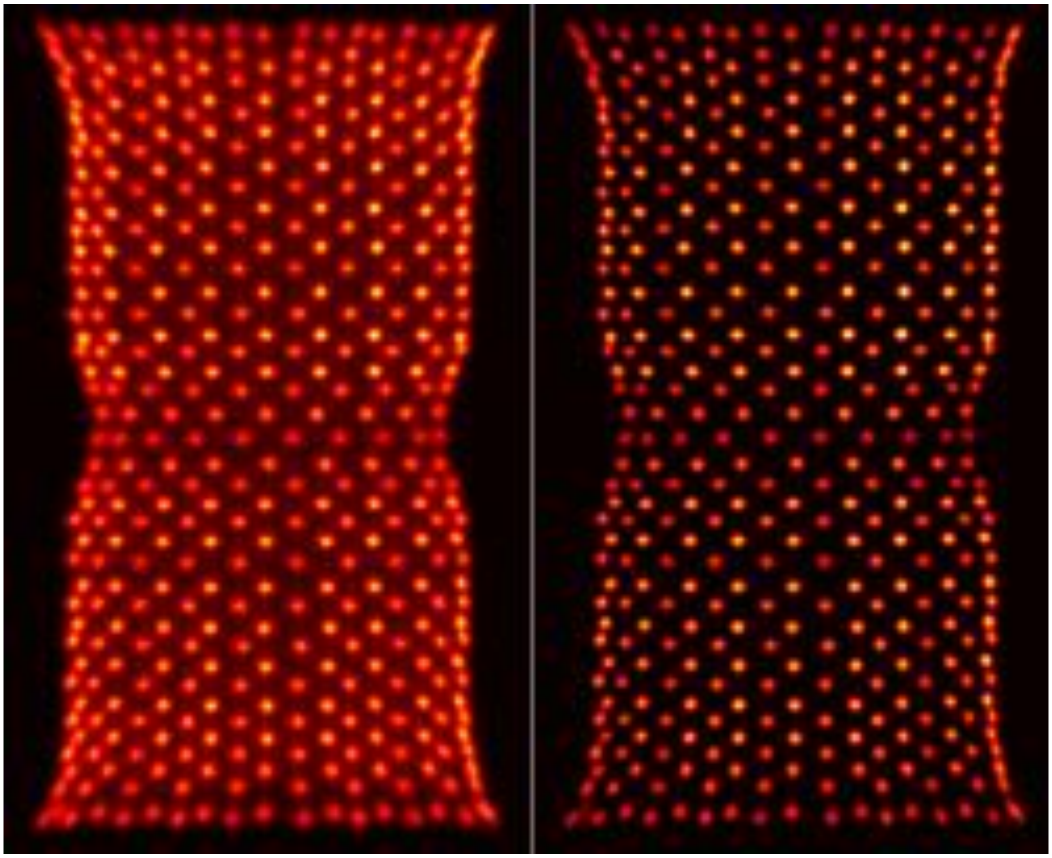

Figure 2-8. Right: Original flood histogram of 409 crystal dual layer offset detector. Left: LoG filtered flood histogram

The input data for this algorithm is assumed to be (x,y) list-mode format of events comprising the point set *C*. This data was planned to be list mode data taken straight from the coincidence circuit but due to the high levels of noise sometimes present in this raw data extra steps can be taken to filter or 'clean up' the data. Pseudo list-mode data, designed to mimic actual list mode data with less noise, can be generated by randomly sampling from a filtered flood histogram using the pixel intensities as sampling weights. The filter used on the flood was a Laplacian of a Gaussian filter (LoG) (Kong, Akakin, & Sarma, 2013) with a standard deviation roughly corresponding to the size of crystal responses in the flood, shown in Figure *2-8*. The LoG filter enhances the appearance of the crystal centers, however if the quality of the flood image is sufficiently good then this step can be omitted and the algorithm can operate directly on the list mode data.

The algorithm starts by creating an initial template (point set V) of user defined dimensions corresponding to a 2D superposition of physical crystal center locations in the scintillator block. The overarching goal of this algorithm is to warp the point set, V, to match the data set C while maintaining the correct crystal numbering inherent to set V. After the creation of point set V, representing the initial estimate of the crystal centers, it is correlated to C by a linear translation, shifting V so the center of mass for both sets is equal, as well as a non-affine transformation which shifts each point in V to its respective Gaussian correspondence, with user defined standard deviation, in C. This step is carried out through one cycle of the EM algorithm (equations *2.3* to *2.7*) initialized with the square template locations as means and large, user defined standard deviations. The means from equation *2.6* are then used as the new template values, shown as blue dots in Figure 2-9. A circular Region of Interest (ROI) is then created at the center of mass (of the data set C) and the point set V_a (a subset of V) is created from any point in V contained within the ROI. This region is not limited to start at the center of mass nor is it constrained to be circular, however the ROI should originate from the region of highest stability or least deformation.

Once initialized, the algorithm follows an iteration cycle. Each point in V_a experiences one iteration of the EM for GMM (equations *2.3* to *2.7*), allowing the point to fit a Gaussian to a subset of the data C (Gauvain & Lee, 1994). That is, the point set V_a is subject to both an E-step and a M-step of the EM algorithm on the data set C. The shift in position for each point in V_a from the mth iteration of the EM step ($V_a^m \rightarrow V_a^{m+1}$) is used to construct a TPS map function f, giving a mapping from one point set to another (equation *2.19*). This is described in equation *2.20* where the function f represents the TPS spatial mapping created with equations *2.9* to *2.19* using V_a^m and V_a^{m+1} as the initial and target point sets respectively. Two stages of the algorithm are shown in Figure 2-9, with the ROI visible and converged points shown in green.

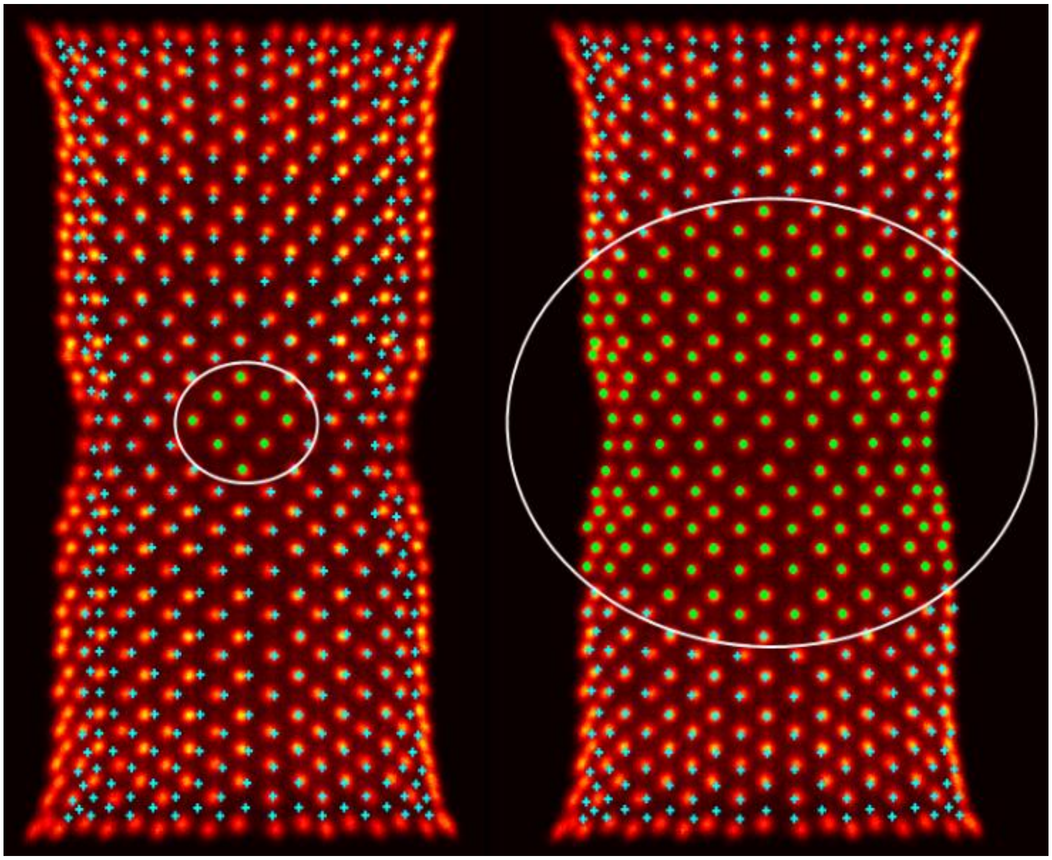

Figure 2-9. Left: Algorithm at 6 iterations. Right: Algorithm at 25 iterations. Converged data points in V_a are shown in green while inactive members of V are blue. The ROI is the white circle. The blue dots outside the ROI represent the crystal location estimates from the initial template warped by the TPS map.

The TPS mapping function *f* is then applied to the whole point set *V* (equation *2.21*). Note that since V_a is a subset of *V*, equation *2.21*, where *f* is utilized, ensures equation *2.20*, where *f* is created. Each iteration cycle is composed of one EM iteration and one TPS transformation. At the end of one iteration loop, the log likelihood L_j^{m+1} of the j^{th} Gaussian for point set V_a is calculated (equation *2.22*) and any point in V_a that has reached convergence, defined as $\left|L_j^{m+1} - L_j^{m}\right| < \varepsilon$, where ε is a preset user defined threshold, is removed from the point set. The ROI is then expanded and another iteration is started.

$$V_a^m \rightarrow V_a^{m+1} = f \tag{2.20}$$

$$V^{m+1} = f(V^m) \tag{2.21}$$

$$L_j^{(m+1)} = \frac{1}{n}\sum_{i=1}^{n} log\left(w_j^{(m+1)} N\left(C_i|\mu_j^{(m+1)}, \Sigma_j^{(m+1)}\right)\right) \tag{2.22}$$

Once all of the points in *V* have reached convergence the algorithm is stopped. **Figure 2-10** shows the algorithm output as well as the segmentation which will lead to a CLUT while **Figure 2-11** shows the crystal numbering. It is extremely important that the crystal location, number, and region boundary all be as accurate as possible for proper event localization, leading to precise image reconstruction. Segmentation of the regions is accomplished by assigning all the pixels in the image to the Gaussian with the highest correspondence respectively. The algorithm is summarized in pseudo code below.

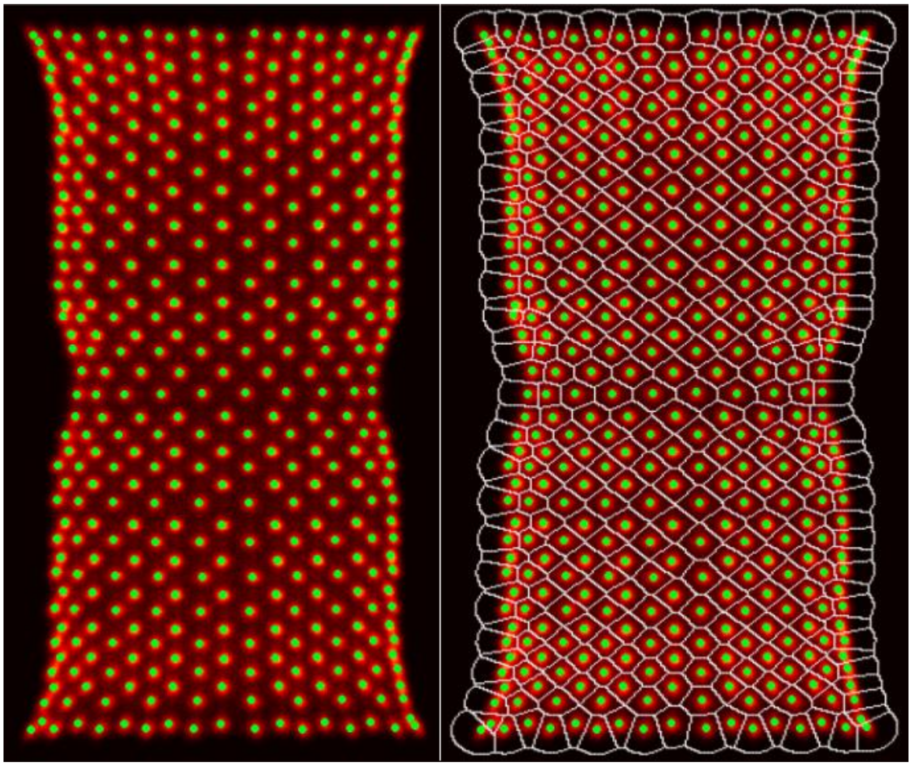

Figure 2-10. Left: finished algorithm with crystal centers shown in green. Right: Simple segmentation of flood showing the CLUT in white.

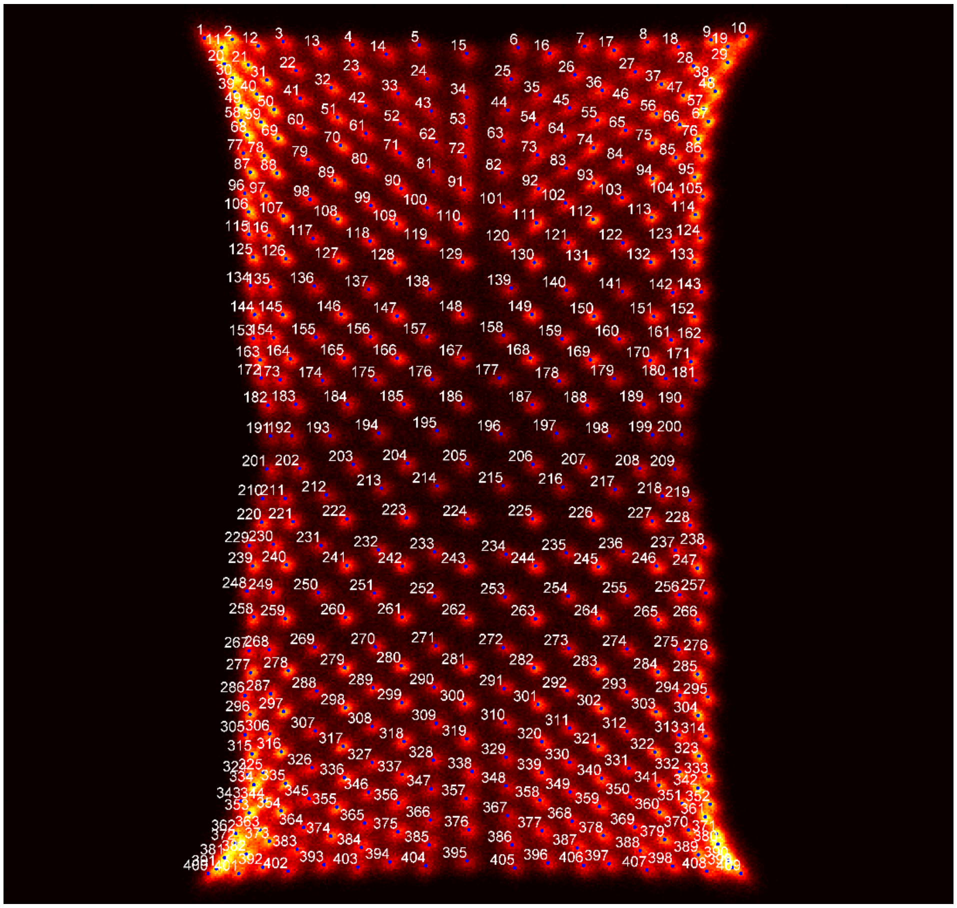

Figure 2-11. Numbering of the flood histogram. Each crystal must have the proper number along with the proper segmentation for accurate image reconstruction.

2.3.1 Pseudo Code for TPS GMM Algorithm

```
1. Initialize
    a. Create Template $V$
    b. Correlate $V$ to data $C$
    c. Initialize ROI

2. Begin Loop
    a. Activate subset of V within ROI  $\rightarrow V_a = ROI(V)$

3. Estimation Maximization
    a. E-step on $V_a$ (equations 2.3 & 2.4)
    b. M-step on $V_a$ (equations 2.5 to 2.7)

4. TPS mapping
    a. Create TPS map $f$ and apply to $V$
          (equations 2.9 to 2.19)

5. Convergence Check
    a. Compute Log-likelihood of $Va$ (equation 2.22)
    b. Remove Converged points from $Va$

6. Iteration End Check
   All points in $V$ converged?

    Yes.  End

     No.  Expand ROI and Return to step 2
```

2.4 Previous Unsuccessful Methods

While developing the current algorithm based on GMMs and TPS maps several other methods were attempted and/or tested with varying results and were eventually discarded. The different approaches are described below along with each method's pros and cons, along with the reason for their abandonment:

- **Sum Superposition Method** – This method relied on summing the flood histogram in the Y-dimension and the X-dimension creating two superposition plots of the vertical and horizontal profiles of the flood. The peaks in the vertical profile were used to locate the rows of the flood. Using a width determined by the vertical peak separation, the horizontal profile of each row was summed and the peaks of each profile determined the X location of the crystal centers. These X positions along with the respective Y positions made up the full set of crystal centers.

    - **Pros** – This method was very fast and simple to implement. It works best with very symmetric flood histograms and may be even more accurate than the current algorithm with flood histograms such as the Inveon floods (discussed in section 3.2).
    - **Cons** – As one may be able to predict, this method is very sensitive to changes to the grid structure of the flood. Meaning; floods that have very straight rows do well with this method, however this is rare in floods with common distortions. It was found this method worked moderately with NIM acquired floods (section 3.1.1) but failed every test with openPET acquired floods (section 3.1.2) and for this reason was no pursued as a viable method.

- **Spring Model Method** – This method used a physical model of forces to try and find the correct crystal center location. The flood was smoothed and differentiated into X and Y gradients. A template was created corresponding to the physical dimensions of the crystal array. The template also served as nodes in a spring mesh that was created where adjacent crystal centers in the template were connected by a spring. The nodes of the template then experienced two forces: a spring force and a force corresponding the intensity gradients of the flood histogram. The theory being that the gradient forces would pull the respective nodes towards their crystal centers and letting the two forces come to an equilibrium (with a damping force on velocity), the spring mesh would ensure that the template fit with the lowest potential energy, thought to correspond to the best fit.

    - **Pros** – None were found. This method was tested and abandoned very quickly.
    - **Cons** – Initially each spring connecting a node was assigned the same spring constant but it was soon found that large deformations in the flood required some springs to have different spring constants, making the numbers of adjustable parameters very high and complicated. Secondly the spring mesh needed to be heavily damped otherwise velocity of the nodes would cause wild errors. Even with sufficient damping however, certain errors in nodes could cause a propagation of errors across the entire mesh. This method was eventually deemed too complicated, having adjustable input parameters almost equal to crystals in number.

- **Annealing Method** – This method was based of the work of a group from the university of Florida (Chui & Rangarajan, 2003). The group outlines a point set matching algorithm based on TPS maps. In the algorithm one 2D point set is matched to another 2D point set taking into account possible outliers from each set. The point sets are registered to one another using fuzzy correspondence and simulated annealing. In this case the simulated annealing refers to the initial correspondence of each point being large, meaning each point corresponds to many other points in the opposite point set, then slowly lowering the correspondence. The theory being that as correspondence is lowered, the TPS map continuously warps one of the point sets until you have one to one correspondence between all points not deemed outliers.

This method was applied to our floods by first scanning the flood histogram to find possible crystal centers. This became the first point set, however it was possible that this point set contained too few or too many points. Since the order of this point set was unknown, it was registered, via the aforementioned method, to another point set that corresponded to the physical dimensions of the crystal array. Once registered, the found crystal centers corresponded to the proper crystal number and possible outliers were removed.

- **Pros –** The method described by (Chui & Rangarajan, 2003) is a very robust point matching algorithm, capable of finding correspondence in very noisy data which was well suited to the flood histograms used for testing. This method worked quite well if the proper number of points were initially found. Although this was not the method chosen, it served as an introduction to TPS serving as an essential stepping stone to the current algorithm.
- **Cons –** This method relied heavily on the initial scan for possible crystal centers. If this scan did not find all of the crystal centers then it was impossible for this method to give correct results. It was found that on lower quality floods it was very difficult to locate all the centers leading to incorrect results most of the time.

3 Methods and Results

All results were obtained on a computer with the following hardware / software:

Operating System	64-bit Windows 7 Pro
Processor	Intel i7-3770 @3.40Ghz
RAM	16.0 GB DDR3
Mother Board	Intel Xeon E3-1200
Video Card	NVidia GeForce GTX 670
MATLAB	R2013b

The algorithm was tested on four different types of flood histograms (93 floods in total) using a variety of different parameter combinations. The adjustable parameters in the algorithm include the ROI step size, or ROI growth rate, the starting ROI position(s), and the GMM log-likelihood threshold (recall $\left|L_j^{m+1} - L_j^m\right| < \varepsilon$). On top of these adjustable parameters within the algorithm itself, there are input parameters that may be subject to change as well depending on what is available to the user, these include the starting template and the number of overall counts (events) making up the flood. The outcome of the algorithm tests are assessed in both run time and accuracy of the subsequent crystal center locations. The crystal center locations are assessed by eye and the number that need manual correction determine the accuracy of the respective trial. The parameters are described in greater detail along with the expected influence on the algorithm outcome below:

- ROI Step Size – Representing the growth of the ROI between iterations, this parameter is directly proportional to how many points are activated each iteration, affecting the run time of the algorithm but inversely affecting the accuracy. The theory behind this algorithm desires points to be warped by the TPS map by previously activated and converged points. Thus activating too many points at once can cause under warped starting positions and lead to inaccurate results.

- ROI Starting Position(s) – The ROI can be started anywhere and in multiple locations simultaneously on the flood histogram. The first activated point, however, should converge to the correct crystal response otherwise there can be a cascade of incorrect convergences with the possibility of complete TPS map failure. Different styles of flood deformations usually lend themselves better to starting locations in the corners or the centers of the flood.

- Log-Likelihood Threshold – This parameter mainly affects the number of iterations each Gaussian requires to reach convergence, and as a result affects the overall run time of the algorithm. A lower value allows fast convergence but may yield a crystal center or Gaussian that does not accurately represent the crystal response.

- Template – While this algorithm aims to reduce the intrinsic GMM need for accurate starting conditions, it still requires a starting point set (template) that resembles the flood or physical crystal array.

- Total Samples – In testing, this parameter represents the total samples from the flood histogram while in practice it could be the number of events in the list-mode data. Increasing the number of samples points from the flood histogram yields a more accurate Gaussian fit while also increasing run time of the algorithm. However, when increasing the samples, there are diminishing returns, past a certain point, between accuracy and the number of samples.

Four different sets of flood histograms were used to evaluate the accuracy and speed of the algorithm. Two of the sets came from our group's MR compatible PET insert. These sets were comprised of 16 flood histograms from each of the 16 detectors within the PET insert, as stated before these detectors have a dual layer offset design with 22x10 and 21x9 bottom and top layers respectively, 409 crystals in total. These sets differ in the acquisition hardware used, with one set using Nuclear Instrumentation Modules (NIM) and the other OpenPET electronics. OpenPET is a flexible / customizable general purpose readout system for PET scanner, typically in development. The third set of flood histograms is from a Siemens Inveon PET scanner. This set is composed of 60 floods from the 20x20 single layer LSO Inveon detectors (Bao, Newport, Chen, Stout, & Chatziioannou, 2009; Constantinescu & Mukherjee, 2009). Finally a single 8x8 PSAPD flood exhibiting a classical pin cushion distortion was used as a proof of concept for further applications of the algorithm. The results of the algorithm tests are in the following sections.

3.1 MR Compatible Small Animal PET Insert Scanner

As stated before, this algorithm was created with the aim to become calibration software for an MR compatible small animal PET insert scanner developed by our group (Stortz et al., 2013). The PET insert was designed for simultaneous imaging inside a Bruker 7T MR scanner. Figure *3-1* shows the finished, working prototype of the PET insert.

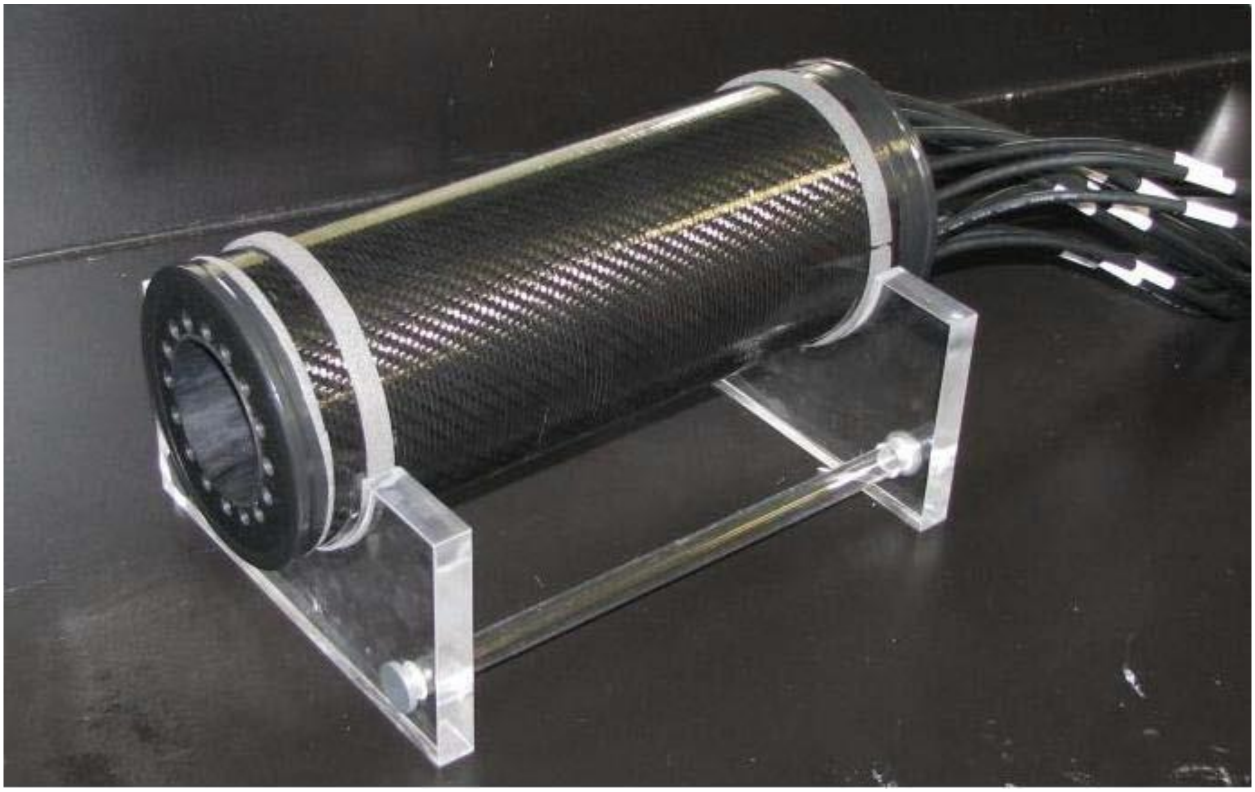

Figure 3-1. Prototype MR Compatible Small Animal PET insert developed by this group.

The system is made of one ring composed of 16 detector modules, as shown in ***Figure 3-2***. Each detector module has a scintillator crystal array made of 409 Cerium-doped Lutetium Yttrium Oxy-Orthosilicate (LYSO) crystals. The LYSO crystals are arranged in a dual layer offset design where the top layer is shifted by a half crystal compared to the bottom layer, resulting in DOI information from the location of the crystal response on the flood histogram as shown in ***Figure 3-3***. The crystal array is of dimension 21×9 and 22×10 for top and bottom layers respectively, and have dimensions of 1.2×1.2×4 (top) / 6 (bottom) mm^3. The scintillator arrays are coupled to two SensL 16-pixel ArraySB-

4 SiPM arrays each having 16 outputs making 32 in total which are multiplexed down to 4 output signals via a resistive network.

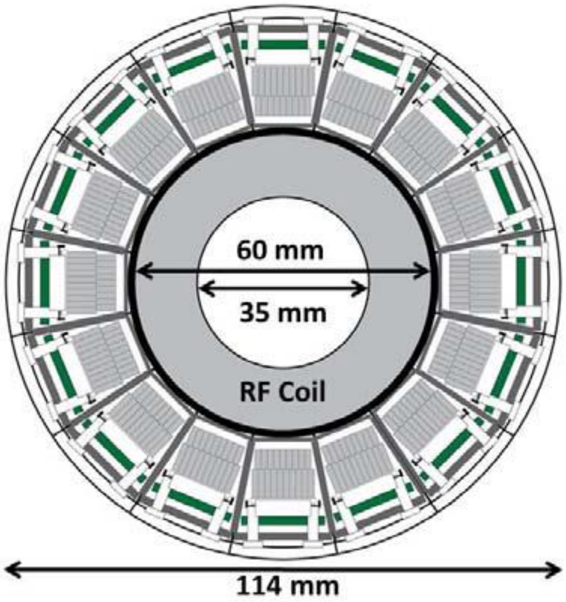

Figure 3-2. Cross section of PET insert prototype showing inner and outer diameters as well as the RF coil for MR imaging. Also visible are the 16 detector modules

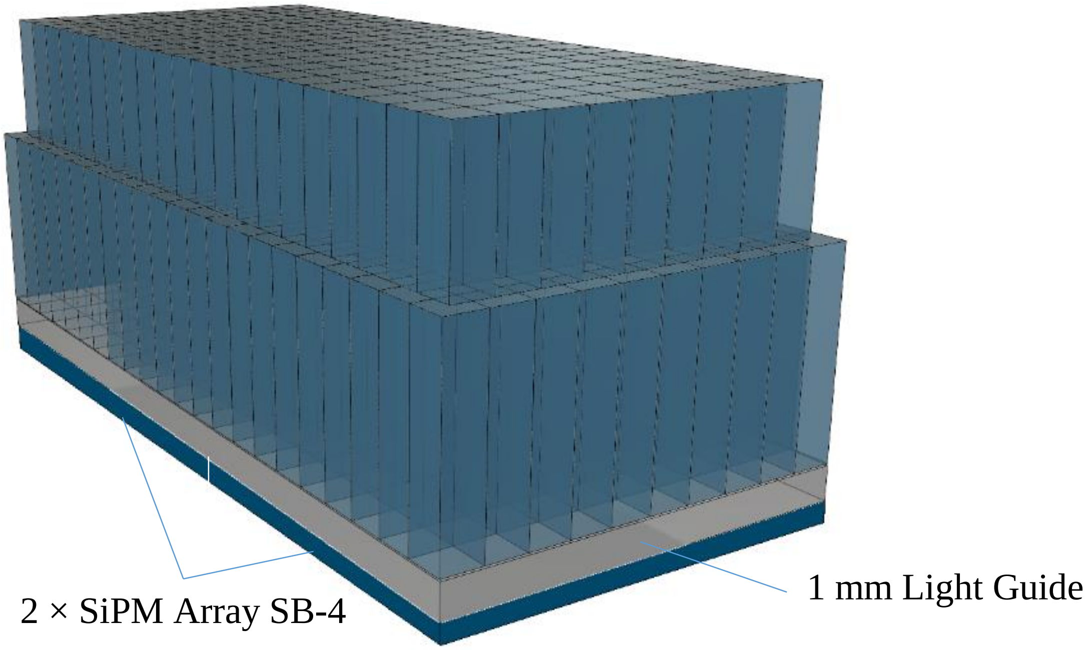

Figure 3-3. Rendered sschematic of the dual layer offset crystal array design

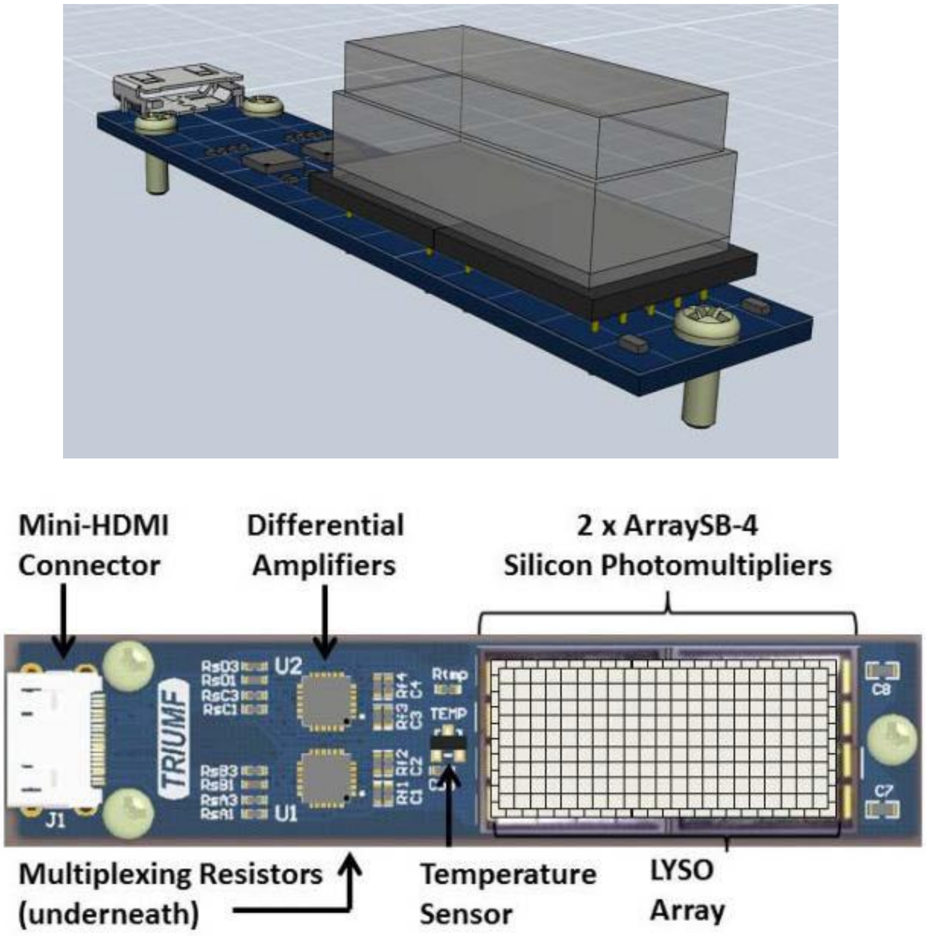

Figure 3-4. Top: One detector module composed of the transmitter board, the SiPMs and the dual layer LYSO crystal array. Bottom: top down view of detector module with schematic labels.

Each detector module is composed of the scintillator array, two SiPMs and a transmitter board which houses all the components, see Figure *3-4*. Each SiPM has 16 pixels and subsequently 16 signal outputs making 32 outputs from both SiPMs on the transmitter board. Due to space and complexity limitations, these 32 signals are multiplexed down to only 4 output signals with a resistive network. The 4 signals (A, B, C, D) are the relative strengths of summed signals in the corners of the resistive array, as shown in Figure *3-5*. These signals can be used in Anger-type logic to position the gamma photon within the scintillator array, assigning i, j coordinates with equation *1.2*.

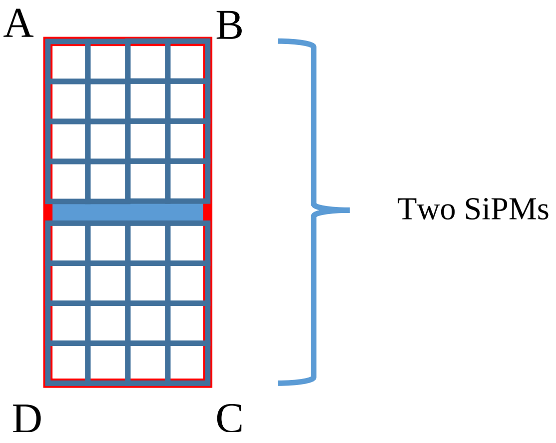

Figure 3-5. Signal diagram of the two SiPMs on the transmitter board. Shown are the four multiplexed signals from the 32 pixels (A, B, C, D) and the corners they represent on the photodetector rectangle.

Each transmitter board is powered and readout by an HDMI cable. The four multiplexed signals are transmitted out through these HDMI cables to the data acquisition electronics to become part of the list-mode data. The list-mode data is comprised of the four signals along with a time stamp, the energy of the gamma is inferred from the sum of the four signals.

3.1.1 NIM Acquisition Floods

3.1.1.1 Setup

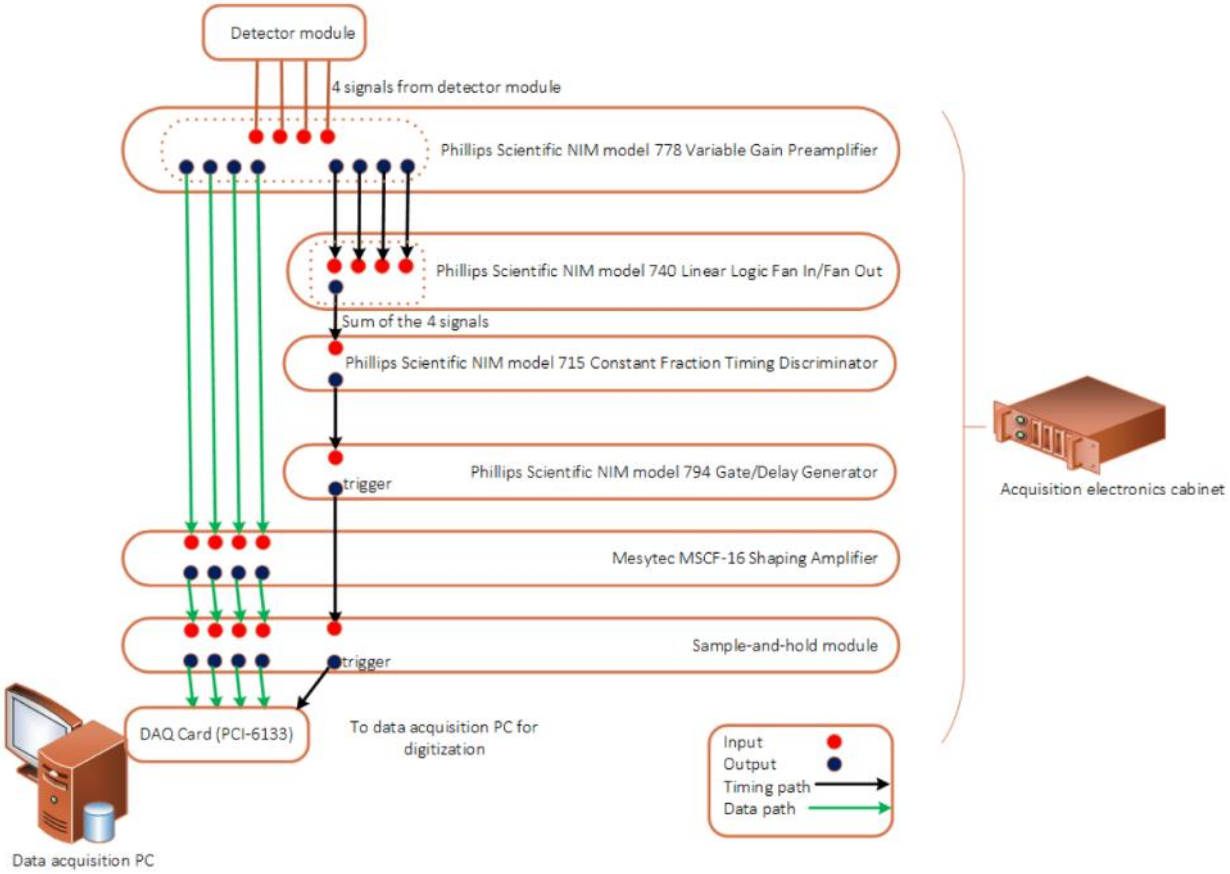

Figure 3-6. Signal path from each detector module to data acquisition computer, resulting in list-mode data (Shams, 2014).

While individual detector modules were being tested, before the PET insert prototype was formally constructed, data acquisition was handled through Nuclear Instrumentation Modules (NIM). The four event signals (A, B, C, D) travel from the transmitter boards through the HDMI cables to a Detector Interface Board (DIB) which can accept signals from 4 transmitter boards. The four event signals are then connected to a Phillips Scientific NIM model 778 variable gain preamplifier which amplifies each signal but also splits the signal into two identical copies, one used to generate an event trigger and the other for measuring amplitude. The trigger paths from the NIM 778 are connected to a Phillips

Scientific NIM model 740 linear logic fan in/out, the sum of which is connected to one channel in a Phillips Scientific NIM model 715 Constant Fraction Discriminator (CFD) which generates a threshold for the trigger signal. The trigger is generated by using the output of the CFD as the input to a Phillips Scientific NIM Model 794 Gate/Delay generator. This trigger-gate is used to drive a sample and hold module which acquires the other four event signal clones from the NIM 778 after they are passed through a shaping amplifier (Mesytec MSCF-16). The custom eight-channel sample and hold is connected to a National Instruments PCI-6143 data acquisition card mounted in a PC running Microsoft Windows with acquisition software developed in Labwindows/CVI® (National Instruments). Figure *3-6* shows a block diagram of the signal path described above. The list-mode data is converted into i, j points via equation *1.2* and these points are binned into a matrix with dimension of the users choosing creating a flood histogram. Figure *3-7* shows a flood histogram created with NIM acquired data binned into 512x512 matrix using ~2M events.

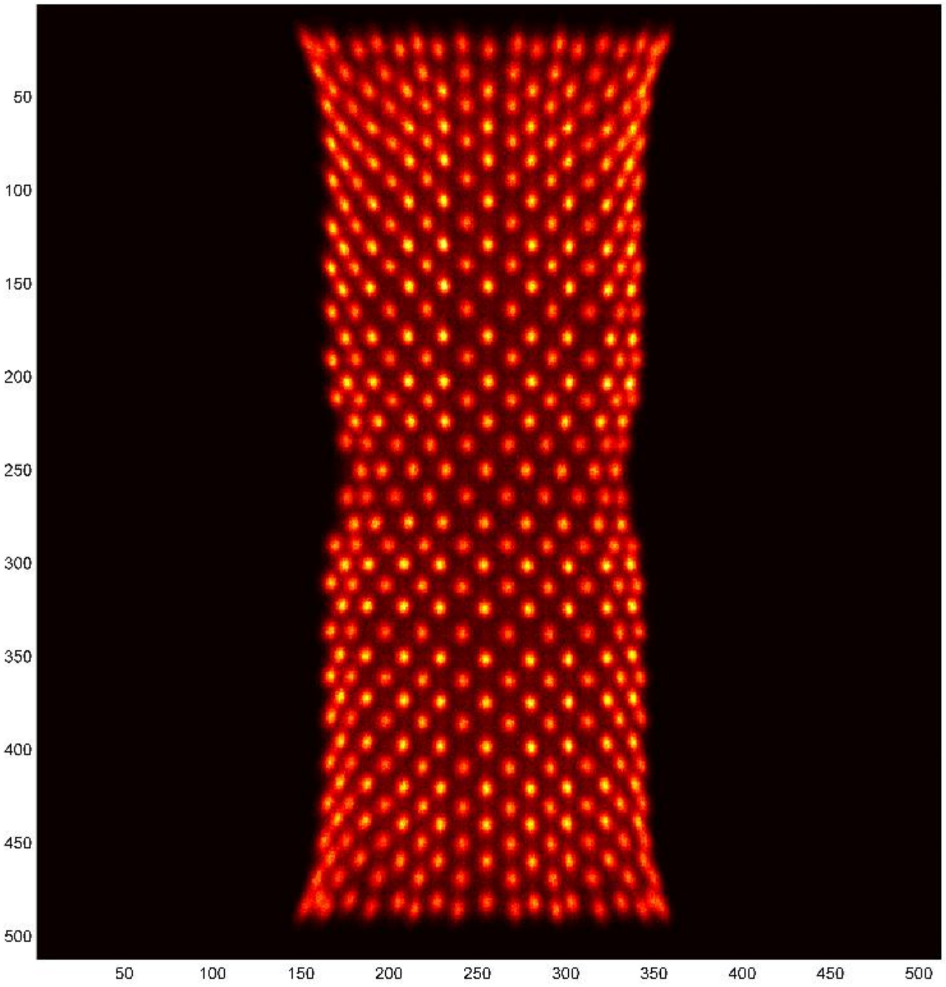

Figure 3-7. 512x512 bin Flood Histogram from one detector module acquired through NIM electronics.

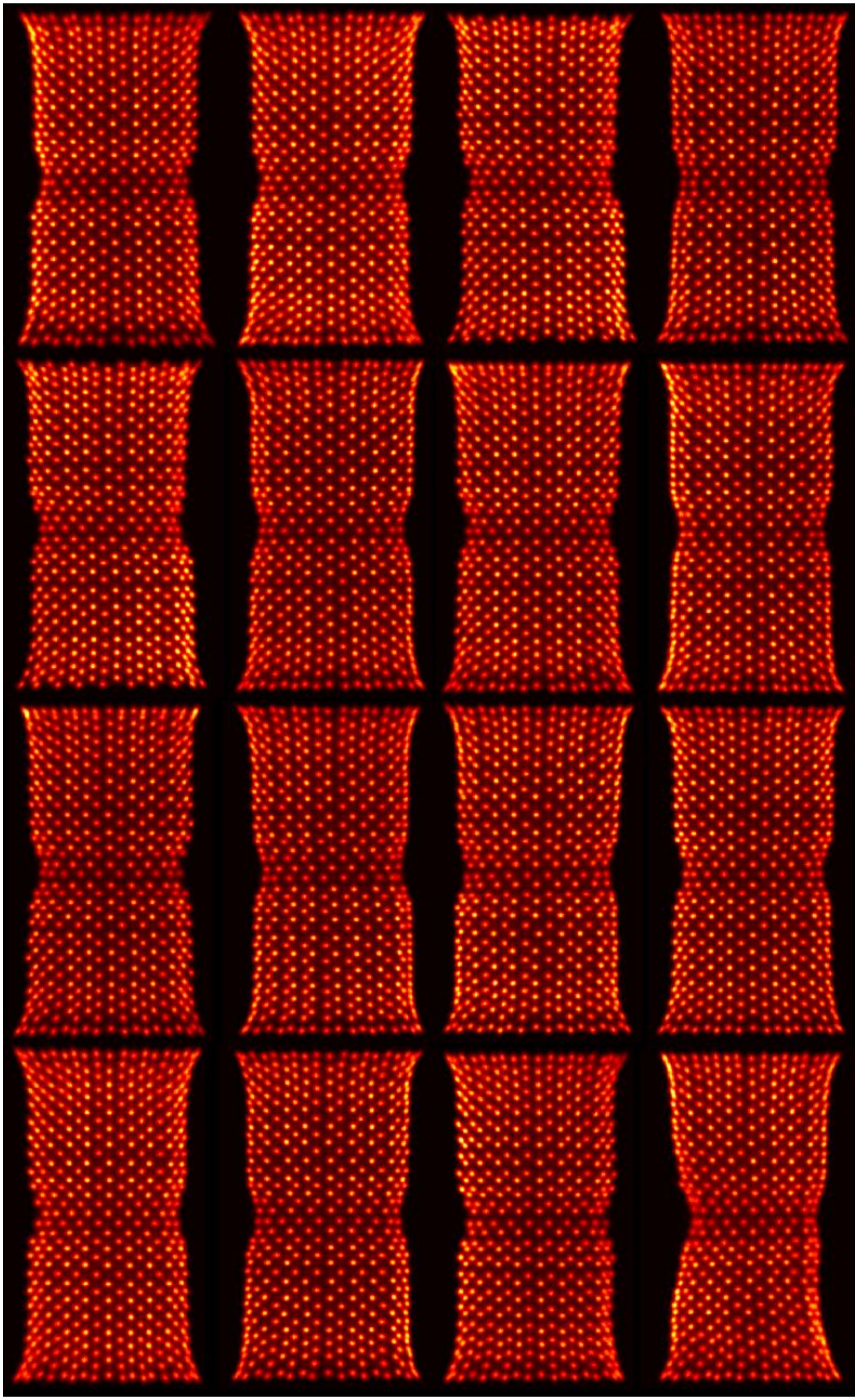

Figure 3-8. All 16 NIM acquired PET insert detector flood histograms

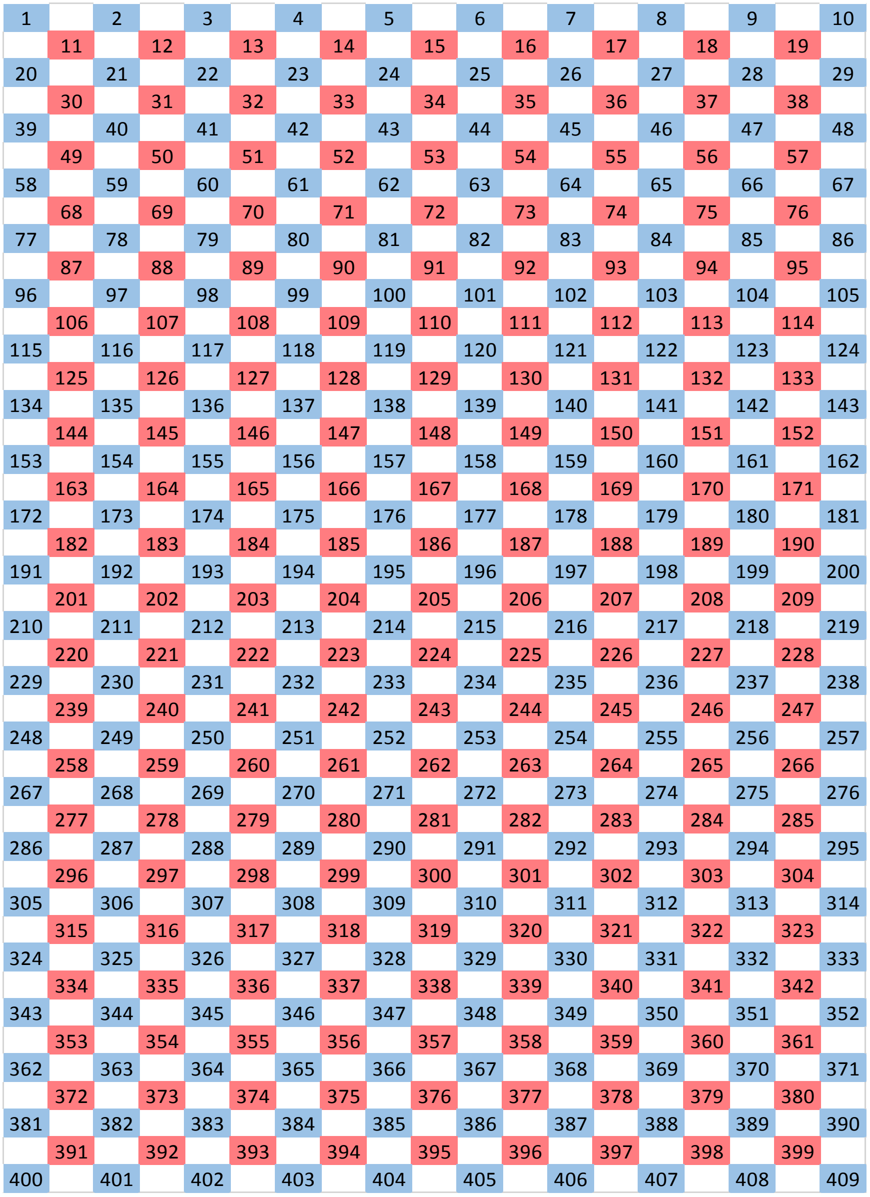

1		2		3		4		5		6		7		8		9		10
	11		12		13		14		15		16		17		18		19	
20		21		22		23		24		25		26		27		28		29
	30		31		32		33		34		35		36		37		38	
39		40		41		42		43		44		45		46		47		48
	49		50		51		52		53		54		55		56		57	
58		59		60		61		62		63		64		65		66		67
	68		69		70		71		72		73		74		75		76	
77		78		79		80		81		82		83		84		85		86
	87		88		89		90		91		92		93		94		95	
96		97		98		99		100		101		102		103		104		105
	106		107		108		109		110		111		112		113		114	
115		116		117		118		119		120		121		122		123		124
	125		126		127		128		129		130		131		132		133	
134		135		136		137		138		139		140		141		142		143
	144		145		146		147		148		149		150		151		152	
153		154		155		156		157		158		159		160		161		162
	163		164		165		166		167		168		169		170		171	
172		173		174		175		176		177		178		179		180		181
	182		183		184		185		186		187		188		189		190	
191		192		193		194		195		196		197		198		199		200
	201		202		203		204		205		206		207		208		209	
210		211		212		213		214		215		216		217		218		219
	220		221		222		223		224		225		226		227		228	
229		230		231		232		233		234		235		236		237		238
	239		240		241		242		243		244		245		246		247	
248		249		250		251		252		253		254		255		256		257
	258		259		260		261		262		263		264		265		266	
267		268		269		270		271		272		273		274		275		276
	277		278		279		280		281		282		283		284		285	
286		287		288		289		290		291		292		293		294		295
	296		297		298		299		300		301		302		303		304	
305		306		307		308		309		310		311		312		313		314
	315		316		317		318		319		320		321		322		323	
324		325		326		327		328		329		330		331		332		333
	334		335		336		337		338		339		340		341		342	
343		344		345		346		347		348		349		350		351		352
	353		354		355		356		357		358		359		360		361	
362		363		364		365		366		367		368		369		370		371
	372		373		374		375		376		377		378		379		380	
381		382		383		384		385		386		387		388		389		390
	391		392		393		394		395		396		397		398		399	
400		401		402		403		404		405		406		407		408		409

Figure 3-9. The proper numbering for one detector of the MR compatible small animal PET insert. Blue tiles represent bottom layer crystals while red are top layer.

Figure *3-7* is a typical flood from our group's dual layer offset crystal array, showing the interleaved crystal response resulting from the offset top layer. The crystal responses are numbered starting from the top left corner and continue left to right. The layers are not counted one at a time but rather simultaneously as depicted in Figure *3-9* showing the interleaved design, with the red cells being the top layer and the blue cells being the bottom layer crystals. By having the top and bottom layer distinguishable on the flood histogram as separate crystal responses one is able to acquire DOI information from this design. Figure *3-7* also showcases some of the distortions that must be dealt with when numbering the flood histogram and creating the CLUT. As stated before, the flood histogram is not a uniform rectangle like its physical counterpart (the crystal array) but is subject to various effects that distort its dimensions. Some distorting factors include the internal SiPM capacitance, the multiplexing network of resistors, and the optical photon paths within the scintillator array. The flood from the PET detectors acquired through NIM electronics show a small pin cushion distortion visible as pulling outwards in the corners of the flood as well as a compression in the mid-section. The flood also exhibits a small compression of the edge crystals all around the borders of the flood. The extended corners and compression of the edge crystals can be attributed to multiple causes. Each crystal in the array is covered (on 4 sides) in a reflective material called Enhanced Specular Reflector (ESR) which reflects 97% of visible photons. This is designed to pipe scintillation light and hold it in its respective crystal. However between the SiPM and the crystal array is a 1 mm thick glass light guide which is not segmented. The light guide has ESR on the 4 sides. This means that a large portion of the isotropic spread of scintillation photons within an edge crystal will be reflected by the ESR on the light guide resulting in a ‘center of mass’ that trends towards the center of the array rather than the true center of the crystal which absorbed the photon, Figure *3-11* depicts this one cause of edge crystal distortion. A second cause is from Compton scattering within the crystal array itself. Compton scattering usually causes the incoming gamma to deposit its energy over multiple crystals rather than the single crystal of interaction. This results in a spread of visible scintillation photons that lead to an incorrect position for the gamma ray. Compton scattering is the main source of inter-crystal scatter which adds noise to the flood histogram by populating regions between crystal responses. Compton scatting events in edge crystals will likely only be detected if they scatter towards the center of the crystal array. If the Compton scattered photon is redirected outwards it will leave the array depositing very little, if any, energy in the scintillation crystal. This effect can manifest itself in ‘tails’ on crystal responses, where the inter-crystal noise has a distinct direction towards the center of the crystal array.

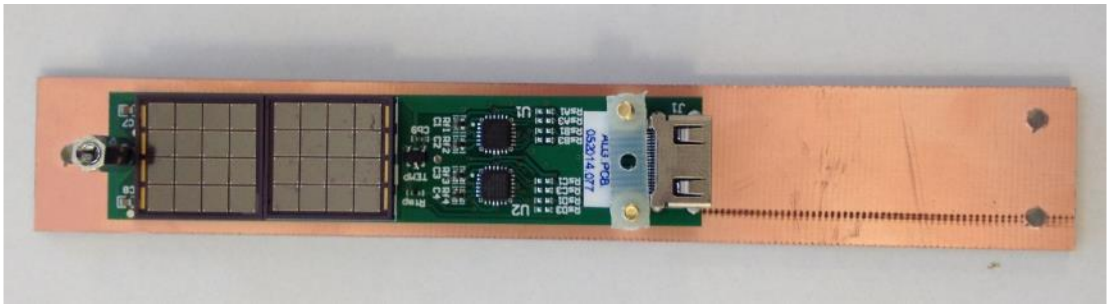

Figure 3-10. Transmitter board without crystal array. Visible are the two SiPMs and their pixels.

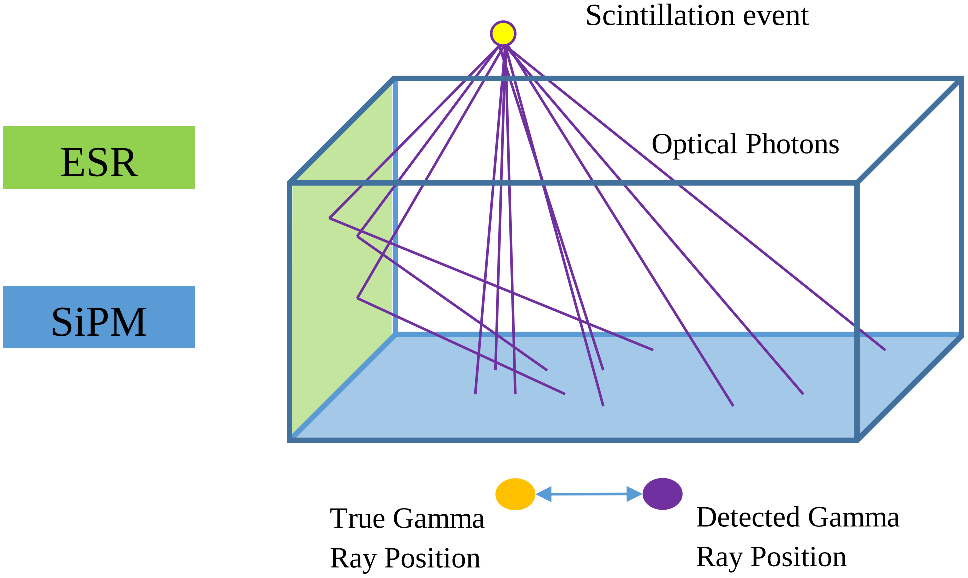

Figure 3-11. Depiction of light guide under an edge crystal, with ESR reflecting optical light causing the detected position of the gamma ray to be shifted away from the reflective material.

The last distortion of interest for the NIM acquired flood histograms is the slight compression of the flood in the center region. This particular crystal array is too long for just one SiPM, so it must be coupled to two SiPMs side by side. However, the SiPMs have mechanical support packaging around their perimeter such that when placed side by side there is an effective dead space between them, see Figure *3-10*. Since the crystal array is continuous and has actively scintillating elements overtop of this dead space, a reflective strip of ESR was placed over top of this dead region in an attempt to collect at least a portion of the optical photons that would have otherwise been lost. This results in a slightly larger compression distortion in the region with the ESR strip.

3.1.1.2 Algorithm Results

Testing with the sixteen NIM floods was initialized using a simple rectangular dual layer offset template that mimics the crystal array dimensions and roughly matches the flood size. This template can be viewed in Figure *3-12* as the blue dots as well the initial starting location of the ROI shown as the green ring. The starting location used was an average position of manual selected centers. The center crystal response was manually selected for each flood and the average position was used to initialize all algorithm trials with the NIM floods.

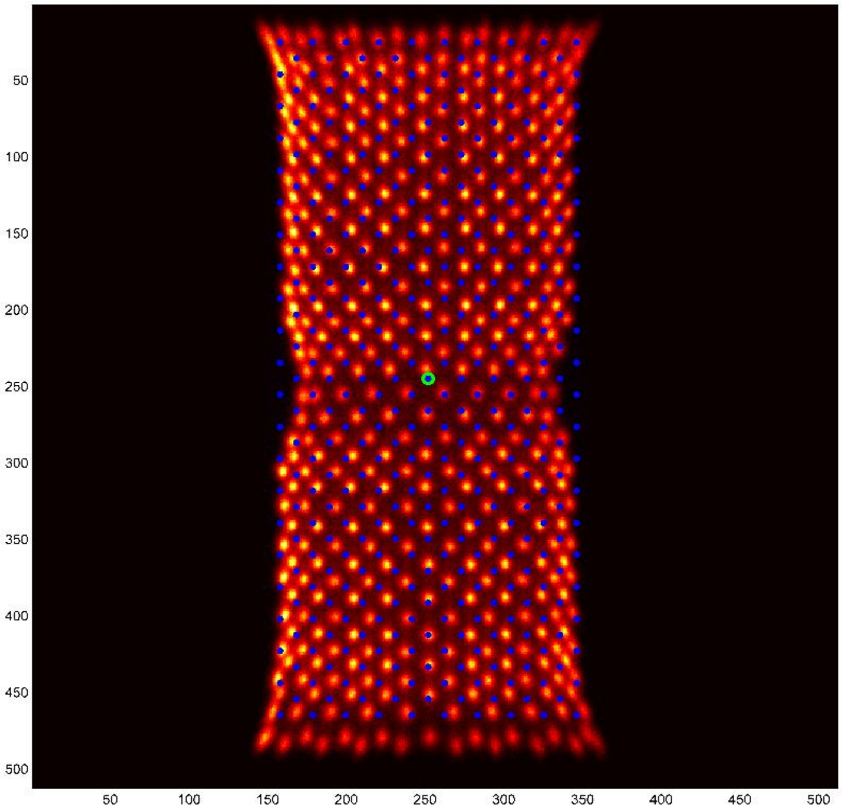

Figure 3-12. NIM acquired flood histogram showing the initial template point set (blue dots) and the starting ROI position (green)

Nine algorithm trials were carried out with the 16 NIM floods running through all combinations varying the Log-likelihood threshold between 0.05, 0.5, and 5 as well as the total counts between 100k, 50k, and 25k. The results are displayed in Table *1* with 'step' and 'threshold' being the ROI step size and log-likelihood threshold, respectively. The fourth column in the table, 'Need Correcting', specifies the total number of crystals out of the 16 floods (6,544 crystals total) that would require manual correction in a calibration setting. The average time represents the mean time to complete the segmentation of one flood histogram while the total time is the full algorithm time across all 16 floods. The error in the average time is the standard deviation of the 16 individual flood times. The subsections of the correction column 'corner' and 'center' represent the number of crystals that needed correcting in the corner of the flood vs. all other locations respectively. A corner region is represented by the five crystal centers residing there, for example in Figure *3-9* the top left corner is represented by crystals 1, 2, 11, 20, and 21. Any error in these regions is labelled a corner error. It was deemed necessary to separate the corner regions from the rest of the flood since the most information is lost here and subsequently it is the most error prone. An error in the corner regions is not as significant as a center error.

Table 1. Results from algorithm tests on NIM acquired floods

Step	Threshold	Samples (×10³)	Need Correcting		Accuracy (%)	Avg. Time (s)	Total Time (s)
			Corner	Center			
5	0.05	100	9	0	99.86	82.5 ± 6.9	1320.3
5	0.5		7	0	99.89	78.2 ± 7.2	1250.6
5	5		8	0	99.88	62.9 ± 1.6	1006.8
5	0.05	50	12	0	99.82	38.4 ± 2.4	613.7
5	0.5		10	0	99.85	33.2 ± 1.3	531.4
5	5		10	0	99.85	30.2 ± 0.6	483.1
5	0.05	25	12	0	99.82	21.2 ± 1.5	338.5
5	0.5		10	0	99.85	19.3 ± 0.7	309.1
5	5		10	2	99.82	17.5 ± 0.4	280.4

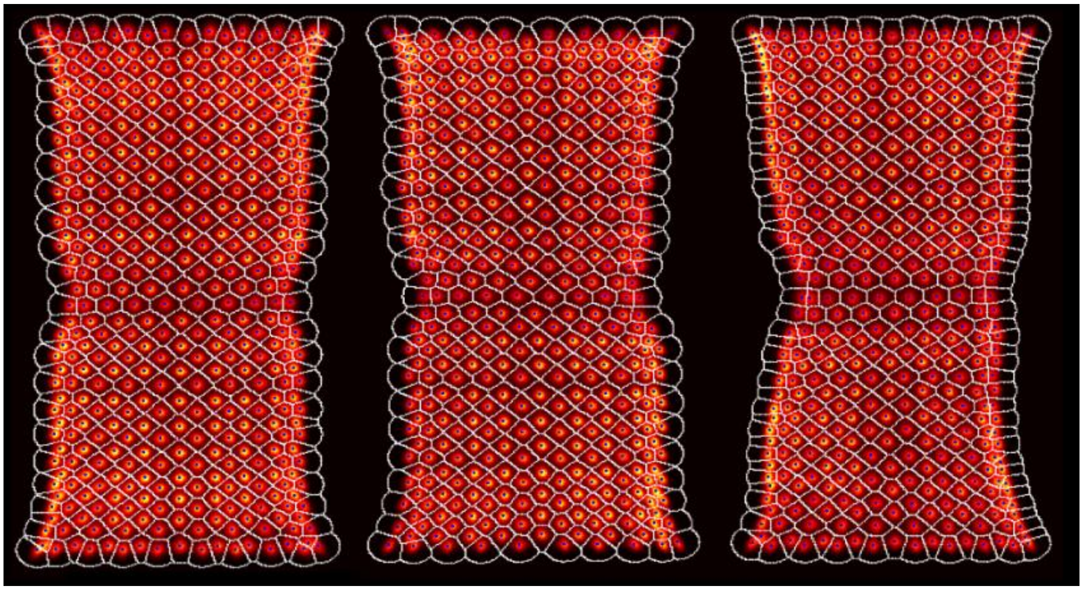

Figure 3-13. Three examples of fits to NIM floods with 100k counts and a 0.5 threshold. Visible are the CLUT boundaries in white.

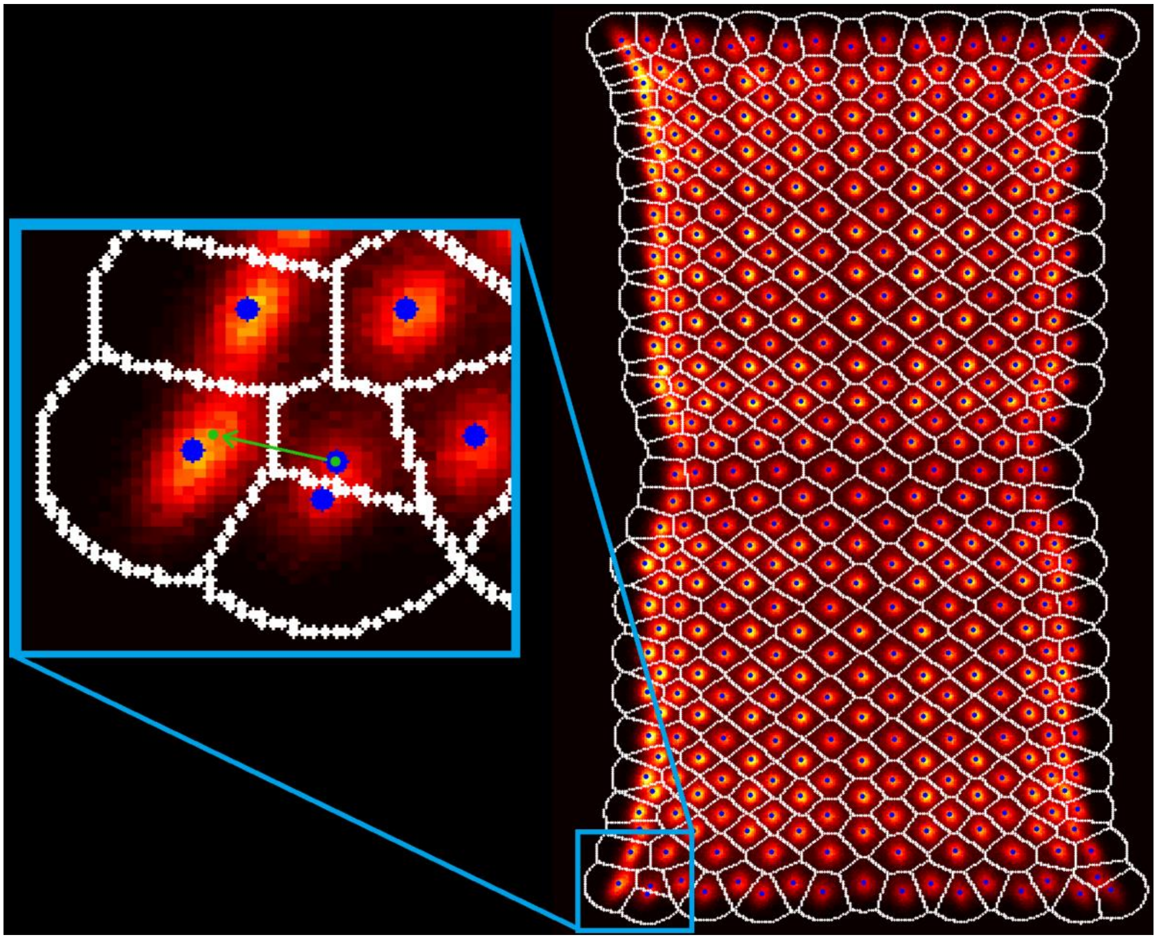

Figure 3-14. Example of crystal center positioning error near corner of flood. The magnified region highlight in green the erroneous, and proper crystal location.

Figure *3-13* shows three examples of the final algorithm output from a trial (100k counts and a 0.5 threshold) with no errors. Examining the data from Table *1* it can be seen there is at least a 99.8% accuracy from all the trials with all errors attributed to crystal centers at or close to the corners of the flood. An example of one such error is shown in Figure *3-14*, where the corner crystal response should contain two crystal centers but one has been shifted to the crystal response on the right. Errors such as this are attributed to poorly resolved corner crystals as shown in Figure *3-14* where instead of two crystal responses, the corner region is one, elongated, response. The error shown in Figure *3-14* represents one crystal that needs correcting in Table *1*.

3.1.1.3 Summary and Discussion of NIM Results

The results of the algorithm applied to the NIM acquired floods are tabulated in Table *1*. Accuracy and minimal user input were goals when creating this algorithm and in the NIM acquired flood histogram tests the algorithm maintained above 99.8% accuracy with a variety of input parameter combinations. As stated before the algorithm reaches best results when the ROI originates from an area of stability (an area where the crystal responses closely resembles the initial template). With the PET insert flood histograms this region of stability was deemed to be the center of the flood. Thus the region of stability was chosen to originate in the center of the flood. This required that the user supply at least one known crystal center near or at the center of the flood histogram to initialize the ROI in the correct place. For these tests the average position of the 205th crystal center was used as the initial ROI location making the user input limited to this point as well as the starting parameters including, step size, template, and log-likelihood threshold.

The results from Table *1* show a tradeoff between run time and accuracy of the algorithm. The main parameter that affects the runtime length is the number of counts used, which increases the number of Gaussian calculations needed to fit each crystal response. However, while some of the times listed in

Table *1* may be unreasonably long for a calibration algorithm, calculating the Gaussian value for each data point is a completely separable process and an excellent candidate for GPU acceleration. Using a GPU could boost the speed of the algorithm between 100 – 1000 times making even the longest of the tests take less than a second per flood.

3.1.2 OpenPET Acquisition Floods

3.1.2.1 Setup

OpenPET is a general purpose electronics readout system for prototype radiotracer imaging scanners. The aim of openPET is to be customizable and flexible to meet the needs of almost any camera or detector design while also meeting critical system requirements such as energy consumption, channel count, and channel density (W. W. Moses et al., 2009). While NIM electronics were used in tested individual detector modules, portability is essential for the PET insert developed by this group so the switch to more compact acquisition electronics was needed. Thus for the completed prototype, openPET readout electronics are used to collect data. The change from NIM to openPET electronics comes with a substantial change in the flood histograms for each of the detector modules. This difference is shown in Figure *3-15* which depicts two flood histograms from the same detector module, one acquired with openPET while the other with NIM. The most notable difference between the two floods is the drop in quality from NIM to openPET. The openPET acquired flood has non-uniformities in counts with the center being less intense compared to the outer regions. Also notable is the drop in corner crystal resolvability from NIM to openPET. The full set of 16 detector module flood histograms acquired with openPET electronics can be viewed in Figure *3-16* which matches the respective detector module floods acquired with NIM electronics shown in Figure *3-8*.

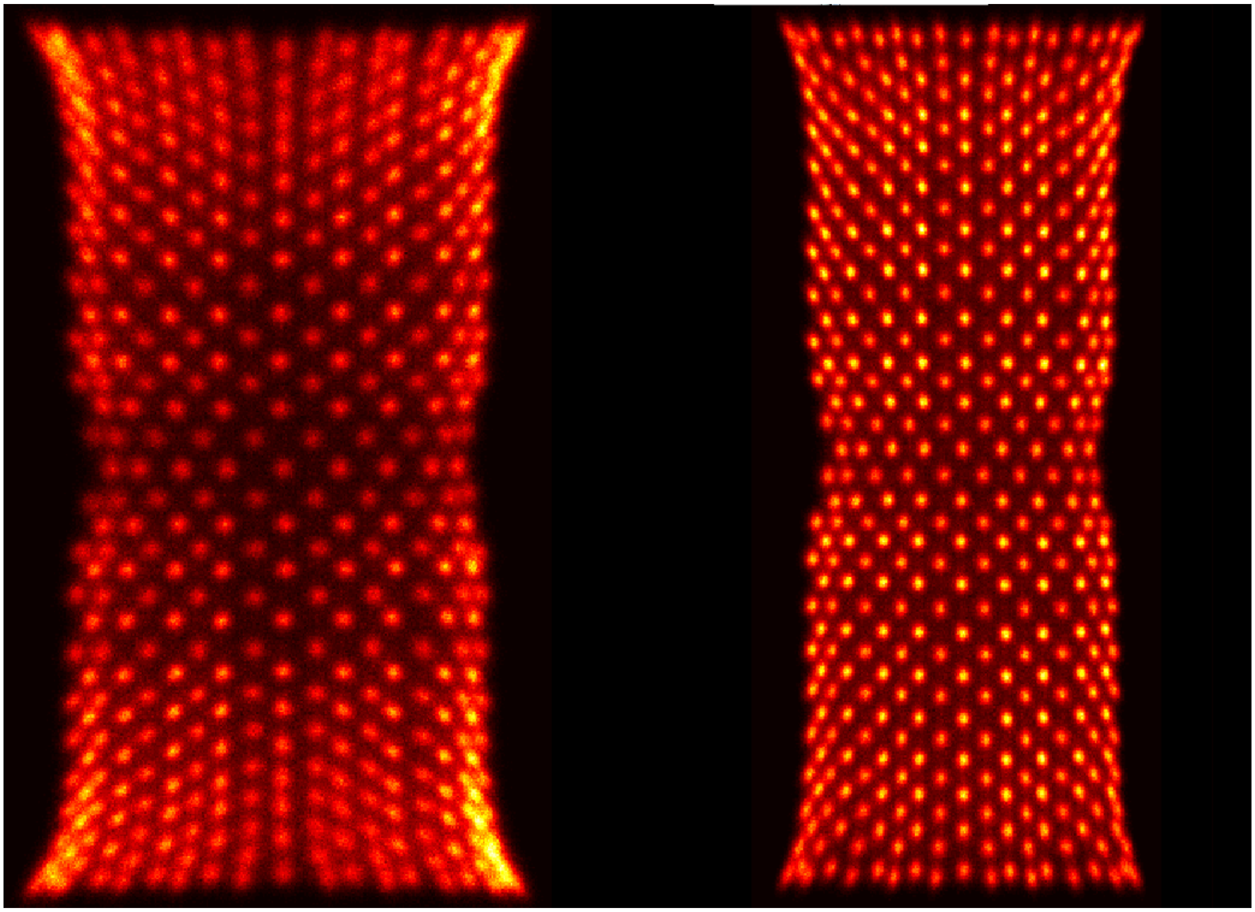

Figure 3-15. Comparison of openPET (left) and NIM (right) acquired flood histograms from the same detector module.

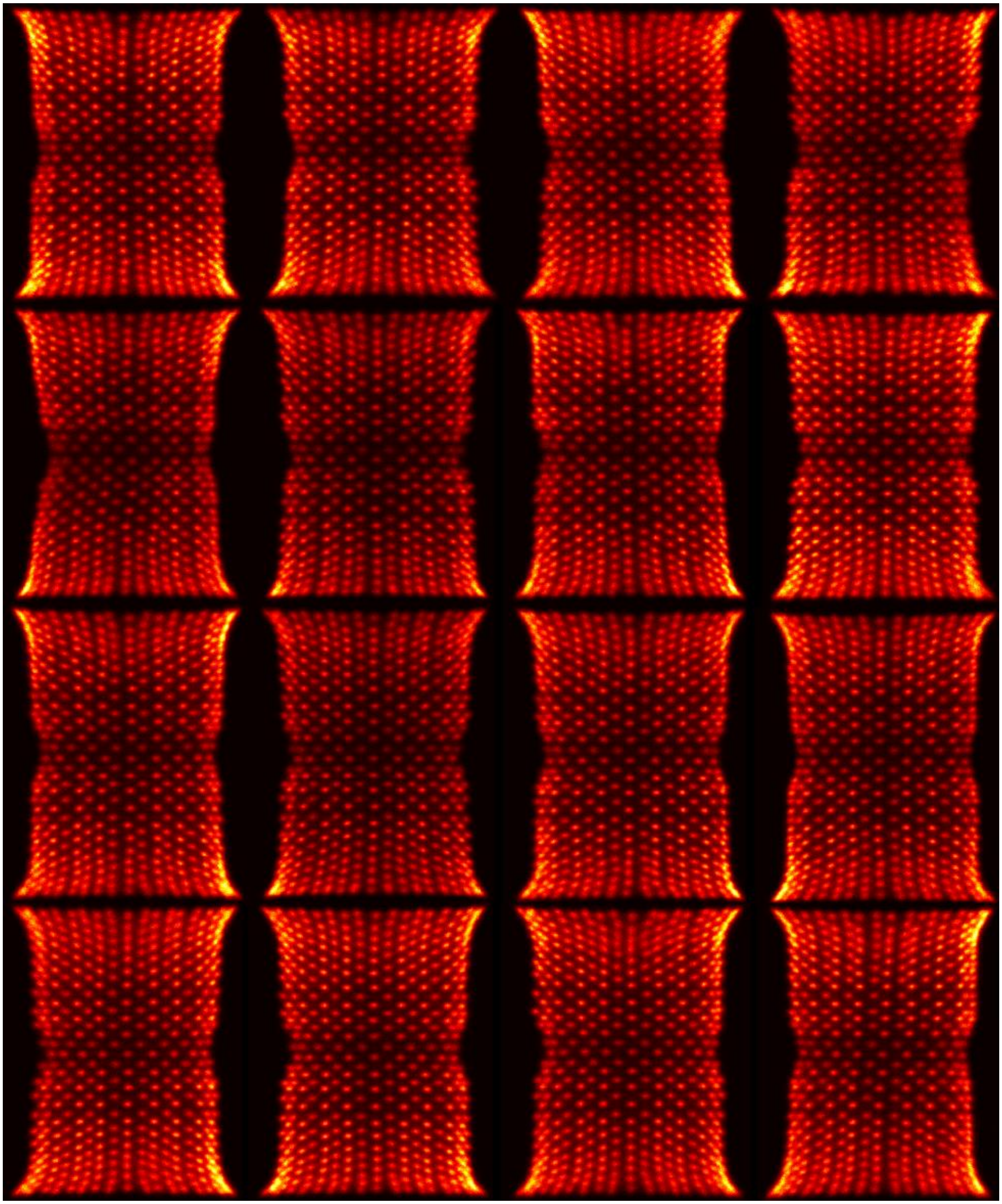

Figure 3-16. All 16 openPET acquired PET insert detector flood histograms

3.1.2.2 Algorithm Results

The algorithm tests on the openPET acquired floods were carried out with the same set of parameters as the NIM tests from section 3.1.1, the only difference being the starting location of the ROI which was re-evaluated to accommodate the change in position of the openPET center crystals. The results of the tests are tabulated in Table *2*.

Table 2. Results from algorithm tests on openPET acquired floods

Step	Threshold	Samples (×10³)	Need Correcting		Accuracy (%)	Avg. Time (s)	Total Time (s)
			Corner	Center			
5	0.05	100	5	0	99.92	73 ± 5.9	1168.3
5	0.5		4	0	99.94	57.1 ± 5.2	913.38
5	5		5	0	99.92	69.8 ± 2.1	1115.9
5	0.05	50	7	0	99.89	31.8 ± 2.4	508.7
5	0.5		8	0	99.88	24.9 ± 1.5	398.8
5	5		6	0	99.91	35.7 ± 1.1	571.4
5	0.05	25	10	2	99.82	16.4 ± 0.8	261.7
5	0.5		9	0	99.86	13.2 ± 0.7	210.9
5	5		7	0	99.89	18.9 ± 0.7	301.9

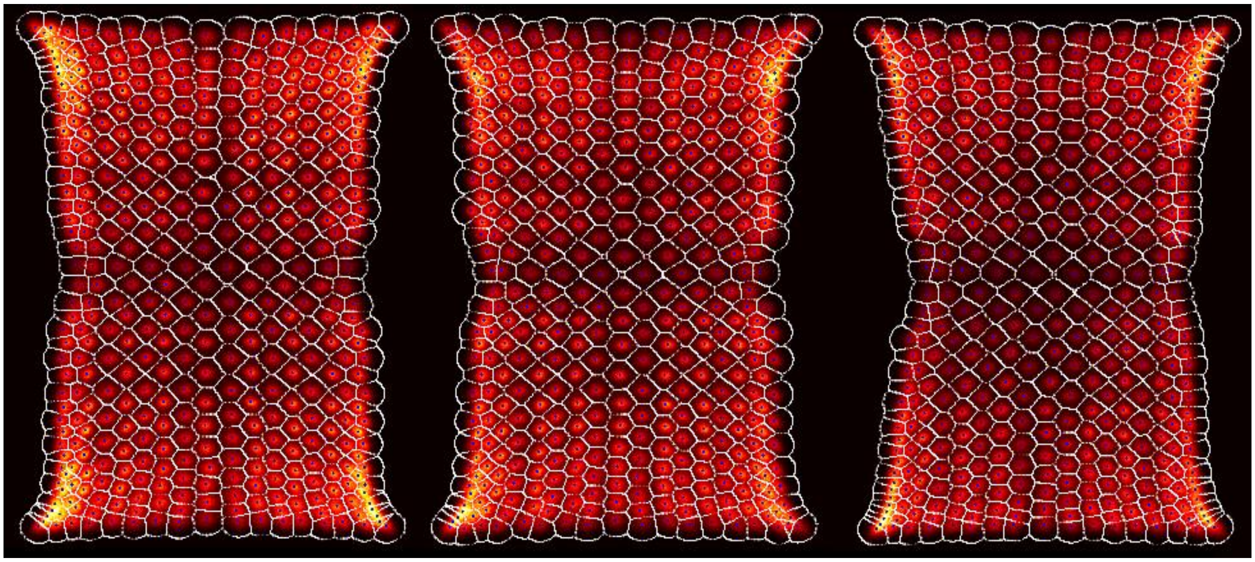

Figure 3-17. Three examples of final algorithm outputs using openPET acquired floods.

3.1.2.3 Summary and Discussion of openPET Results

The results from the openPET algorithm tests can be found in Table *2*. Despite the drop in flood histogram quality compared to the NIM floods, the algorithm still maintained an accuracy above 99.8% and even performed better in some trials than the NIM counterparts. This may seem surprising however the lower resolution corners of the openPET floods limit the ability of the user to correctly identify the location of the true crystal response centers. Thus the results are somewhat misleading in the sense that it may seem that the algorithm performs better with a decrease in flood quality but in fact the ‘true’ crystal center is unresolvable in these blurred corner regions making it difficult to say whether the algorithm has given correct results.

3.1.2.4 In Practice (Calibration)

In practice this crystal identification algorithm will mainly be used as one (embedded) part of our larger PET detector calibration software. The software program, titled ‘PET Detector Analysis,’ is written in MATLAB® and takes the raw data from the four output channels and creates the detector floods, CLUT, and energy lookup table (ELUT). Figure *3-18* shows the flood creation panel from ‘PET Detector Analysis.’ Here the user can create the flood histograms from the raw detector data with various parameters such as max / min energy cut, and different scaling factors. The user can also use an ROI to view energy histograms for the events falling within the ROI bounds.

Figure *3-19* shows the CLUT creation panel. The crystal identification algorithm is embedded within this panel as a callback to the ‘Register’ button in the bottom right corner. This panel helps the user create the CLUTs for each detector. Visible on the right hand side are tools for creating or loading templates (initial point sets). The user would then apply the crystal identification algorithm to this template matching it to the flood histogram. Located along the bottom of the panel is a correction tool for fixing points after running the algorithm in case points were misplaced. This tool is embedded as the call back for the ‘Fix Numbering’ button. Clicking this button puts the right hand display into editing mode where right-clicks from the user select the closest point and left-clicks move the selected points to the new user defined location. Using this panel it is also possible for the user to ‘lock’ certain points before running the algorithm. The ‘Fix Template Points’ button also enables an editing mode in the right display, however, this moves points and also locks them for the algorithm. Locked points are allowed to converge but not allowed to move on iterations of the algorithm. This can have a dramatic effect on the outcome of the algorithm since all the points are connected via the TPS map. The tools and functions located here allow the user to easily utilize the algorithm and fix possible mistakes that may arise.

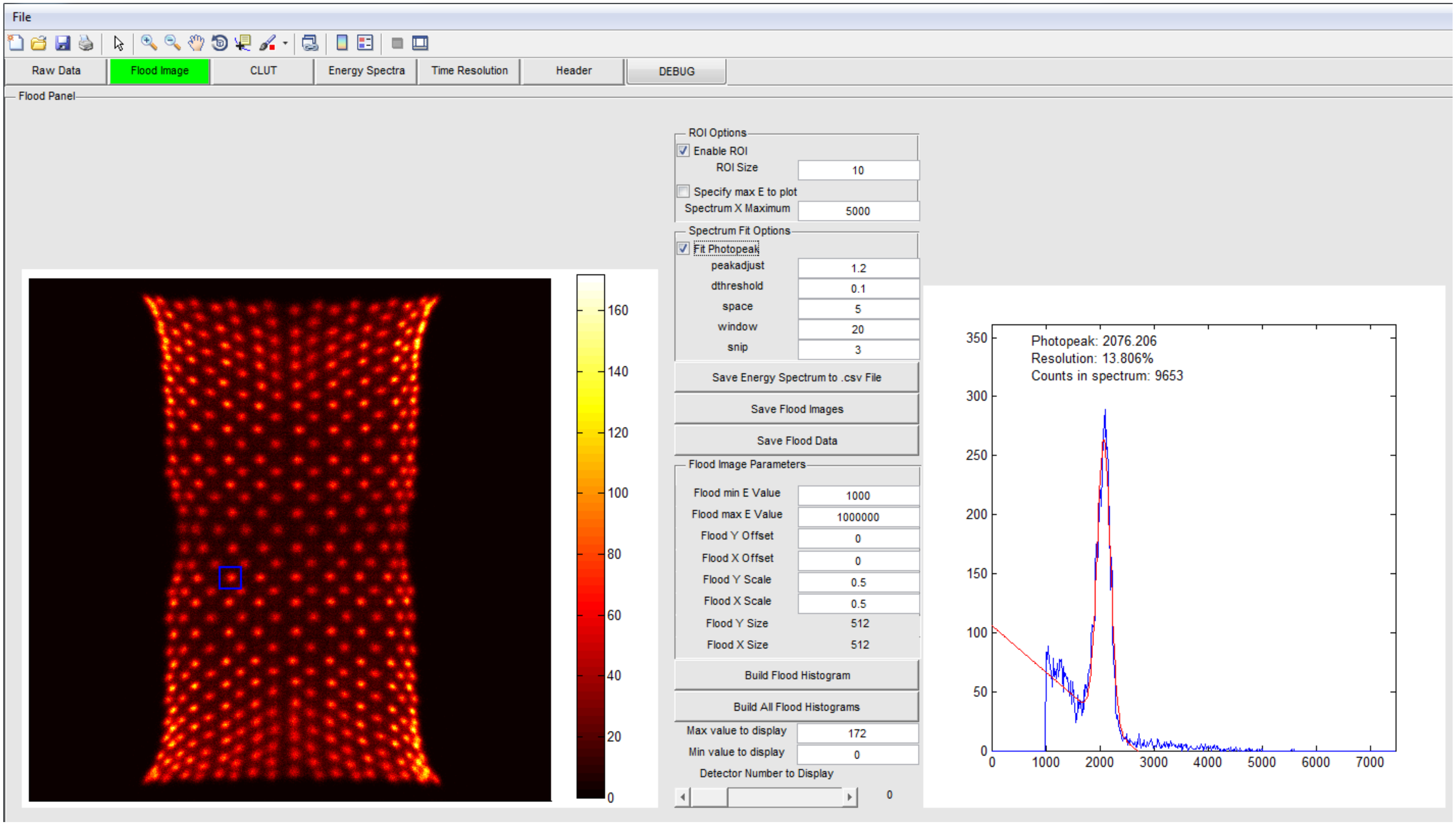

☑ Enable ROI
ROI Size 10
☐ Specify max E to plot
Spectrum X Maximum 5000
☑ Fit Photopeak
peakadjust 1.2
dthreshold 0.1
space 5
window 20
snip 3
Flood min E Value 1000
Flood max E Value 1000000
Flood Y Offset 0
Flood X Offset 0
Flood Y Scale 0.5
Flood X Scale 0.5
Flood Y Size 512
Flood X Size 512
Max value to display 172
Min value to display 0
Detector Number to Display 0

Photopeak: 2076.206
Resolution: 13.806%
Counts in spectrum: 9653

Figure 3-18. Calibration software: flood histogram panel. This panel allows users to create flood histograms for every detector as well as view the energy profiles within an ROI (shown in blue) selected by the user.

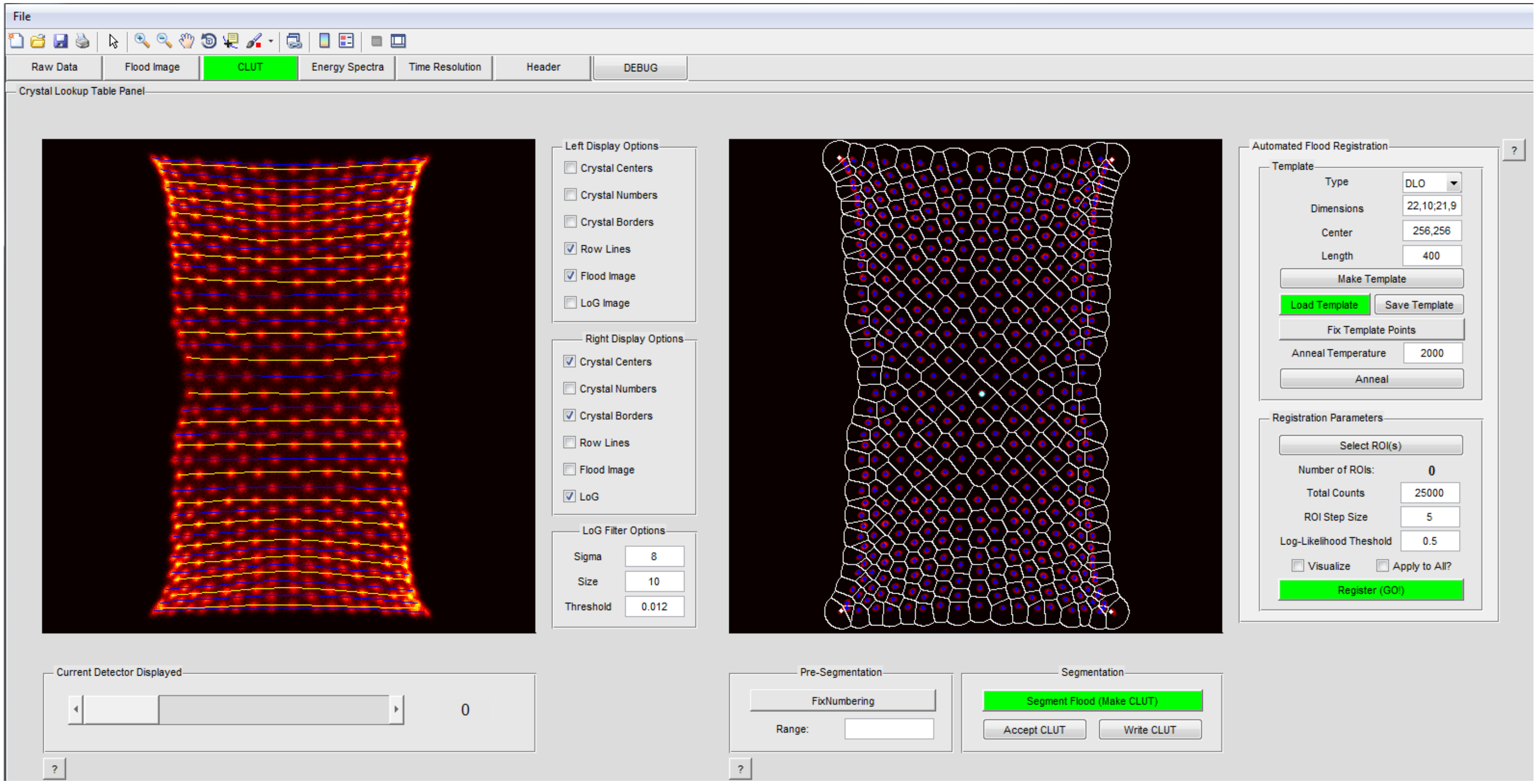

Left Display Options

☐ Crystal Centers
☐ Crystal Numbers
☐ Crystal Borders
☑ Row Lines
☑ Flood Image
☐ LoG Image

Right Display Options

☑ Crystal Centers
☐ Crystal Numbers
☑ Crystal Borders
☐ Row Lines
☐ Flood Image
☑ LoG

LoG Filter Options

Sigma 8
Size 10
Threshold 0.012

Automated Flood Registration

Template

Type DLO
Dimensions 22,10;21,9
Center 256,256
Length 400
Anneal Temperature 2000

Registration Parameters

Number of ROIs: 0
Total Counts 25000
ROI Step Size 5
Log-Likelihood Theshold 0.5
☐ Visualize ☐ Apply to All?

Current Detector Displayed 0

Pre-Segmentation

Range:

Segmentation

Figure 3-19. Calibration software: CLUT panel. In this panel the user creates the CLUT for each detector flood. The crystal identification algorithm is tied to the ‘Register’ button in the bottom right corner. Various tools for making / loading templates are located on the right, as well as tools for correcting possible incorrect points after running the algorithm.

3.2 Siemens Inveon Floods

On top of testing the algorithm with floods from this group's small animal PET detector, flood histograms from a Siemens Inveon Preclinical PET scanner were also made available for testing. The Siemens Inveon consists of 4 rings of 16 detector blocks each making 64 detector blocks total. Each detector block is composed of a 20x20 array of LSO crystals with each crystal having volume dimensions 1.51 x 1.51 x 10 mm^3 with a 1.59 mm crystal pitch. The scanner has a ring diameter, transaxial, and axial FOV of 16.1 mm, 10.0 mm, and 12.7 mm respectively. Light guides are used to couple the crystal arrays to position sensitive (PS) PMTs (Constantinescu & Mukherjee, 2009; Disselhorst et al., 2010; Lijun Lu et al., 2013).

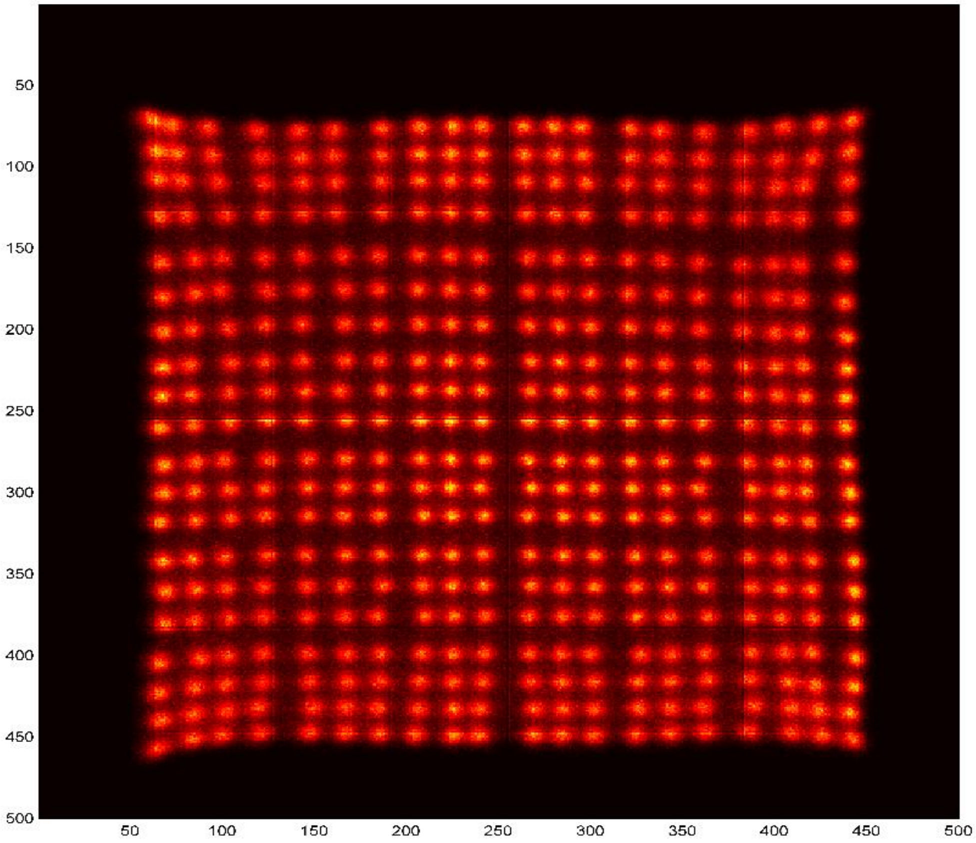

Figure 3-20. A flood histogram from one detector module of a Siemens Inveon PET scanner composed of 400 (20x20) crystals.

Figure *3-20* shows an example of a typical Inveon flood histogram. Immediately noticeable is the relative lack of deformations in the Inveon flood compared to the PET insert developed by our group. The Inveon flood histogram experiences almost no edge crystal compression distortion. This is partially due to the PS-PMT and the way the detector module is constructed. An Inveon detector module uses a photodetector with a smaller active area than the back of the crystal array. A light guide is used to pipe the optical light from scintillation events from the crystals to the PS-PMT. The flood corresponds extremely well to the physical dimensions of the symmetric scintillator array. The only noticeable deformations are slight deviations in the rows and columns of the flood due to irregularities in the crystal array as well as a slight pull outwards of the corner crystal responses where the crystal array is close to the rounded edge of the PS-PMT.

Table 3. Results from 60 Inveon detector blocks, each consisting of 400 crystals.

Step	Threshold	Samples (×10³)	Need Correcting		Accuracy (%)	Avg. Time (s)	Total Time (s)
			Crystals	Floods			
5	0.05	150	2	1	99.992	99 ± 2.5	5941.6
5	0.5		2	1	99.992	87.6 ± 2.4	5253.4
5	5		1	1	99.996	82.4 ± 2.5	4945.1
5	0.05	100	0	0	100	65.2 ± 2.2	3910.9
5	0.5		1	1	99.996	58.2 ± 1.6	3493.6
5	5		1	1	99.996	55.5 ± 1.7	3330.2
5	0.05	50	5	1	99.979	31.2 ± 0.9	1811.9
5	0.5		1	1	99.996	28.2 ± 0.8	1633.5
5	5		1	1	99.996	27.4 ± 0.5	1641.3
5	0.05	25	2	2	99.992	16.5 ± 0.3	955.3
5	0.5		0	0	100	15 ± 0.4	870
5	5		1	1	99.996	14.7 ± 0.3	852

Table *3* summarizes the results from the application of our algorithm to the 60 Inveon floods that were made available to us. In this table the 'Threshold' represents the log-likelihood threshold used to determine convergence and the 'Step' column is the change in ROI step size between each iteration.

The ‘Need Correcting’ column is divided into two sub-columns with ‘Crystals’ showing the total number of crystals needing correcting across all 60 floods and ‘Floods’ being the number of floods the respective crystals covered, i.e. one flood might need multiple corrections. The ‘Accuracy’ column is the percentage of correct crystals across all 60 x 400 = 24000 crystals. The ‘Time’ column and subsequent sub-columns remain the same as in previous tables, with the average time representing the mean algorithm runtimes for individual floods. As shown in the table, the algorithm maintained an accuracy upwards of 99.9% across all 60 floods. On average each set of algorithm runs required only 1 or 2 corrections across the 60 floods which were spread at most across 2 floods. As expected, runtime was directly proportional to the number of samples used and inversely proportional to log-likelihood threshold.

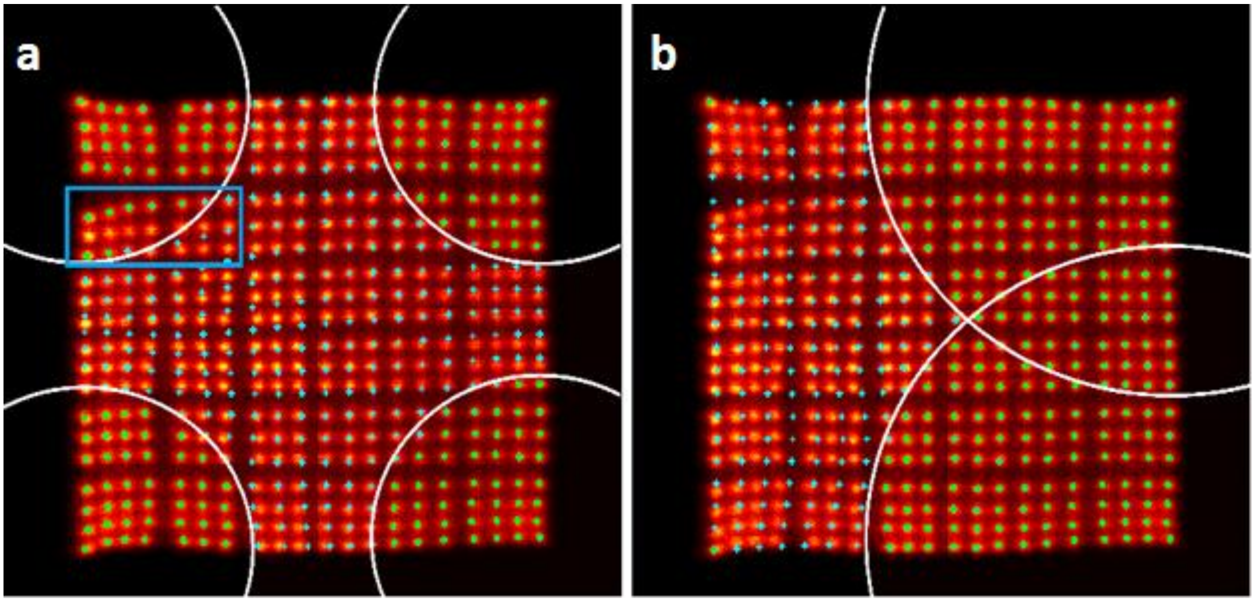

Figure 3-21. Left: Corner expansion ROI for error prone flood, error region shown in blue rectangle. Right: ROIs removed or altered to better suit error prone flood. Converged points are shown in green, with un-converged points in blue and the ROIs in white.

For the Inveon detectors, the ROIs for the algorithm were initialized and expanded from the corners of the flood, see ***Figure 3-21*-a**. Due to the uniformity of the Inveon flood histograms, the corners were the most stable regions to accurately match the template to the proper crystal response. The few errors across all the batches were mainly localized to the same two floods within the 60. These floods (one of which is depicted in ***Figure 3-21***) showcase attributes to which the algorithm is error prone. It was hypothesized that these errors were caused by local deformations in the flood image that could not be accurately predicted by the ROI that activated the erroneous points. For these floods, it was found that disabling the ROIs closest to the error regions resulted in a better fit, allowing the TPS map to better predict the locations of the crystal responses. An example of this is shown in ***Figure 3-21*****-b** where the two left side ROIs have been disabled, allowing the right side ROIs to complete the entire flood. The error in crystal identification is depicted in ***Figure 3-21*****-a** left within the blue rectangle showing several crystals the algorithm has missed. By allowing the user to select ROI starting locations as an extra step, the error can be reduced. In all tested cases, choosing the ROIs for problematic floods allowed all crystals to be correctly identified. The disadvantage is this step requires extra time and user input to define and predict which ROIs should be active.

3.3 Pin Cushion Distortion Floods

Lastly, one pincushion distorted flood was tested (Wu et al., 2009), shown in Figure *3-22*. Since there is only one of these floods no statistical data is available and this section merely serves as a proof of concept for floods with similar distortions. The algorithm was initalized with a square 8x8 template, shown in Figure *3-23*, which was centered at the center of mass for the flood. The ROI was also initilized and expanded starting at the center of mass for the flood. The algorithm identifies the crystal center with relative ease starting from the center of the flood and working outwards.

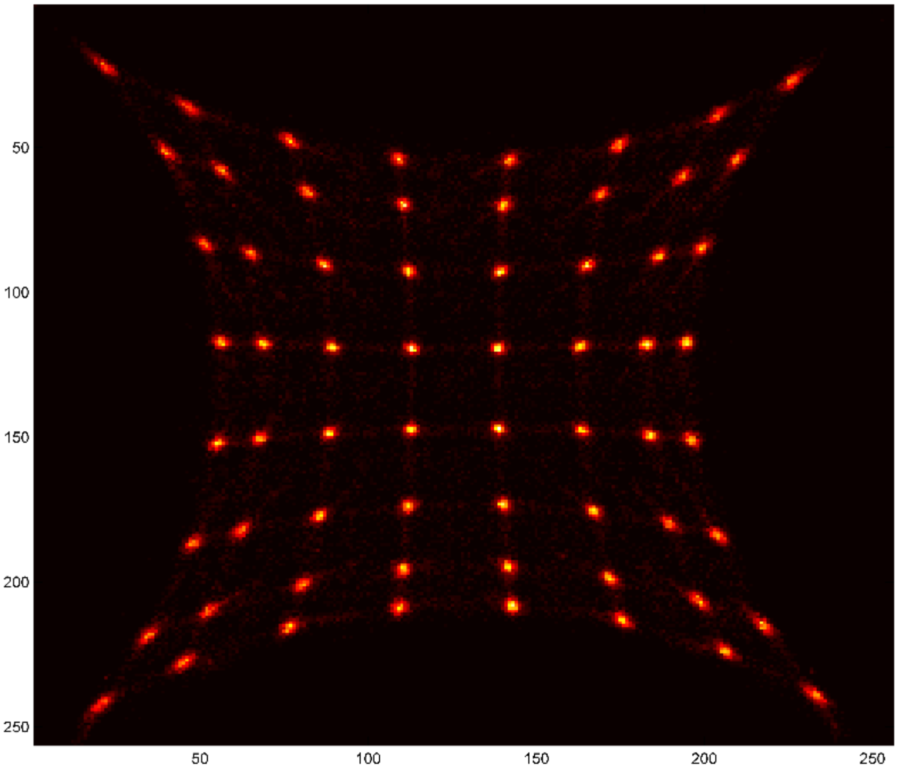

Figure 3-22. Pin cushion distortion flood from an 8x8 64 crystal PET detector module.

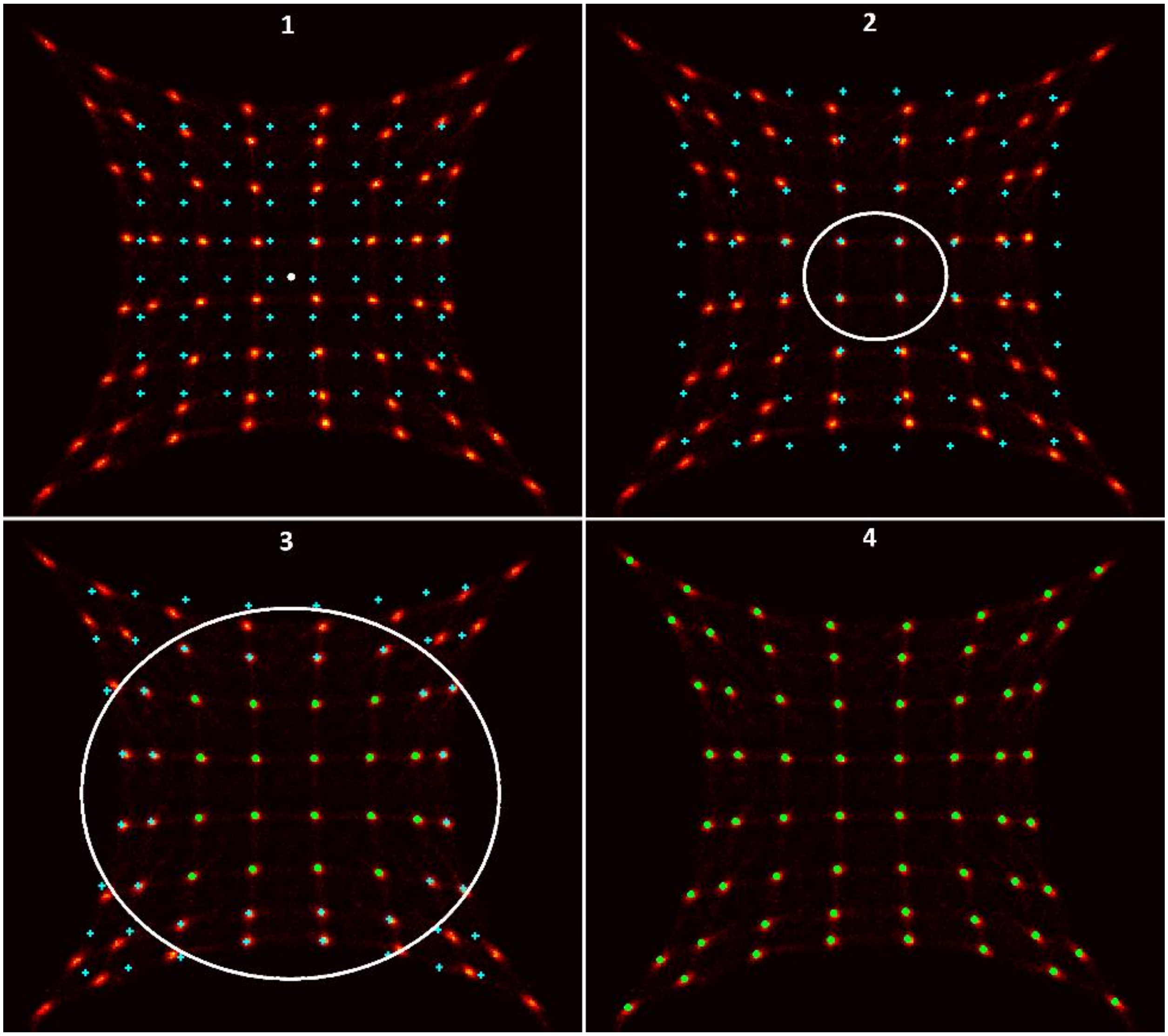

Figure 3-23. Depiction of the algorithm fitting the pin cushion distorted flood at several stages. 1) Initial template shown as blue dots. 2-3) ROI expanding, converged points shown in green. 4) Final algorithm output with all points converged.

4 Summary and Future Work

4.1 Summary

The crystal identification algorithm developed for this thesis project and calibration software of the small animal PET insert developed by this group shows accuracy and versatility when identifying crystal response regions of various flood histograms. The algorithm was creating with the following goals in mind:

- **Speed** – Must require significantly less than the time required for manual segmentation.
- **Robustness** – There are a variety of distortions, of varying magnitude, unique to the flood histograms used for testing. The algorithm should successfully identify crystals in these difficult regions.
- **Accuracy** – Should identify the location of crystals to equal or greater accuracy than manual segmentation.
- **Minimal user input** - Should use the minimal amount of initial data and user correction throughout algorithm.

The algorithm consistently maintained an accuracy above 99.8% with various input parameter combinations for all 4 sets of flood histograms used for testing. The user input throughout the testing was limited to the input parameters of the algorithm: counts, ROI step size, and log-likelihood threshold, as well as one user defined starting point for the ROI. For very symmetric flood histograms it was found that this last user defined point may not even be necessary. For flood histograms with more complicated deformations it was found that increasing the user input, by defining more crystal centers before the algorithm starts, leads to a direct increase in algorithm accuracy. Thus the algorithm shows versatility when dealing with various levels of flood quality; if the user is presented with a low quality flood they might input 5, or more, extra points and vice versa if presented with a very uniform flood they might choose only to input one or even nothing.

The run time of the algorithm varied between ~20 and ~80 seconds per flood. While this is substantially faster than manual segmentation (a 400 crystal flood takes at least 400 seconds) it was still hoped that the whole crystal identification process, for the small animal PET insert set of 16 floods, would take less than ten minutes. While current times are longer than this goal, this algorithm has highly parallel calculation and is an excellent candidate for GPU acceleration. Running the operations found within the algorithm with a GPU is expected to speed up the run time hundreds of times faster. Excluding the user input time, this would enable full calibration of a 16 detector set well under 10 minutes.

4.2 Future Work

It is expected that work will continue on this algorithm as is it used in the calibration software for the small animal PET insert developed by this group whether it is in a laboratory setting or as a commercial package for the scanner. There is no planned extension of the algorithm as of this moment however there are several additions to this work that were discussed but never realized due to time constraints and feasibility. These additions are listed below and could serve as possible future endeavors for this work.

- 3D flood segmentation – In the calibration process for a PET scanner the CLUT is created (with this algorithm) then in each crystal region a photopeak is fit to the energy data. The photopeak is assumed to be a Gaussian plus linear function. Rather than these two processes being separate the list mode data could be looked at as a 3 dimensional data set, having an (x, y) position but also an energy position as well, giving it a location in 3D space with the axes being x, y, and energy. The algorithm would then find both crystal center and photopeak position in one step by fitting a 3D GMM to the list mode data saving time and possibly improving accuracy.

- Probabilistic LOR creation – Somewhat more theoretical is the idea of creating LORs for image reconstruction in a probabilistic manner. Instead of the CLUT being hard coded crystal numbers it would be left in the Gaussian form created by this algorithm. Events coming in would then be given a set of probabilities as to which Gaussians they most correspond to, instead of a single crystal ID number. The LORs created would then have weights corresponding to how likely the two events are to have come from the respective crystal centers. While this could represent a more accurate image it would also mean a substantial increase in computing resources and possibly reconstruction time.
- Error prediction – As the algorithm fits Gaussians to the sampled flood histogram, errors can occur leading to a propagation of incorrectly numbered crystal responses. In theory it should be possible to predict when these occur by actively monitoring the log-likelihood of each Gaussian as it is fit as well as the correspondence of each point within the ROI. If an error is detected mid-algorithm, one might wish the algorithm to halt and display the problematic region. In the case of more than one ROI expanding across the flood, it has been found that the ROI responsible for the error can be stopped while letting the other ROI(s) expand, possibly allowing a more accurate fit.

5 References

Anger, H. O. (1966). Sensitivity, Resolution, and Linearity of the Scintillation Camera. *IEEE Transactions on Nuclear Science, 13*(3), 380–392. doi:10.1109/TNS.1966.4324123

Bao, Q., Newport, D., Chen, M., Stout, D. B., & Chatziioannou, A. F. (2009). Performance evaluation of the inveon dedicated PET preclinical tomograph based on the NEMA NU-4 standards. *Journal of Nuclear Medicine : Official Publication, Society of Nuclear Medicine*, *50*(3), 401–408. doi:10.2967/jnumed.108.056374

Bilmes, J. (1997). A Gentle Tutorial of the EM Algorithm and its Application to Parameter Estimation for Gaussian Mixture and Hidden Markov Models. Retrieved from http://citeseerx.ist.psu.edu/viewdoc/summary?doi=10.1.1.28.613

Bookstein, F. L. (1989). Principal warps: thin-plate splines and the decomposition of deformations. *IEEE Transactions on Pattern Analysis and Machine Intelligence*, *11*(6), 567–585. doi:10.1109/34.24792

Canadas, M., Sanz, E. R., Vives, M. O., Vaquero, J. J., Desco, M., Vicente, E., … Romero, L. (2010). Performance evaluation for 68Ga and 18F of the ARGUS small-animal PET scanner based on the NEMA NU-4 standard. In *IEEE Nuclear Science Symposuim & Medical Imaging Conference* (pp. 3454–3457). IEEE. doi:10.1109/NSSMIC.2010.5874448

Casey, M. E., & Nutt, R. (1986). A Multicrystal Two Dimensional BGO Detector System for Positron Emission Tomography. *IEEE Transactions on Nuclear Science*, *33*(1), 460–463. doi:10.1109/TNS.1986.4337143

Chaudhari, A. J., Joshi, A. a, Bowen, S. L., Leahy, R. M., Cherry, S. R., & Badawi, R. D. (2008). Crystal identification in positron emission tomography using nonrigid registration to a Fourier-based template. *Physics in Medicine and Biology*, *53*(18), 5011–27. doi:10.1088/0031-9155/53/18/011

Cherry, S., Sorenson, J., & Phelps, M. (2012). *Physics in nuclear medicine* (4th ed.).

Cho, Z. H., Chan, J. K., Ericksson, L., Singh, M., Graham, S., MacDonald, N. S., & Yano, Y. (1975). Positron ranges obtained from biomedically important positron-emitting radionuclides. *Journal of Nuclear Medicine : Official Publication, Society of Nuclear Medicine, 16*(12), 1174–6. Retrieved from http://europepmc.org/abstract/med/1194970

Chui, H., & Rangarajan, A. (2003). A new point matching algorithm for non-rigid registration. *Computer Vision and Image Understanding*, *89*(October 2002), 114–141. doi:10.1016/S1077-3142(03)00009-2

Colombino, P., Fiscella, B., & Trossi, L. (1965). Study of positronium in water and ice from 22 to -144 °C by annihilation quanta measurements. *Il Nuovo Cimento*, *38*(2), 707–723. doi:10.1007/BF02748591

Constantinescu, C. C., & Mukherjee, J. (2009). Performance evaluation of an Inveon PET preclinical scanner. *Physics in Medicine and Biology*, *54*(9), 2885–2899. doi:10.1088/0031-9155/54/9/020

Dempster, a, Laird, N., & Rubin, D. (1977). Maximum Likelihood from Incomplete Data via the EM Algorithm. *Journal of the Royal Statistical Society. Series B (Methodological)*, *39*(1), 1–38. Retrieved from http://www.jstor.org/stable/2984875

Disselhorst, J. a, Brom, M., Laverman, P., Slump, C. H., Boerman, O. C., Oyen, W. J. G., … Visser, E. P. (2010). Image-quality assessment for several positron emitters using the NEMA NU 4-2008 standards in the Siemens Inveon small-animal PET scanner. *Journal of Nuclear Medicine : Official Publication, Society of Nuclear Medicine*, *51*(4), 610–617. doi:10.2967/jnumed.109.068858

Gauvain, J. L., & Lee, C. H. (1994). Maximum a posteriori estimation for multivariate Gaussian mixture observations of Markov chains. *IEEE Transactions on Speech and Audio Processing*, *2*(2), 291–298. doi:10.1109/89.279278

Hawkes, R. C., Fryer, T. D., Lucas, A. J., Siegel, S. B., Ansorge, R. E., Clark, J. C., & Carpenter, T. A. (2008). Initial performance assessment of a combined microPET focus-F120 and MR split magnet system. *2008 IEEE Nuclear Science Symposium Conference Record*, 3673–3678. doi:10.1109/NSSMIC.2008.4774113

Hoffman, E. J., Phelps, M. E., Mullani, N. a, Higgins, C. S., & Ter-pogossian, M. M. (1976). Design and Performance Characteristics of a Whole-Body Positron Transaxial Tomograph. *Journal of Nuclear Medicine*, *17*(6), 493–502.

Hong, S. J., Kang, H. G., Ko, G. B., Song, I. C., Rhee, J.-T., & Lee, J. S. (2012). SiPM-PET with a short optical fiber bundle for simultaneous PET-MR imaging. *Physics in Medicine and Biology*, *57*(12), 3869–3883. doi:10.1088/0031-9155/57/12/3869

Hu, D., Atkins, B. E., Lenox, M. W., Castleberry, B., & Siegel, S. B. (2006). A neural network based algorithm for building crystal look-up table of PET block detector. *IEEE Nuclear Science Symposium Conference Record*, *4*(1), 2458–2461. doi:10.1109/NSSMIC.2006.354409

Judenhofer, M. S., Wehrl, H. F., Newport, D. F., Catana, C., Siegel, S. B., Becker, M., … Pichler, B. J. (2008). Simultaneous PET-MRI: a new approach for functional and morphological imaging. *Nature Medicine*, *14*(4), 459–65. doi:10.1038/nm1700

Knoll, G. F. (2010). *Radiation Detection and Measurement* (4th ed.). John Wiley & Sons.

Kong, H., Akakin, H. C., & Sarma, S. E. (2013). A generalized laplacian of gaussian filter for blob detection and its applications. *IEEE Transactions on Cybernetics*, *43*(6), 1719–1733. doi:10.1109/TSMCB.2012.2228639

Langner, J. (2003). *Development of a Parallel Computing Optimized Head Movement Correction Method in Positron-Emission-Tomography*. University of Applied Sciences, Dresden.

Lecomte, R., Cadorette, J., Rodrigue, S., Lapointe, D., Rouleau, D., Bentourkia, M., … Msaki, P. (1996). Initial results from the Sherbrooke avalanche photodiode positron tomograph. *IEEE Transactions on Nuclear Science*, *43*(3), 1952–1957. doi:10.1109/23.507252

Levin, C. S., & Hoffman, E. J. (1999). Calculation of positron range and its effect on the fundamental limit of positron emission tomography system spatial resolution. *Physics in Medicine and Biology*, *44*(3), 781–799. doi:10.1088/0031-9155/45/2/501

Lijun Lu, Karakatsanis, N., Jianhua Ma, Zhaoying Bian, Yanjiang Han, Jing Tang, … Chatziioannou, A. F. (2013). Performance evaluation of the Inveon PET scanner using GATE based on the NEMA NU-4 standards. In *2013 IEEE Nuclear Science Symposium and Medical Imaging Conference (2013 NSS/MIC)* (Vol. 50, pp. 401–408). IEEE. doi:10.1109/NSSMIC.2013.6829094

Lucas, A. J., Hawkes, R. C., Guerra, P., Ansorge, R. E., Nutt, R. E., Clark, J. C., … Carpenter, T. A. (2006). Development of a combined microPET-MR system. *IEEE Nuclear Science Symposium Conference Record*, *4*, 2345–2348. doi:10.1109/NSSMIC.2006.354384

Maramraju, S. H., Junnarkar, S., Ravindranath, B., Southekal, S., Stoll, S., Smith, S. D., … Schlyer, D. (2008). An MR compatible PET scanner based on RatCAP for small animal imaging at 9.4 T. *IEEE Nuclear Science Symposium Conference Record*, 3679–3682. doi:10.1109/NSSMIC.2008.4774114

Melcher, C. L. (2000). Scintillation crystals for PET. *Journal of Nuclear Medicine : Official Publication, Society of Nuclear Medicine*, *41*(6), 1051–1055.

Moses, W. W. (2011). Fundamental Limits of Spatial Resolution in PET. *Nuclear Instruments & Methods in Physics Research. Section A, Accelerators, Spectrometers, Detectors and Associated Equipment*, *648 Supple*, S236–S240. doi:10.1016/j.nima.2010.11.092

Moses, W. W., Buckley, S., Vu, C., Peng, Q., Pavlov, N., Choong, W. S., … Jackson, C. (2009). OpenPET: A flexible electronics system for radiotracer imaging. *IEEE Transactions on Nuclear Science*, *57*(5 PART 1), 2532–2537. doi:10.1109/TNS.2010.2058866

Petrillo, G. A., McIntyre, R. J., Lecomte, R., Lamoureux, G., Schmitt, D., & Hx, C. (1984). Scintillation Detection with Large-Area Reach-Through Avalanche Photodiodes. *IEEE Transactions on Nuclear Science*, *31*(1), 417–423. doi:10.1109/TNS.1984.4333290

Phelps, M. E., Hoffman, E. J., Huang, S. C., & Kuhl, D. E. (1978). ECAT: a new computerized tomographic imaging system for positron-emitting radiopharmaceuticals. *Journal of Nuclear Medicine : Official Publication, Society of Nuclear Medicine*, *19*(6), 635–647.

Pichler, B., Lorenz, E., Mirzoyan, R., Pimpl, W., Roder, F., Schwaiger, M., & Ziegler, S. I. (1997). Performance test of a LSO-APD PET module in a 9.4 Tesla magnet. *1997 IEEE Nuclear Science Symposium Conference Record*, *2*, 1237–1239. doi:10.1109/NSSMIC.1997.670533

Saveliev, V., & Golovin, V. (2000). Silicon avalanche photodiodes on the base of metal-resistor-semiconductor (MRS) structures. *Nuclear Instruments and Methods in Physics Research, Section A: Accelerators, Spectrometers, Detectors and Associated Equipment*, *442*(1-3), 223–229. doi:10.1016/S0168-9002(99)01225-5

Schlyer, D. J. (2004). PET tracers and radiochemistry. *Annals of the Academy of Medicine Singapore*, *33*(2), 146–154.

Shams, E. (2014). *A Slow Control System with Gain Stabilization for a Small Animal MR-Compatible PET Insert*. University of Manitoba.

Shibuya, K., Yoshida, E., Nishikido, F., Suzuki, T., Tsuda, T., Inadama, N., … Murayama, H. (2007). Annihilation photon acollinearity in PET: volunteer and phantom FDG studies. *Physics in Medicine and Biology*, *52*(17), 5249–5261. doi:10.1088/0031-9155/52/17/010

Spurrier, M. A., Szupryczynski, P., Yang, K., Carey, A. A., Melcher, C. L., & Member, S. (2008). Effects of Ca2+ co-doping on the scintillation properties of LSO: Ce. *IEEE Transactions on Nuclear Science*, *55*(3), 1178–1182. doi:10.1109/TNS.2007.913486

Stonger, K. a., & Johnson, M. T. (2004). Optimal calibration of PET crystal position maps using Gaussian mixture models. *IEEE Transactions on Nuclear Science*, *51*(1 I), 85–90. doi:10.1109/TNS.2004.823334

Stortz, G., Walker, M. D., Thompson, C. J., Goertzen, A. L., Retiere, F., Zhang, X., … Retière, F. (2013). Characterization of a New MR Compatible Small Animal PET Scanner Using Monte-Carlo Simulations. *IEEE Transactions on Nuclear Science*, *60*(3), 1637–1644. doi:10.1109/TNS.2013.2256927

Suk, J. Y., Thompson, C. J., Labuda, A., & Goertzen, A. L. (2008). Improvement of the spatial resolution of the MicroPET R4 scanner by wobbling the bed. *Medical Physics*, *35*(4), 1223. doi:10.1118/1.2868760

Tsoumpas, C., Agarwal, S., Marsden, P. K., & King, A. P. (2012). Evaluation of two PET motion correction techniques for simultaneous real-time PET-MR acquisitions using an MR-derived motion model. *IEEE Nuclear Science Symposium Conference Record*, 2519–2522. doi:10.1109/NSSMIC.2012.6551574

Vincent, L., & Soille, P. (1991). Watersheds in digital spaces: An efficient algorithm based on immersion simulations. *IEEE Transactions on Pattern Analysis and Machine Intelligence*. doi:10.1109/34.87344

Vinke, R., & Levin, C. S. (2014). A method to achieve spatial linearity and uniform resolution at the edges of monolithic scintillation crystal detectors. *Physics in Medicine and Biology*, *59*(12), 2975–2995. doi:10.1088/0031-9155/59/12/2975

Wang, Y., Seidel, J., Tsui, B. M. W., Vaquero, J. J., & Pomper, M. G. (2006). Performance Evaluation of the GE Healthcare eXplore VISTA Dual-Ring Small-Animal PET Scanner. *J. Nucl. Med.*, *47*(11), 1891–1900. Retrieved from http://jnm.snmjournals.org.proxy2.lib.umanitoba.ca/content/47/11/1891.full

Wilkinson, D. H. (1952). The Phoswich—A Multiple Phosphor. *Review of Scientific Instruments*, *23*(8), 414. doi:10.1063/1.1746324

Wirrwar, A., Vosberg, H., Herzog, H., Hailing, H., & Weber, S. (1997). 4.5 Tesla magnetic field reduces range of high-energy positrons-potential implications for positron emission tomography. *IEEE Transactions on Nuclear Science*, *44*(2), 184–189. doi:10.1109/23.568801

Wu, Y., Ng, T. S. C., Yang, Y., Shah, K., Farrell, R., & Cherry, S. R. (2009). A study of the timing properties of position-sensitive avalanche photodiodes. *Physics in Medicine and Biology*, *54*(17), 5155–72. doi:10.1088/0031-9155/54/17/006

Xiaowen, K., Zheng, G., Xishan, S., Yaqiang, L., Shi, W., Zhaoxia, W., … Yongjie, J. (2008). Comparing crystal identification algorithms for PET block detectors. *IEEE Nuclear Science Symposium Conference Record*, 4562–4566. doi:10.1109/NSSMIC.2008.4774301

Yoshida, E., Kimura, Y., Kitamura, K., & Murayama, H. (2004). Calibration procedure for a DOI detector of high resolution PET through mixture Gaussian model. *2003 IEEE Nuclear Science Symposium. Conference Record (IEEE Cat. No.03CH37515)*, *4*(5), 2543–2549. doi:10.1109/NSSMIC.2003.1352398

Zaidi, H., Ojha, N., Morich, M., Griesmer, J., Hu, Z., Maniawski, P., … Shao, L. (2011). Design and performance evaluation of a whole-body Ingenuity TF PET-MRI system. *Physics in Medicine and Biology*, *56*, 3091–3106. doi:10.1088/0031-9155/56/10/013